5-7-2005

In-Situ Surface Science Studies of the Interaction between Sulfur Dioxide and Two-Dimensional Palladium Loaded-Cerium/Zirconium mixed Metal Oxide Model Catalysts

Esteban Javier Romano

Recommended Citation

Romano, Esteban Javier, "In-Situ Surface Science Studies of the Interaction between Sulfur Dioxide and Two-Dimensional Palladium Loaded-Cerium/Zirconium mixed Metal Oxide Model Catalysts" (2005). *Theses and Dissertations*. 2750.
https://scholarsjunction.msstate.edu/td/2750

IN-SITU SURFACE SCIENCE STUDIES OF THE INTERACTION BETWEEN SULFUR DIOXIDE AND TWO-DIMENSIONAL PALLADIUM LOADED-CERIUM/ZIRCONIUM MIXED METAL OXIDE MODEL CATALYSTS

By

Esteban Javier Romano

A Dissertation
Submitted to the Faculty of
Mississippi State University
in Partial Fulfillment of the Requirements
for the Degree of Doctor of Philosophy
in Chemical Engineering
in the Dave C. Swalm School of Chemical Engineering

Mississippi State, Mississippi

May 2005

IN-SITU SURFACE SCIENCE STUDIES OF THE INTERACTION BETWEEN SULFUR DIOXIDE AND TWO-DIMENSIONAL PALLADIUM LOADED-CERIUM/ZIRCONIUM MIXED-METAL OXIDE MODEL CATALYSTS

By

Esteban Javier Romano

Approved:

Kirk H. Schulz
Dean of Engineering, Earnest W. and Mary Ann Deavenport, Jr., Chair, James W. Bagley College of Engineering
(Major Professor)

Clifford E. George
Professor and Interim Director of the Dave C. Swalm School of Chemical Engineering
(Committee Member)

Hossein Toghiani
Associate Professor of Chemical Engineering (Committee Member)

Priscilla J. Hill
Assistant Professor of Chemical Engineering (Committee Member)

Mark E. Zappi
Texas Olefins Professor and Graduate Coordinator of Chemical Engineering

Name: Esteban Javier Romano

Date of Degree: May 7, 2005

Institution: Mississippi State University

Major Field: Chemical Engineering

Major Professor: Dr. Kirk H. Schulz

Title of Study: IN-SITU SURFACE SCIENCE STUDIES OF THE INTERACTION BETWEEN SULFUR DIOXIDE AND TWO-DIMENSIONAL PALLADIUM LOADED-CERIUM/ZIRCONIUM MIXED-METAL OXIDE MODEL CATALYSTS

Pages in Study: 153

Candidate for Degree of Doctor of Philosophy

Cerium and zirconium oxides are important materials in industrial catalysis. Particularly, the great advances attained in the past 30 years in controlling levels of gaseous pollutants released from internal combustion engines can be attributed to the development of catalysts employing these materials. Unfortunately, oxides of sulfur are known threats to the longevity of many catalytic systems by irreversibly interacting with catalytic materials.

In this work, polycrystalline cerium-zirconium mixed-metal-oxide (MMO) solid solutions were synthesized. High resolution x-ray photoelectron spectroscopy (XPS) spectral data was collected and

examined for revelation of the surface species that form on these metal oxides after in-situ exposures to sulfur dioxide. The model catalysts were exposed to sulfur dioxide using a custom modified in-situ reaction cell and platen heater. The results of this study demonstrate the formation of sulfate and sulfite surface sulfur species. Temperature and compositional dependencies were displayed, with higher temperatures and ceria molar ratios displaying a larger propensity for forming surface sulfur species.

In addition to analysis of sulfur photoemission, the photoemission regions of oxygen, zirconium, and cerium were examined for the materials used in this study before and after the aforementioned treatments with sulfur dioxide. The presence of surface hydroxyl groups was observed and metal oxidation state changes were probed to further enhance the understanding of sulfur dioxide adsorption on the synthesized materials.

Palladium loaded mixed-metal oxides were synthesized using a unique solid-state methodology to probe the effect of palladium addition on sulfur dioxide adsorption. The addition of palladium to this model system is shown to have a strong effect on the magnitude of adsorption for sulfur dioxide on some material/exposure condition combinations. Ceria/zirconia sulfite and sulfate species are identified on the palladium-loaded MMO materials with adsorption sites located on the exposed oxide sites.

DEDICATION

This Dissertation is Dedicated to my unborn Child.

May your journey of life be a joy;
a tale of travels down untrodden trails.

ACKNOWLEDGEMENTS

This dissertation would have been impossible for me to complete without the support of family and friends.

To Kirk Schulz, thank you for believing in me and allowing me to continue with your research. You have been a great mentor, advisor, and friend.

To the members of my graduate committee I give my utmost thanks for your time spent on this work and your judicious concern over my professional development.

To my parents, Esteban and Maria, thank you for supporting and encouraging me with everything.

To my wife, Amanda – my educational goals would never have been met without your undaunted love and support over the years. I love you.

Thank you, Mr. Doss and Martha Brodnax, for your friendship and for allowing me to live and play at Pinedale Farm during these years.

To Rye and Simon – rain or shine, you fellows always cheer me up. You have both been highly dedicated writing companions.

Thank you God, for the strength you've given me to finish this work and move on.

TABLE OF CONTENTS

Page

DEDICATION ii

ACKNOWLEDGEMENTS iii

LIST OF TABLES vii

LIST OF FIGURES viii

CHAPTER

I. INTRODUCTION 1

- 1.1 Introduction 1
- 1.2 Automotive Emissions Inventory 3
  - 1.2.1 Fuel Formulation Changes 4
  - 1.2.2 Durability of Emissions Control Devices 5
  - 1.2.3 Fuel Sulfur Content 7
- 1.3 Technological Advancements 8
  - 1.3.1 Modern Catalytic Converter Construction 10
  - 1.3.2 Chemical Composition 11
- 1.4 Operational Considerations and Phenomena 14
  - 1.4.1 Deactivation Mechanisms 16
  - 1.4.2 Sulfur Deactivation 18
- 1.5 Research Objective 20

II. EXPERIMENTAL METHODS 23

- 2.1 Mixed-Metal Oxide Synthesis 23
- 2.2 Sample Preparation 24
- 2.3 X-ray Photoelectron Spectroscopy Fundamentals 25
- 2.4 In-situ Characterization of SO_2 Adsorption 28
- 2.5 In-situ Reaction Cell Heating System 31
  - 2.5.1 Introduction 31
  - 2.5.2 UHV System Description 33
  - 2.5.3 Reaction Cell Design 34

CHAPTER Page
- 2.5.4 Heating System Design 37
- 2.5.5 Heater Operation 46
- 2.6 Experimental Conditions 47

III. SO_2 ADSORPTION ON CSZ MIXED-METAL OXIDES 50

- 3.1 Apparatus Parameters 50
- 3.2 Data Acquisition 51
- 3.3 Sample Temperature and Composition Effects 52
- 3.4 Sulfur Line Analysis 57
- 3.5 Discussion 61
  - 3.5.1 Sulfate and Sulfite Surface Species Identification 61
  - 3.5.2 Effect of Temperature on SO_2 Adsorption 65

IV. CZMMO OXYGEN PHOTOEMISSION 67

- 4.1 Oxygen 1s High Resolution Photoemission Spectra 67
- 4.2 Terminal Hydroxyl Groups on Metal Oxides 69
- 4.3 Previous XPS Investigations on Ceria 71
- 4.4 Data Acquisition 73
- 4.5 Results 74
  - 4.5.1 O(1s) Spectral Symmetry 74
  - 4.5.2 Curve Peakfitting 80
- 4.6 Discussion 93

V. CZMMO CERIUM AND ZIRCONIUM PHOTOEMISSION 96

- 5.1 High Resolution Photoemission Spectra of Ce and Zr 96
- 5.2 Cerium Photoemission 99
  - 5.2.1 Overview 99
  - 5.2.2 XPS Spectral Features of Cerium Oxide 99
  - 5.2.3 Determination of Oxidation State 100
- 5.3 Data Acquisition 102
- 5.4 Results 103
- 5.5 Discussion 108

VI. PALLADIUM CZMMO PHOTOEMISSION 111

- 6.1 Introduction 111
- 6.2 Performance of Palladium Catalysts 112
- 6.3 Adsorption of SO_2 on Palladium Catalysts 114
- 6.4 Modeling of Ceria-Zirconia Supported Palladium 115

CHAPTER Page

6.4.1 Real Precious Metal Loaded Catalysts 115
6.4.2 Metal-Support Interfacial Sites and Synthesis 117
6.4.3 FESEM/EDX Characterization of Model System 118
6.4.4 Preliminary XPS Characterization of Model System 123
6.5 SO_2 Adsorption Studies 128
6.5.1 SO_2 Exposure Conditions 128
6.5.2 Results 129
6.6 Discussion 136

VII. CONCLUSIONS 140

VIII. RECOMMENDATIONS FOR FUTURE RESEARCH 143

REFERENCES 147

LIST OF TABLES

TABLE Page

1.1 Federal Automotive Exhaust Emission Standards 6

1.2 EPA Gasoline Sulfur Standards (2004-2006) 7

1.3 Percent Change in Air Pollutant Emissions.......................... 9

3.1 Reported literature values for binding energies and species identified during photoemission experiments conducted for SO_2 adsorption on ceria 62

4.1 Reported literature values for O(1s) binding energies (eV) of reported species identified during photoemission (XPS) experiments on cerium oxides [58,62] 72

4.2 Reported values for O(1s) XPS binding energies of reported species on pure ceria and zirconia metal oxides. Exposure conditions of 15 min., 20 ppm SO_2, 1000 T, and 673 K 87

4.3 Relative O(1s) peak areas attributed to hydroxy and lattice oxygen atoms prior to treatment with SO_2 for all CZMMO compositions examined 88

4.4 Relative O(1s) peak areas attributed to hydroxy and lattice oxygen atoms after 15 minute exposure to 20 ppm SO_2 at 1000 T and the temperature listed in the table for all CZMMO compositions examined 89

LIST OF FIGURES

FIGURE Page

1.1 Surface analysis system used in this study with in-situ XPS capabilities and incorporating metal-sealed ultra-high vacuum conditions 22

2.1 Diagram of the UHV system employed in this study 35

2.2 Custom-built extension rod dimensions and layout................. 38

2.3 Platen fork and heating element arrangement diagram............ 40

2.4 Channelized boron nitride insulator diagram 43

2.5 Heating system performance graph 49

3.1 High resolution XPS spectra after SO_2 exposure at 473 K for six compositions, (a) Ce/Zr=1:0, (b) Ce/Zr=9:1, (c) Ce/Zr=7:3, (d) Ce/Zr=5:5, (e) Ce/Zr=2:8, (f) Ce/Zr=0:1 53

3.2 High resolution XPS spectra for ZrO_2 before (b) and after (a) exposure to SO_2 at 673 K showing the three lobed zirconia 3d satellite feature encountered in this energy range 54

3.3 High resolution XPS spectra after SO_2 exposure at 673 K for six compositions, (a) Ce/Zr=1:0, (b) Ce/Zr=9:1, (c) Ce/Zr=7:3, (d) Ce/Zr=5:5, (e) Ce/Zr=2:8, (f) Ce/Zr=0:1 56

3.4 Plot of S(2p) normalized peak area vs. ceria (or zirconia) molar ratio for exposures to SO_2 at 298, 473, and 673 K.. 58

3.5 S(2p) curve deconvolution for pure ceria exposed to SO_2 at 673 K.. 59

FIGURE Page

3.6 Plot of sulfate-to-sulfite area ratio vs. ceria mole fraction for exposures to SO_2 at temperatures of 298, 473, and 673 K........ 60

4.1 High resolution O(1s) XPS spectra of pure ceria taken (a) prior to exposure and (b) after a 15 minute exposure to 20 ppm SO_2/N_2 gas at 673 K and 1000 torr 75

4.2 High resolution O(1s) XPS spectra of pure zirconia taken (a) prior to exposure and (b) after a 15 minute exposure to 20 ppm SO_2/N_2 gas at 673 K and 1000 torr 76

4.3 High resolution O(1s) XPS spectra of pure ceria taken (a) prior to exposure and (b) after a 15 minute exposure to 20 ppm SO_2/N_2 gas at 673 K and 1000 torr 77

4.4 High resolution O(1s) XPS spectra of pure zirconia taken prior to exposure (dashed), and after a 15 minute exposure to 20 ppm SO_2/N_2 gas at 673 K and 1000 torr (solid line) 78

4.5 High resolution O(1s) XPS spectra and curve deconvolution for pure ceria taken prior to SO_2 exposure. Peak A is attributed to metal oxide lattice oxygen atoms and Peak B is due to oxygen atoms bound in surface hydroxyl groups 81

4.6 High resolution O(1s) XPS spectra and curve deconvolution for pure ceria taken after a 20 ppm SO_2 gas exposure at 673 K and 1000 T for 15 minutes. Peak A is attributed to metal oxide lattice oxygen atoms and Peak B is due to oxygen atoms bound in surface hydroxyl groups 82

4.7 High resolution O(1s) XPS spectra and curve deconvolution for pure zirconia taken prior to SO_2 exposure. Peak A is attributed to metal oxide lattice oxygen atoms and Peak B is due to oxygen atoms bound in surface hydroxyl groups 83

FIGURE Page

4.8 High resolution O(1s) XPS spectra and curve deconvolution for pure zirconia taken after a 20 ppm SO_2 gas exposure at 673 K and 1000 T for 15 minutes. Peak A is attributed to metal oxide lattice oxygen atoms and Peak B is due to oxygen atoms bound in surface hydroxyl groups 84

4.9 Percentage of O(1s) peak area attributed to hydroxyl (-OH) oxygen species, prior to any treatment 91

4.10 Percentage of O(1s) XPS peak area attributed to hydroxyl (-OH) oxygen species, after a 15 minute 20 ppm SO_2/N_2 treatment at 1000 T and 298, 473, or 673 K 92

5.1 High resolution Zr (3d) XPS spectra of pure zirconia taken (a) prior to exposure and (b) after a 15 minute exposure to 20 ppm SO_2/N_2 gas at 673 K and 1000 torr pressure 98

5.2 High resolution Ce (3d) XPS spectra for ceria taken (a) prior to any treatment and (b) after 15 minutes of 1.5 keV Ar^+ ion sputtering at θ=138° 105

5.3 High resolution Ce (3d) XPS spectra for ceria taken (a) prior to any treatment and (b) after a 15 minute exposure to a 20 ppm SO_2/N_2 gas at 673 K and 1000 T 107

6.1 Sweep test results comparing Pd-only and Pt/Rh TWC formulations for the conversion of CO, HC, and NOx emissions [2].. 113

6.2 FESEM micrograph of a Pd-ceria compacted wafer of the type used in SO_2 adsorption studies (x 22,000). Rectangular areas labeled 1 and 2 were selected for EDX analysis 120

6.3 EDX spectra for two areas selected on the Pd-ceria wafer shown in Figure 6.2. This data demonstrates that Area 1, with the rough morphology, corresponds to palladium metal. Area 2, with smooth morphology, is identified as ceria 121

FIGURE Page

6.4 XPS survey scan for as-synthesized palladium-ceria wafer with corresponding Ce(3d) and Pd(3d) regions delineated and shown as inset XPS high resolution scans 124

6.5 XPS survey scan for as-synthesized palladium-zirconia wafer with corresponding Zr(3d) and Pd(3d) regions delineated and shown as inset XPS high resolution scans 125

6.6 XPS survey scan for as-synthesized palladium-zirconia-ceria MMO wafer with corresponding Ce(3d), Zr(3d), and Pd(3d) regions delineated and shown as inset XPS high resolution scans 126

6.7 XPS spectra after SO_2 exposure at 473 K for six MMO compositions, each with a palladium loading of 10 mass% (a) Ce/Zr=1:0, (b) Ce/Zr=9:1, (c) Ce/Zr=7:3 (d) Ce/Zr=5:5, (e) Ce/Zr=2:8, (f) Ce/Zr=0:1 130

6.8 XPS spectra after SO_2 exposure at 673 K for six MMO compositions, each with a palladium loading of 10 mass% (a) Ce/Zr=1:0, (b) Ce/Zr=9:1, (c) Ce/Zr=7:3 (d) Ce/Zr=5:5, (e) Ce/Zr=2:8, (f) Ce/Zr=0:1 131

6.9 Compilation of S 2p peak areas obtained using high resolution XPS after a 15 min SO_2 exposure at 1000 T for six MMO compositions (x-axis). Solid lines and filled symbols denote the results obtained for base MMO's while dashed lines and hollow symbols represent MMO's loaded with 10 mass% palladium 134

7.1 Graphic showing the formation of singly-coordinated hydrogen sulfite species and doubly-bridged sulfate species on the partially hydroxylated surface of ceria/zirconia 142

CHAPTER I

INTRODUCTION

1.1 INTRODUCTION

Ambient air quality has been an important topic for the environmental community for more than thirty years. The Clean Air Act of 1970 and the Amendments to the Clean Air Act in 1977 and 1990 have established the need for the scientific community to stay involved with research in technology used for the abatement of pollutants from any source [1]. With a growing world population, sprawling urban areas, and the increased demand for many products produced at industrial sites, it is increasingly important for society to maintain or improve the status of air quality. In response, lawmakers have written laws and regulations that incorporate higher standards for air quality that must be addressed in the years to come by every facet of industry.

Over the past three decades, heterogeneous catalysts have been developed, used, and the subject of intense research in the abatement of air pollutants [1]. Perhaps the most widely known application of heterogeneous catalysis for the abatement of air pollutants is in automotive applications [2]. Here, devices known as catalytic converters and diesel particulate traps have been designed in a concerted effort over the last three decades to address the emission of hydrocarbons, carbon monoxide, nitrogen oxides, and particulates emitted from automobiles and trucks [1]. Continual advancement of these devices is necessary in response to the implementation of more stringent transportation emissions standards. The life cycle of a particular device such as a catalytic converter can be considered to be the time period that the converter operates effectively for the conversion or abatement of the targeted pollutants. Various fuel contaminants, such as sulfur, can have a significant detrimental effect on the length of a catalytic converter's life cycle.

Sulfur-bearing compounds, which are always found to some extent in fuels derived from crude petroleum, are a known poison for catalytic converters [2]. During combustion in an internal combustion (IC) engine, sulfur-bearing impurities in the fuel will typically be oxidized and form a variety of sulfur compounds. Of the sulfur compounds produced, sulfur oxides are the most common, but the release of hydrogen sulfide has also been reported in the literature from the reduction of sulfates under fuel-rich combustion conditions [2]. As the gaseous exhaust passes through a catalytic converter, the sulfur species present tend to chemisorb irreversibly and selectively poison the catalysts' active sites [2]. The sulfur content of automotive fuels has been identified by the U.S. Environmental Protection Agency (EPA) as a threat to emissions control because of the detrimental effect sulfur compounds have on emissions control systems [3]. A more complete understanding of the actual mechanism by which sulfur compounds adsorb on typical catalyst materials is needed and is the basis of the research objective in this study.

1.2 AUTOMOTIVE EMISSIONS INVENTORY

Gasoline and diesel engines emit a significant amount of polluting compounds. Up to half of the United States' emissions of nitrogen oxides (NO_x), volatile organic compounds (VOCs), and hazardous air pollutants (HAPs) come from internal combustion engines [1]. Even a larger proportion, up to 95 percent, of all atmospheric carbon monoxide found in cities is released from IC engines [4].

In 1970, the American population traveled an estimated 1 trillion miles in automobiles, and this figure has risen each year to a level of approximately 2.5 trillion miles in 1997 [5]. Each year, the number of driven miles is expected to increase by 2 or 3 percent [5]. This rise in driven miles is due to many factors, which can include the increase in population, cheap and readily available fuels, and the general progress and prosperity of American society.

1.2.1 Fuel Formulation Changes

In addition, emissions can increase by changes in the fuels' formulation. For example, the elimination of tetraethyl-lead from commercial gasoline has led to the inclusion of other octane boosting additives, which are also considered to be oxygenates. Adding oxygenates, such as methyl-tert butyl ether (MTBE) or ethanol, to fuel is equivalent to adding oxygen to the combustion mixture [6]. If all other engine operating parameters are held constant, this addition will make the combustion mixture increasingly fuel-lean, and hence, more likely to produce larger percentages of NO_x pollutants, especially at higher combustion temperatures [2,6,7]. The incorporation of oxygen sensors in IC engine exhaust are intended to provide advanced control of air-fuel stoichiometry to minimize the production of unwanted emissions and increase fuel economy [2]. However, these sensors cannot detect oxygen bound in different oxygen-containing compounds such as CO, NO_x, and oxygenates [2,8,9]. Oxygen sensors are designed to detect only unreacted or excess diatomic oxygen. For this reason, the addition of ethanol to gasoline blends is purported to increase the photochemical production of ground-level ozone [7]. All commercially available gasoline, diesel, and aviation fuels are complex and variable mixtures of hundreds of paraffinic, aromatic, and other organic compounds [6,10,11].

1.2.2 Durability of Emissions Control Devices

Early emissions control catalysts had a required life cycle of about 50,000 miles under the requirements of the original Clean Air Act of 1970 [2]. However, a more recent amendment to the Clean Air Act, passed in 1990, established a higher standard for converter durability of 100,000 miles for new automobiles built after the year 1996 [2]. Future requirements for durability will likely undergo increases in the years to come. The premise behind this durability enhancement is the decrease in emissions control effectiveness obtained from converters installed on older vehicles whose effective transportation life is being extended. All catalyst poisoning and deactivation processes will directly impact the attainment of more stringent performance criteria that will be encountered in the future. Table 1.1 shows the gradual development of EPA exhaust limits on hydrocarbon, carbon monoxide, and nitrogen oxides imposed on automobile manufacturers since 1970 for new passenger cars as tested under the Federal Test Procedure (FTP) 75 cycle [1].

Table 1.1 Federal Automotive Exhaust Emission Standards

	Maximum Emissions (grams/mile)		
Year	HC	CO	NO_x
Pre-Control (estimated)	10.6	84	4.1
1970	4.1	34	-
1977	1.5	15	2.0
1981	0.41	3.4	1.0
1994	0.25	3.4	0.4
1994 (TLEV)	0.125	3.4	0.4
1997 (LEV)	0.075	3.4	0.2
1997-2003 (ULEV)	0.040	1.7	0.2
ZEV	-0-	-0-	-0-

Transitional low emission vehicles (TLEV), low emission vehicles (LEV) and ultra-low emission vehicles (ULEV) are considered to be currently available gasoline and gas-electric hybrid automobiles [2]. The zero emission vehicle (ZEV) is generally considered to consist of certain hydrogen fuel cell powered or electric powered automobiles [2].

Over the years, the implementation of these limits into law has prompted a great deal of research in order to comply with these limits in practice. However, the effect of sulfur on the long-term performance of catalytic converters remains a significant problem, even in light of more stringent fuel sulfur regulations.

1.2.3 Fuel Sulfur Content

The EPA also sets standards for sulfur content which, must be met by petroleum refiners [3]. Now that sulfur deactivation of emission control catalysts is a well known phenomena, there are several options for legislators to choose from to ensure that the federal emission standards are met. One of the available options is to remove sulfur-bearing compounds from petroleum fuels to levels that would prolong emission control catalyst effectiveness to acceptable life cycles. Table 1.2 is a summary of recent federal regulations involving fuel sulfur content in gasoline fuels [5]. The fuel sulfur content allowed for diesel fuels is also regulated, but somewhat higher levels are allowed at this time.

Table 1.2 EPA Gasoline Sulfur Standards (2004-2006)

	Sulfur Content (ppm)	
Year	Production Cap	Corporate Average
2004	300	120
2005	300	90
2006	80	30

In the state of California, due to its more severe smog and air pollution issues, is the only state that has its own regulations concerning all air quality issues [2,7]. In every regard, the regulations are more stringent in California than the laws implemented elsewhere in the United States

[7]. However, it has been shown that a typical 300 ppm sulfur gasoline produces a 20 ppm sulfur dioxide (SO_2) concentration in the exhaust gas stream [12]. Even with reductions in the sulfur levels encountered in gasoline, there will always be some level of sulfur impurities present in crude oil derived fuels, and therefore, long-term catalyst deactivation concerns will remain. Additionally, the cost of removing sulfur from fuels at the refinery is expensive and highly variable due to differences in crude petroleum feed source [3]. In general, low sulfur crude petroleum is more expensive than high sulfur crude petroleum. One estimate puts the cost increase for 40 ppm sulfur gasoline at 8 cents per gallon, while another estimate gives less than 2 cents per gallon increase for 30 ppm sulfur gasoline [3,5]. As petroleum reserves are consumed, the quality of the remaining reserves will decrease, making the feed more difficult to refine into ultra-clean products because of the higher levels of impurities that exist in those lower quality crude oils. Ultimately, the design of a catalyst that is tolerant of sulfur and any other deactivating condition or impurity would be the answer to this challenging problem.

1.3 TECHNOLOGICAL ADVANCEMENTS

The past couple of decades have been marked by significant strides in the abatement of air pollutants from all sources. Table 1.3 shows the progress made in reducing the emissions of nitrogen oxides, volatile organic compounds, sulfur dioxide, particulate matter (PM_{size}, in microns), carbon monoxide, and lead in two overlapping time periods since 1983 [4].

Table 1.3 Percent Change in Air Pollutant Emissions From All Sources

Pollutant	Percent Change in Emissions 1983-2002	Percent Change in Emissions 1993-2002
NO_x	-15	-12
VOC	-40	-25
SO_2	-33	-31
PM_{10}	-34	-22
$PM_{2.5}$	-	-17
CO	-41	-21
Pb	-93	-5

These gains are attributable to the implementation of legislation, such as the Clean Air Act, which then motivates the necessary technological advancements through extensive research at various research centers. During the same time, from 1983 to 2002, the U.S. Gross Domestic Product (GDP) has increased 114%, vehicle miles traveled has increased 105%, total energy consumption has increased by 28%, and the U.S. population has increased by 28% [4]. Of direct interest to the subject of automotive emissions is the 25% increase from 1983 levels in the U.S. national consumption of gasoline fuels in the year 2002 [13]. The development of catalytic converters in the automotive industry has been instrumental in the realization of these air quality improvements in light of increased usage of gasoline fuels. However, catalytic converters will need to perform at even higher levels in the future as environmental regulations become more stringent.

To perform at the higher levels needed for compliance with more demanding environmental laws, many aspects of converter design will have to be revisited. Thermal stability, selectivity for the desired reactions, durability, and resistance to deactivation processes are all subjects that will need to be technically advanced as catalytic converters progress. Over the years, numerous advancements have been made with respect to these and other subjects, but there is still no viable solution to the treatment of sulfur dioxide in the deactivation of current catalysts.

1.3.1 Modern Catalytic Converter Construction

Modern commercial catalytic converters are generally constructed using a low surface area ceramic monolith as the catalyst support [2]. The large open frontal area of these parallel channel honeycomb structures provides a very low pressure drop which translates into negligible power loss for the vehicle [2]. First generation converters employed pelleted catalysts that had unfavorable pressure drop characteristics, and these catalysts suffered from gradual attrition due to vibration [2,12]. The most commonly used material for this monolithic catalyst support is synthetic cordierite ($2MgO \cdot 2Al_2O_3 \cdot 5SiO_2$), but metal monoliths are becoming more popular due to the thinner walls that can be produced [2,14]. Typically, the high surface area catalyst is deposited on the low surface area monolith by some dipping process followed by calcination [2]. A washcoat, usually an aqueous solution that contains the active metal and carrier precursory materials, is used in the dipping process which then deposits the catalyst onto the monolith walls after calcination [2]. The exact manufacturing details and compositions are kept as trade secrets, but in general, noble metals such as platinum (Pt), palladium (Pd), and rhodium (Rh) are incorporated with certain high surface area carriers and promoters [2]. Various metal oxides such as alumina, baria, lanthana, ceria and zirconia are used for the high surface area carrier in varying proportions [2,14]. After calcination, the monolithic catalyst is usually inserted in an insulated metal canister, which is then easily incorporated into the exhaust line of any automobile.

1.3.2 Chemical Composition

The catalyst used in modern catalytic converters is called a three-way catalyst. This name was given because these materials are designed for the abatement of three principal pollutants encountered in automobile exhaust, NO_x, CO, and hydrocarbons. The chemical composition of the catalyst used in catalytic converters is variable and details are held as proprietary trade secrets. However, generalizations can be made about several key components of interest in this study.

For a three-way catalyst to function as designed, an oxygen buffer, otherwise known as oxygen-storage-capacity (OSC), must exist so that oxygen can be released from the catalyst during oxidizing conditions and adsorbed during reducing conditions [15]. Ceria is well known for its unique ability as an OSC component [2,15,16]. Ceria undergoes a reversible reaction from a +IV oxidation state to a +III oxidation state quickly and easily as in the following equation:

$$4\ CeO_2 \leftrightarrow 2\ Ce_2O_3 + O_2 \qquad (1)$$

In the fully oxidized +IV state, ceria provides the necessary oxygen for the oxidation of carbon monoxide and hydrocarbons to carbon dioxide while reduced +III ceria adsorbs oxygen into the crystalline lattice from nitrogen oxides to yield diatomic nitrogen [12]. However, pure ceria shows approximately 98 percent loss of surface area after just 12 hours at 1323 K [16]. For this reason, zirconium oxide has become an important component to improve the thermal stability of the modern emissions catalyst [15,16]. Solid solutions of ceria and zirconia have shown thermal stability to temperatures in excess of 1273 K while maintaining desirable OSC properties [16]. Temperatures encountered in a commercial catalytic converter can reach 1000 K or higher due to extreme driving conditions or because of close-coupling of the converter to the exhaust manifold for faster light-off or the abatement of start-up pollutants [2,16]. Additionally, zirconia shows unique oxygen ion conduction properties that should provide some benefit to the overall OSC of the catalyst by easing the transport of oxygen in the crystalline lattice [2]. Because of this unique property, zirconia-based technology has enabled the development of modern oxygen sensors mentioned in section 1.2.1. Together, ceria and zirconia show much promise in the field of catalytic air pollution control [15].

In commercial three-way catalysts, the most important catalytically active sites occur at the sites where certain noble metal particles are in intimate contact with support or promoter metal oxide, such as ceria [2,17]. Using high-resolution transmission electron microscopy (HRTEM), it has been found that these catalytically active areas are found at interfacial sites where the noble metal particles coexist side-by-side with ceria particles [17]. This experimental proof is contrary to the long-held position in the catalysis community that the noble metal particles must be deposited onto the surface of such metal oxides [17].

The noble metals, such as platinum, rhodium, and palladium, are very expensive components used in the manufacture of these devices. Platinum and palladium are the two metals which were employed in the first generation catalytic converter (1976-1979). This first generation catalyst was generally considered to be an oxidation catalyst [2]. The second generation catalytic converter (1979-1986) was modified to provide reduction of NO_x. Platinum and rhodium were the metals found to be the most active for the simultaneous oxidation of CO and reduction of NO_x [2]. High loadings of ceria were employed in the second generation converter because of the discovery of its unique OSC properties which eliminated the need for a two-stage reactor [2]. Rhodium is among the most expensive of all metals at approximately $200 per gram [18]. In addition, the invention of the modern oxygen sensor during these years enabled more precise control over the air-fuel stoichiometry [2]. However, the third generation catalytic converter (1986-1992) needed to withstand much higher temperatures due to increased fuel economy operational strategies and higher average driving speeds [2]. At high temperatures, rhodium experiences very undesirable reactions with alumina and other metal oxides [2]. This is still an active area of research. However, palladium resurfaced in the middle 1990's as a possible replacement for platinum and/or rhodium in the fourth generation converter due to its lower cost and suitable performance characteristics. The fourth generation three-way catalyst will contain palladium in conjunction with metal oxides such as ceria and zirconia [2].

1.4 OPERATIONAL CONSIDERATIONS AND PHENOMENA

As described in the previous sections, reactions occur inside the catalytic converter to yield a benefit to the environment and human well-being by destroying harmful pollutants and creating benign or otherwise unregulated gases. All of the reactions occurring in a catalytic converter can be classified as reduction or oxidation reactions [2]. A vehicle's exhaust is comprised of many gases, and ideally, catalytic converters will effectively convert each into unregulated species. The three principal pollutants created in combustion chambers include nitrogen oxides (NO_x), carbon monoxide (CO), and non-methane hydrocarbons (NMHC) from incomplete fuel combustion. In the case of NO_x, the catalyst must be able to reduce these species to harmless nitrogen gas. In order to be able to accomplish this task, the catalyst must be able to adsorb oxygen into its crystalline lattice or on other active sites while providing a path for nitrogen ions to combine and form diatomic nitrogen gas. In the case of NMHC and CO, the catalyst must be able to release oxygen from its crystalline lattice or other active sites so that these compounds may be completely oxidized to water and carbon dioxide (CO_2). Exhaust gas mixtures will contain some amount of each of NO_x, CO, and NMHC at any given time and under any fuel-to-air stoichiometry [14]. Under certain circumstances, the exhaust gas mixture can be rich in any one of these pollutants. The air-to-fuel stoichiometry has a significant impact on what particular combustion products are formed [2,14]. Fuel rich instances would give increasingly higher levels of CO and HC emissions due to the excess amount of fuel present in the combustion chamber for the fixed amount of air (and hence oxygen for combustion). With higher temperatures and fuel lean conditions the formation of NO_x is increased because the combustion conditions are optimal for the production of NO_x as delineated in the Zeldovich mechanism [2,19]. Therefore, the catalyst must be able to handle a variety of exhaust compounds, oxidizing some while selectively reducing others. Additionally, research has shown that a very significant portion of all hydrocarbon emissions (60 to 80 percent) are emitted during the cold-start segment of automobile operation [2]. The cold-start segment occurs during the first 2 minutes after starting the engine when the engine and catalyst are at ambient temperature [2]. During a cold starting segment, the catalytic reactions are mass transport limited and do not occur [2]. However, after gradual heating, the catalyst reaches a temperature known as the light-off temperature and the reaction rate is then controlled by chemical kinetics [2].

1.4.1 Deactivation Mechanisms

Deactivation processes can occur due to many different conditions. Combustion of contaminants in the fuel leads to the formation of known poisons for emissions control catalysts. The combustion of such contaminants may produce compounds that form stable complexes on the catalyst surface which can alter the activity of the catalyst. Fuel sulfur is the topic of this study, but other poisoning impurities do exist [2]. When lead was still used as an octane booster, severe deactivation occurred due to lead deposition [12]. Other contaminants can consist of phosphorous and zinc that are present in lubricating motor oils in the form of zinc dialkyldithiophosphate (ZDDP) [2]. The poisoning due to the adsorption of impurities remains a topic of active research.

Thermal deactivation is the loss of catalytic activity due to exposure of the catalyst to damaging temperatures. Some catalytic components are not thermally stable at the exhaust operating temperatures of modern automobiles. This problem is aggravated with the modern engine control strategies that increase fuel economy while the average speed used on roadways is also increasing with time [2]. Ultimately, these operating conditions produce exhaust streams that are of higher temperature than those found in older vehicles. Significant noble metal encapsulation has been observed for various compositions of Pd-ceria-zirconia catalysts at temperatures of 1323 K [15]. Encapsulation and loss of surface area due to sintering are the result of catalyst exposure to damaging temperatures.

Physical deactivation is another detrimental process that can occur when particulate matter physically blocks the exhaust gases from contacting the catalyst or active sites. The generation of particulates can be the result of engine operation (e.g. diesel engines) or some other factor. The combustion design of diesel engines leads to high particulate emissions relative to gasoline engines [2,11]. The high level of particulates under normal diesel engine operating conditions requires different strategies when addressing diesel emissions versus gasoline engine emissions [2]. Additionally, unlike gasoline engines, the air-fuel stoichiometry in diesel engines is always fuel-lean, yielding low levels of NMHC and CO emissions from diesel engines [2]. Therefore, the rationale used in the design of diesel particulate traps is significantly different than that used in designing three-way catalytic converters for use on gasoline engines. Loss of catalytic washcoat adhesion with respect to ceramic or metal monoliths can be a source of pore-clogging particulates [2]. Similarly, pelleted catalyst beds suffer from gradual pellet attrition due to constant vibration of the packed bed. Unfortunately, not only does this scenario cause loss of catalyst, but also forms particulates, which can become a barrier for exhaust gases. Additionally, different combustion and fuel properties contribute to particulate matter formation in the combustion chambers of engines. The EPA has classified 2 size ranges of these particulate emissions to be regulated [4]. The two sizes of particulate matter (PM) that are regulated by the EPA include 2.5 micron ($PM_{2.5}$) and 10 micron (PM_{10}) [4]. These sooty particles can act in the same manner as the other particulates mentioned above by becoming a physical barrier between the gaseous reactants and the catalyst.

1.4.2 Sulfur Deactivation

The effect of sulfur on three-way-catalysts (TWC) has been a persistent subject over the years, but no viable solution yet exists [2,12,15]. As mentioned in section 1.2.3, one possibility is to circumvent the catalyst deactivation problem by removing sulfur from fuels [5,6]. However, this can prove costly to the consumer and refiner. Another potential solution would involve the design of sulfur-tolerant catalysts that are capable of achieving the same benefit to society.

Researchers at private corporations, universities, and national laboratories have undertaken studies to better understand the phenomena of sulfur deactivation on materials used in TWCs. The number of works in the literature attests to the importance of the subject. Sulfur deactivation was first observed when first generation emission-control oxidation catalysts were found to “store” sulfur during standard FTP tests in the early 1970’s [20]. Over the next several years, more advanced analytical techniques were developed. This technology advancement has permitted much more detailed examinations of these particular interactions. One later study found that upon exposure to SO_2 at various conditions, sulfates (SO_4^{2-}) and sulfites (SO_3^{2-}) formed on typical commercial TWC carrier materials, while elemental sulfur formed on the noble metals in the catalyst [21]. However, the complexity of catalyst compositions has warranted fundamental studies that probe the effect of SO_2 on the individual components used in commercial catalysts. Such fundamental studies can contribute pieces of information that catalyst designers may use to develop improved catalysts in the future.

1.5 RESEARCH OBJECTIVE

The objective of this study includes the determination of surface sulfur species formed on palladium-loaded and base cerium and zirconium oxide solid solutions after exposure to SO_2 at realistic automobile temperatures and partial pressures of SO_2. Ceria-zirconia mixed-metal oxides (MMO) and palladium will continue to play an important role in future emissions control systems as discussed in section 1.3.2. The materials used in this study will include co-precipitated polycrystalline powders. The technique used for the determination of surface oxidation states is x-ray photoelectron spectroscopy (XPS). The justification for this study comes from the lack of in-situ photoemission studies on a realistic set of materials in this compositional range.

In order to attain the research objective, various MMO compositions will be synthesized in the laboratory as described elsewhere

[22-24]. The raw MMO materials will be characterized using scanning and transmission electron microscopy, energy dispersive x-ray spectroscopy (EDX), and XPS. An existing ultra-high vacuum (UHV) system (shown below in Figure 1.1) with XPS capabilities and an in-situ reaction cell will then be used to probe the SO_2 interaction. Design and construction of a reaction cell heating system is required as a part of this objective in order to allow realistic temperatures to be attained in the reaction cell. In addition to studies employing the base MMO compositions, palladium loaded samples will be used in an effort to investigate the interaction of SO_2 with the interface between the MMO and palladium metal particles.

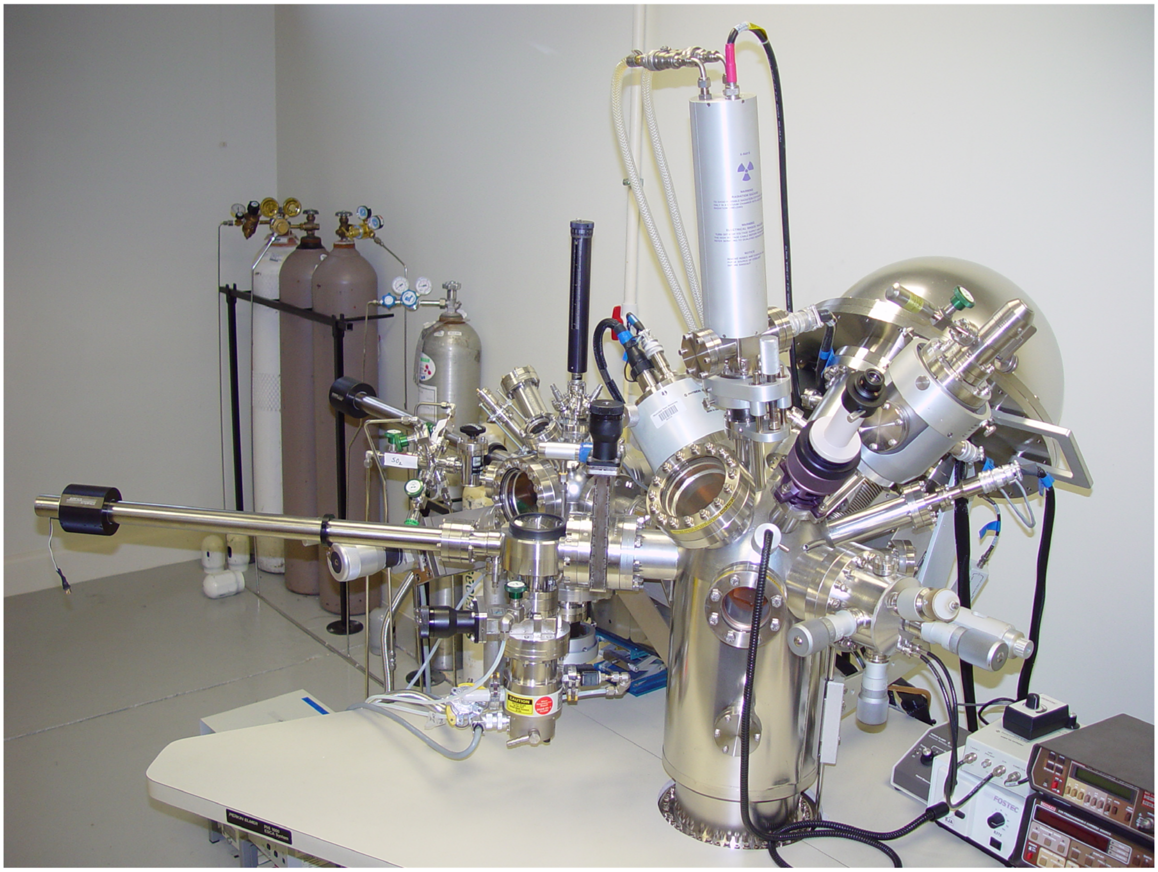

Figure 1.1 Surface analysis system used in this study with in-situ XPS capabilities and incorporating metal-sealed ultra-high vacuum conditions

CHAPTER II

EXPERIMENTAL METHODS

2.1 MIXED-METAL OXIDE SYNTHESIS

Mixed-metal oxides were synthesized using a co-precipitation technique described elsewhere [22-24]. Aqueous solutions of cerium ammonium nitrate (CAS #16774-21-3) and zirconium oxynitrate (CAS #13826-66-9) were prepared under mild heating (at a temperature of approximately 323 K) and manual agitation with a pyrex stirring rod. Typically, 200 milliliters of distilled water was used to make approximately 4 grams of MMO powder. However, the final mass produced varied slightly depending on the composition, since the molar weight of ceria and zirconia are different. Upon dissolution, the pH of the precursor salt solutions was adjusted using an equivalent volume of pure ammonium hydroxide. Each precipitated solid batch of different composition was filtered and subsequently rinsed with 2 liters of distilled water using a vacuum funnel and filter paper. The filter cake was calcined in air at 773 K for one hour to remove entrained water and decompose residual nitrate and ammonium groups. The resulting crystals were then ground into a fine powder using a ceramic mortar and pestle. The powder was then stored in air tight glass vials for use at a later date. Previous BET surface area measurements taken for MMO's synthesized in the same exact fashion ranged from 34 to 85 m^2/g, with increasing surface areas reported for higher zirconia substitutions [22]. In addition, previous powder XRD data showed that powders synthesized in this exact fashion are polycrystalline solids [22].

2.2 SAMPLE PREPARATION

The techniques used for sample preparation can be categorized with respect to the analytical technique employed. For SEM analysis, double sided copper or carbon tape was used to fix powder particles or sample wafers onto sample dollies prior to coating with a gold-palladium conduction coating. SEM was also performed on uncoated MMO powders so that the full benefit of EDX analysis could be attained, but sample charging limited micrograph quality under these conditions.

For TEM analysis, polyvar coated copper grids were used to fix small quantities of MMO powders. Microtomed thin-sections of embedded MMO powders were also used on coated copper grids. Limitations were encountered with higher zirconia molar ratios due to the inherent hardness of zirconia, which is similar to the hardness of the diamond used as the cutting edge for thin-sectioning.

For insertion into the UHV apparatus used in photoemission experiments, the sample powders were pressed into flat and thin wafers using a standard 13 mm FTIR potassium bromide pellet press at pressures of approximately 800 MPa. The resulting wafers were approximately 0.1 mm in thickness. The resulting wafers were delicate to the touch and were fractured into smaller pieces for loading onto 1” sample platens. In general, the pieces used in this analysis were from 3 to 4 mm in diameter, which was sufficient for the system used since the spectrometer spot-size is 0.8 mm in diameter.

2.3 X-RAY PHOTOELECTRON SPECTROSCOPY (XPS) FUNDAMENTALS

X-ray photoelectron spectroscopy (XPS) or electron spectroscopy for chemical analysis (ESCA) is an ultra high vacuum technique used for surface chemical characterization. The technique was developed by Kai Siegbahn, a 1981 recipient of the Nobel Prize in Physics, at the University of Uppsala, Sweden in the mid 1960’s [25]. The principle behind XPS is Einstein’s photoelectric effect, in which incident photons cause electrons to be emitted after striking a solid material. Electrons ejected in this fashion are known as photoelectrons. As with any other physical system, conservation of energy must be maintained.

$$h\nu = KE + BE + \Phi_s \qquad (2)$$

In equation (2), hν represents the photon energy, KE represents the kinetic energy of the ejected electron, BE is the ejected electron's binding energy, and Φ_s is the electron spectrometer's work function (a constant, usually ≤ 5 eV). Typically, the electron spectrometer measures the kinetic energy of the photoelectrons which enables the calculation of the corresponding binding energies at a constant photon energy. A XPS spectrum consists of the number of photoelectrons detected in a certain time period versus the binding energy. The XPS spectrum is of great utility in elemental identification because each element has a characteristic set of binding energies for a given electronic transition. However, careful determination of binding energies yields even more information about atomic relationships in the form of bonding configurations. Since in many instances, the photoelectrons are ejected from shared or overlapping orbitals, the bonding environment will have a direct impact on the value of the binding energy for a given electronic transition.

An ultra high vacuum (UHV) environment is required in XPS for a couple of reasons. First, UHV is necessary for the accurate determination of electron kinetic energy by the electron spectrometer by creating a controlled volume where long mean-free-paths between elementary particles exists. In order for accurate electron kinetic energy measurements to be taken, electrons must travel unimpeded from the sample to the entrance slit on the spectrometer. By removing gas molecules from the control volume to UHV levels, the particle mean-free-path in the vacuum system increases to levels where the probability of a photoelectron striking a gas molecule is very low [26]. Secondly, UHV is necessary to prevent further contamination of the material's surface by "atmospheric contaminants", which can include air molecules that collide with the surface of interest according to the kinetic theory of gases [25]. Any molecules that "stick" to the surface of the material being studied due to particle flux are commonly found on XPS spectra because of the surface sensitivity of this technique.

XPS is known as a surface analysis technique. The sampling depth is dictated by the inelastic mean-free-path (IMFP) of the electrons in the material being studied and also the electron energy [27]. Only those electrons that are ejected without energy loss from the material's surface contribute usable electron counts in the spectra. In general, 95% of electrons that are ejected without energy loss reside at a depth three times the IMFP or less from the surface. In actuality, it has been shown that photoionization occurs to depths of several microns in many materials, but any photoelectrons generated at these depths have lost substantial energy by the time they reach the surface and only contribute to the background signal if ejected from the surface [28]. The practical limit for sampling depth in XPS is considered to be 100 angstroms, but the actual value can vary depending on electron take-off angle and the material's IMFP.

Monoenergetic x-rays are used in XPS as excitation photons. Commercially available anodes usually consist of magnesium (Mg) and aluminum (Al) with corresponding Kα photon energies of 1253.6 eV and 1486.6 eV [29]. Mg-Kα radiation, with a wavelength of 9.89 Å, was used in this study. Because of the high energy of these x-rays, photoelectrons are generated from atomic core levels to less energetic transitions encountered from valence shells [28].

Upon insertion of the sample wafers into the UHV system, the samples must be off-gassed and the system pressure brought back down to UHV working levels using a series of UHV pumps prior to spectral analysis. Characterization of the raw metal oxides was conducted on each sample prior to in-situ characterization of SO_2 adsorption for comparison later in the study.

2.4 IN-SITU CHARACTERIZATION OF SO_2 ADSORPTION

XPS is a technique that has found great utility in the study of heterogeneous catalysis [30]. Since most heterogeneous catalytic systems involve surface phenomena, it is easy to see why this is so. However, the utility of XPS is enhanced further when various instrumental appendages are available and used to accomplish very specific tasks. For molecular adsorption studies in heterogeneous catalysis, it is a great advantage to have an environmental cell or reaction chamber attached to the principle analysis vessel that is isolatable from the analysis vessel. A system as described here was used in this study of SO_2 adsorption on the mixed-metal oxides of interest.

This reaction chamber is used as a batch reactor in which gases can be admitted up to a specified upper limiting pressure. The upper pressure limit is an equipment design parameter and must not be exceeded for safety reasons. However, realistic gas pressures for some heterogeneous systems can be achieved. For the materials in question, the actual pressures experienced by an emissions control catalyst are slightly above atmospheric pressure due to modern monolith designs which have very low pressure drops [2]. The reaction cell used in this study can safely accommodate gas pressures of up to 1000 Torr, which enables realistic exposure pressures to be attained experimentally. After some residence time, the gaseous reactants are removed from the reaction cell by a series of isolatable vacuum pumps that evacuate the reaction cell volume. After sufficient evacuation, the sample can then be moved back into the analysis vessel under UHV conditions for XPS analysis. By proceeding in this manner, only chemisorbed species will remain on the solid’s surface and render useful information about the interaction between the solid and gaseous components. Another benefit is the lack of influence provided by atmospheric contamination that would be present from exposing the sample to air while in transit from a reaction vessel into the UHV analysis vessel. Hence, the term “in-situ” describes a protocol where such influences are diminished.

By performing experiments in this manner, an attempt to bridge traditional low-pressure UHV chemisorption experiments with traditional high pressure catalytic studies is undertaken. Interestingly, in this study, a UHV technique such as XPS is employed in a more realistic setting than is normally encountered. In traditional chemisorption studies, the low pressures employed in addition to the highly ordered and nearly defect free surfaces examined explain why differences exist between experiments using this methodology and high pressure catalytic studies [31]. This pressure gap between the two methodologies may signify a generally poor understanding of the relationship between catalytically active sites and the various point defects that may exist on a surface, and particularly on ionic solids such as metal oxides [31].

In addition to pressure gap effects, there are also very specific energy gaps that can limit the applicability of UHV techniques in the treatment of heterogeneous catalysts. Typically, catalysts are used at elevated temperatures or over a range of temperatures. As previously noted for modern automobile emissions catalysts, the temperature can range from ambient temperature upwards to 1273 K [2]. However, in many UHV analyses, researchers have used lower temperatures for chemisorption exposures and analysis. During analysis using several techniques, low temperatures yield an enhanced signal-to-noise ratio. Additionally, when studying adsorption phenomena on heterogeneous catalysts, it is possible to condense multiple monolayers of a gas onto a surface and then allow desorption of this condensate as the temperature is ramped to some temperature that lies above the condensate's boiling point. These two low temperature phenomena can prove beneficial in some applications. However, in this study, an effort is made to reproduce the temperature and pressure conditions that a typical automotive catalyst will experience while garnering the unique viewpoint that only UHV techniques, such as XPS can provide.

2.5 IN-SITU REACTION CELL HEATING SYSTEM

2.5.1 Introduction

In order to accomplish these experiments at realistic conditions, a reaction cell heating system was designed for the existing reaction cell available. Various heating system designs can be found in the literature to serve in various applications [32-40]. In addition, it is common for UHV equipment manufacturers to offer commercial systems that consist of an environmental reaction cell and heating system. However, acquisition cost becomes an issue with these commercial systems and many system designs ultimately are unable to reliably reach the temperatures necessary for catalytic research. Therefore, it is important to have several options to choose from when acquiring or building a suitable system, particularly for use in highly specialized applications [33].

The attainment of temperatures to 1000 K and beyond puts incredible stresses on the materials that are responsible for inducing the heat transfer to the specimen. Damage to a heating filament or some other heating surface is often the result of over-stressing the critical heat generating device. Once damage occurs, it is often necessary to send the system or part of the system back to the manufacturer for repairs. As a result of this drawback, system downtime and extra expenditures are incurred.

It is for these reasons that we have designed and constructed a simple, yet durable, heating and sample transfer system that can be incorporated into most reaction or environmental cells that are attached to and used in conjunction with UHV spectroscopic chambers. Generally, the specimen is to be treated under various conditions in the reaction cell, which is ordinarily maintained at UHV pressure levels to facilitate sample transfer into and out of the cell. Once the specimen has been subjected to some treatment, the reaction cell is re-evacuated and the sample platen inserted into the main spectroscopic chamber for analysis. The system design allows for immediate implementation onto any existing reaction cell with a 6” flange and it is relatively inexpensive. One distinct advantage of this design is that construction and maintenance can be accomplished in the laboratory due to the simplicity of the design and the availability of replacement parts.

2.5.2 UHV System Description

The UHV system in the Surface Science laboratory consists of a Physical Electronics (PHI) Model 1600 main analysis chamber fitted with a PHI Model 10-360 spherical capacitor analyzer (SCA) and multichannel detector. The system is fitted with a PHI Model 10-110 electron gun, PHI Model 04-548 dual anode x-ray source, and a PHI Model 04-303A differential ion gun. These systems, each equipped with an appropriate control system, allow for materials characterization using three important techniques, AES, XPS, and ISS. A PHI Model 07-763 specimen introduction assembly is attached to the main chamber for specimen introduction using a magnetic load lock sample transfer system. Sample platens up to three inches in diameter can be inserted for analysis as long as the platen transfer groove is 0.8975 inches in diameter and 0.1025 inches wide. The sample holder in the main analysis chamber is a PHI Model 10-325 specimen manipulator. This manipulator offers comprehensive manipulation in the x, y, z directions, and also allows tilting and rotation of the sample platen for studies that involve angle resolving techniques. High vacuum pressures are first achieved using a Pfeiffer Model TPU-062 rotary vane and turbomolecular pump, which are attached to the bottom port of the introduction assembly. This turbo-pumping station includes a 62 l/s turbomolecular pump and a rotary vane roughing pump. The introduction chamber has UHV rated valves to both the pump inlet flange and the main chamber flange. UHV pressure levels are ultimately achieved using a 270 l/s PHI ion pump and a titanium sublimation pump system. Pressure measurement in the main analysis chamber is accomplished using a Varian UHV-24 type ionization gauge and, in addition, a Granville-Phillips convectron gauge is attached to the introduction assembly for monitoring pressure levels during sample introduction and off-gassing.

2.5.3 Reaction Cell Design

Figure 2.1 is a diagram of the main analysis chamber with the attached reaction cell. This reaction cell is attached to the main spectroscopic chamber at a joint created by a 2 3/4" CF UHV rated gate valve that permits complete isolation from the main spectroscopic chamber. The system geometry is such that a second magnetic load-lock for sample transfer into the reaction cell creates a forty-five degree angle

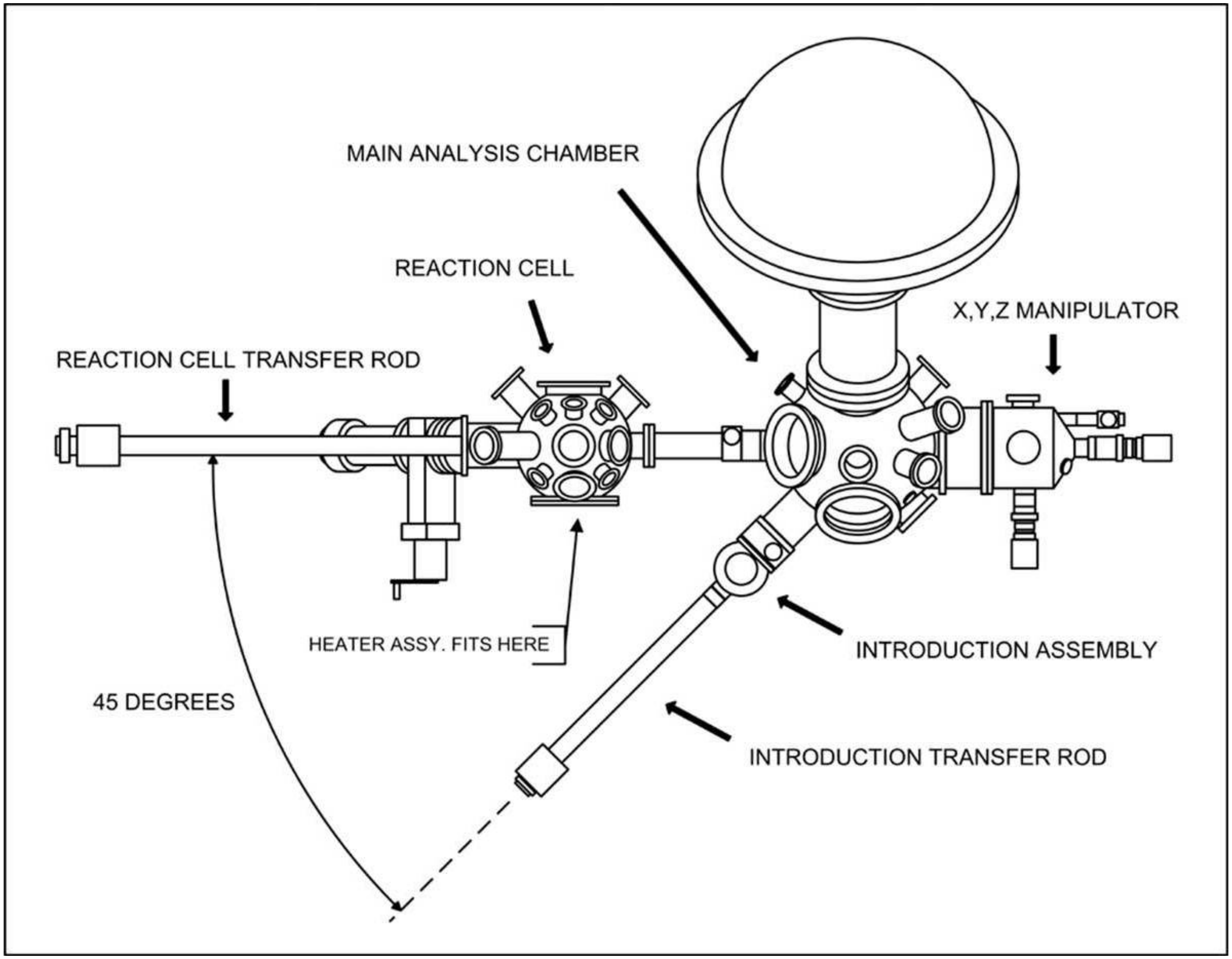

Figure 2.1 Diagram of the UHV system employed in this study

with the introduction assembly load-lock with the center of the main analysis chamber acting as a vertex for the two transfer rods. The connection between the main analysis chamber and the reaction cell allows for the transfer of only one inch sample platens, but this can vary with other systems depending on the diameter of the ports installed between the two chambers. The reaction cell is fitted with roughly fifteen ports for attaching various pieces of equipment and can be modified accordingly. The vacuum pumping system on this isolated cell consists of another equivalent Pfeiffer turbo-pumping station and a Varian VacIon Starcell 55 ion sputter pump (50 l/s). The turbo-pumping station is separated from the reaction cell by a UHV rated manual gate valve. The number of gas reactant lines entering the reaction cell can vary, but in the authors' laboratory, five different gas species are plumbed into the system. The five gas cylinders containing reagent gases are plumbed into a miniature six-way cross equipped with 1 1/3" CF flanges that acts as a manifold for the entering gaseous reactants. The sixth flange is connected to a MDC inline valve (part no. IV-075M). Each gas line is constructed using stainless steel tubing and Swagelok connectors. In addition, Nupro manually actuated valves are used to isolate each line independently before allowing any gas to enter the manifold and passing through the inline valve. Pressure measurement in the reaction cell is accomplished by choosing one of three available gauges depending on the pressure range of the application. A Hastings-Teledyne DV-6 gauge tube, Granville-Phillips convectron gauge, or a Varian UHV-24 ion gauge are all installed in the reaction cell. During most reactive exposures, the tube or convectron gauges are used because these can tolerate higher pressures without causing damage to gauge filaments. Two viewports, one on a 2 3/4 inch flange and another on a 4 inch flange, are installed to provide visual verification and assistance of sample manipulation from two different angles.

2.5.4 Heating System Design

The heating system is mounted to the front of the reaction cell and rests entirely on the 6 inch OD multiport flange hat (MDC 409006). This multiport fitting contains six 1 1/3" CF mini-flanges on a 3.5" bolt circle and a 2 3/4" flange located centrally and with a 3.15" extension from seal to seal. Locating all heating components on this multiport fitting allows for easy access to accomplish any needed repairs. Unbolting the flange hat provides complete access to the heating system. Installed on this fitting are two medium current solid conductor electrical feedthroughs (MDC 640000) using 1 1/3" CF mini-flanges to mount onto the multiport fitting. These two feedthroughs are used to provide the electrical current to the heating element and are rated to handle currents

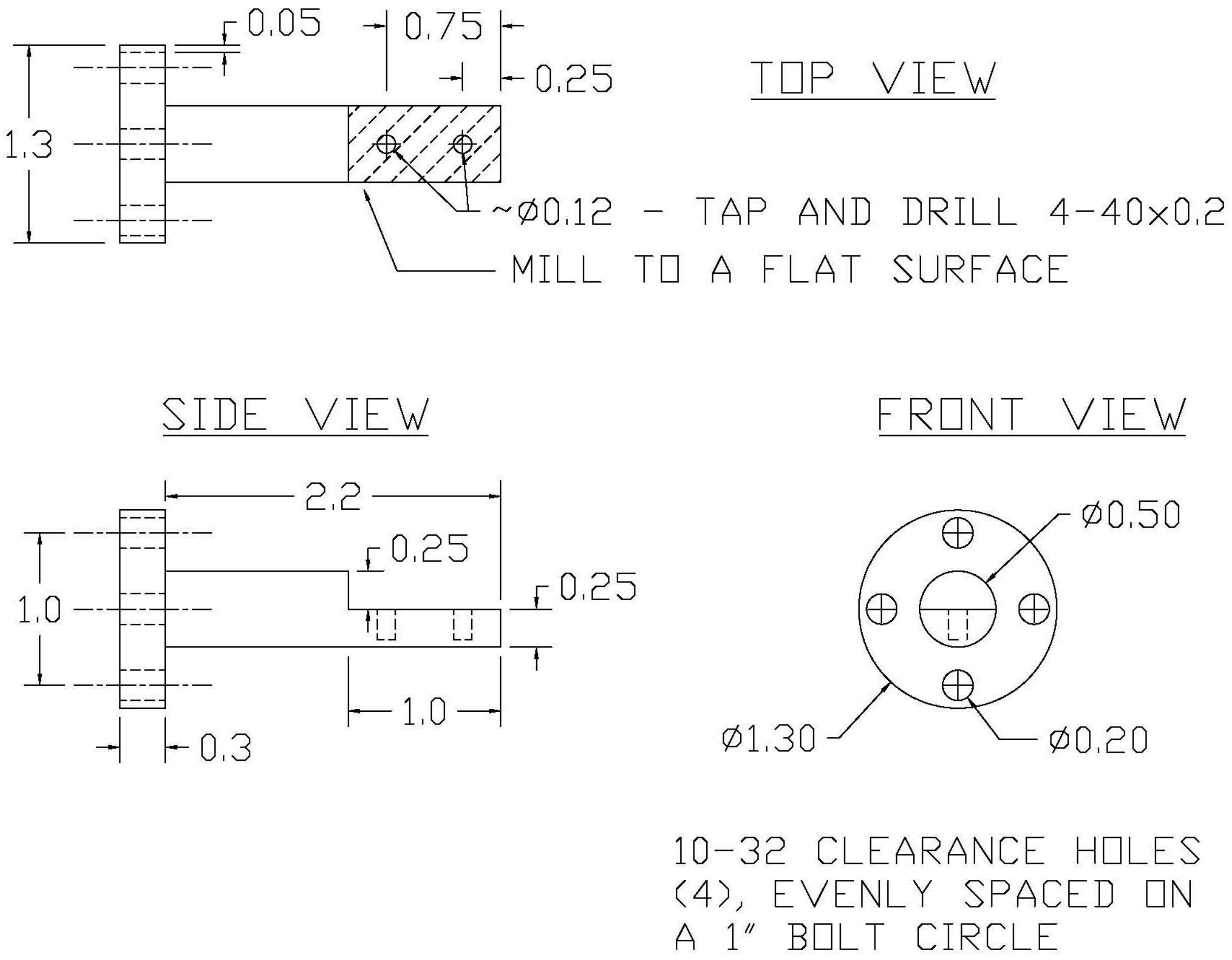

Figure 2.2 Custom-built extension rod dimensions and layout

up to 150 A and 5000 V. In the author's laboratory, a type K thermocouple feedthrough (MPF Products A0391-2-CF) is mounted onto the fitting using a 1 1/3" CF mini-flange for temperature measurement. This thermocouple probe could also be attached to a separate linear motion feedthrough and moved into place to measure pertinent temperatures. A fourth feedthrough attached to the multiport fitting is a linear motion feedthrough mounted to the center 2 3/4" port (MDC 6612018). This feedthrough provides 2 inches of travel which is sufficient for loading the small platens used in the authors' system, but may be insufficient for larger platens in other systems (other longer travel length motion feedthroughs are available). Onto this linear motion feedthrough is attached a custom-machined extension constructed from a 316 stainless steel rod, which is depicted in Figure 2.2. Four 10-32 clearance holes are drilled equidistantly on a 1 inch bolt circle allowing the attachment of the extension directly onto the linear motion feedthrough's 1 1/3 inch diameter attachment head. In addition, the last 1 inch of the extension is milled to a flat surface down to half the diameter of the extension rod, and two 4-40 holes are tapped and drilled onto the flat-milled section. In the authors' laboratory, the extension rod is mounted onto the motion feedthrough using four 10-32 vented screws and is 2 1/2" in overall length. Care must be taken during machining to ensure that the fasteners and associated holes line up properly for any

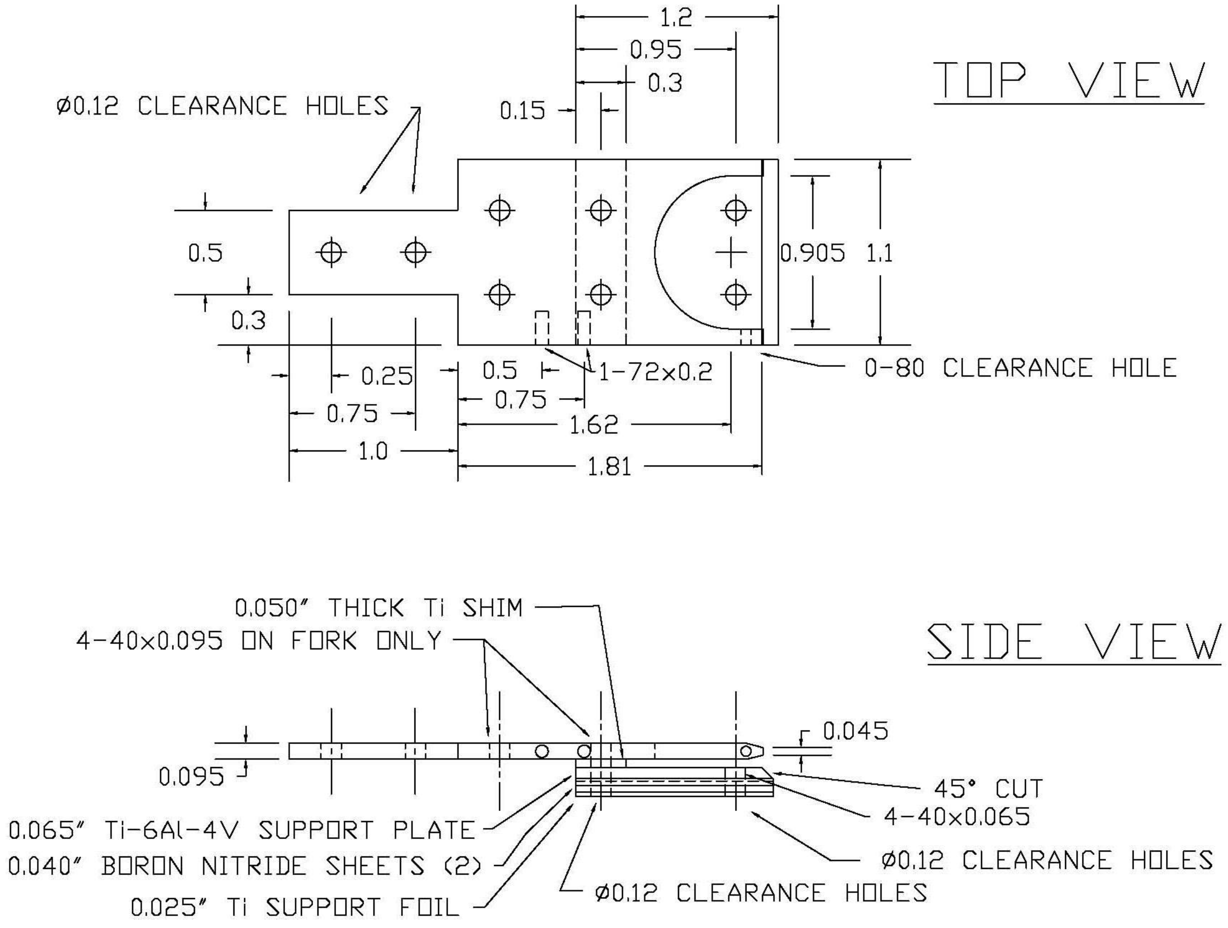

Figure 2.3 Platen fork and heating element arrangement diagram

given system. A sample holder and transfer fork also need to be machined with the proper dimensions to accommodate a 1 inch sample platenas described in Figure 2.3. In the authors' laboratory, this means a fork that is 0.905 inches in ID and 0.095 inches thick (±0.005"). Stainless steel alloy 316 is the material of choice due to its availability and performance at high temperatures. When attaching the transfer fork to the extension arm, two alumina spacers (Kimball Physics Inc. #AL2O3-SP-C-050) are used with each fastener to provide the proper offset for sample holder loading. These spacers are used for fine vertical adjustment, to ensure that the sample transfer fork on the heater has the same vertical position as the load-lock transfer fork that retrieves the sample platen from the main chamber. Small differences may exist in other systems or for other platen designs. In addition, the spacers help reduce the conduction of heat into the extension arm by separating most of the fork attachment area from the extension arm attachment area.

A support plate with a properly sized offset spacer (see Figure 2.3), are constructed of titanium alloy (Ti-6Al-4V). This support plate is to provide the primary heating surface on which the sample platen rests on. Due to the design of the PHI sample platens used in the author's laboratory, it is necessary to include a spacer to allow proper docking of the platen. The actual heat generation comes from a ceramic insulated heating element. Several advanced ceramics may be used, depending on the temperature range that is desired. Aluminum oxide, boron nitride, and commercially trademarked products such as Macor by Corning, Inc., may be used to build the ceramic insulator. The lack of machinability all but eliminates the use of aluminum oxide as the insulator material. Boron nitride (Saint-Gobain Advanced Ceramics Grade AX05) was the ceramic that proved to be the best material for this application. This grade of boron nitride provides the necessary high levels of machinability and resistance to extreme localized temperatures encountered in the proximity of the tantalum heating element. In the proximity of the heating element, it is estimated that temperatures must reach 2000 to 2200 K in order to attain a platen temperature of 1000 K in a reasonable amount of time. In addition, the thermal conductivity for the AX05 boron nitride (71 W/m-K at 298 K) is vastly superior to that of Macor (1.46 W/m-K at 298 K) which offers superior heat transport to the sample platen. A sandwich made of the AX05 boron nitride was constructed from two rectangular pieces, each with four 4-40 clearance holes and one side with a 0.025 inch deep recessed channel for the heating filament as sketched in Figure 2.4. The 25 mil recessed channel can vary in shape, but must run a fairly tight, weaving pattern throughout the ceramic to afford good heat transfer area for the heating filament. In addition, two rectangular recesses are cut on two corners to allow the proper placement of the copper connection tabs. The authors'

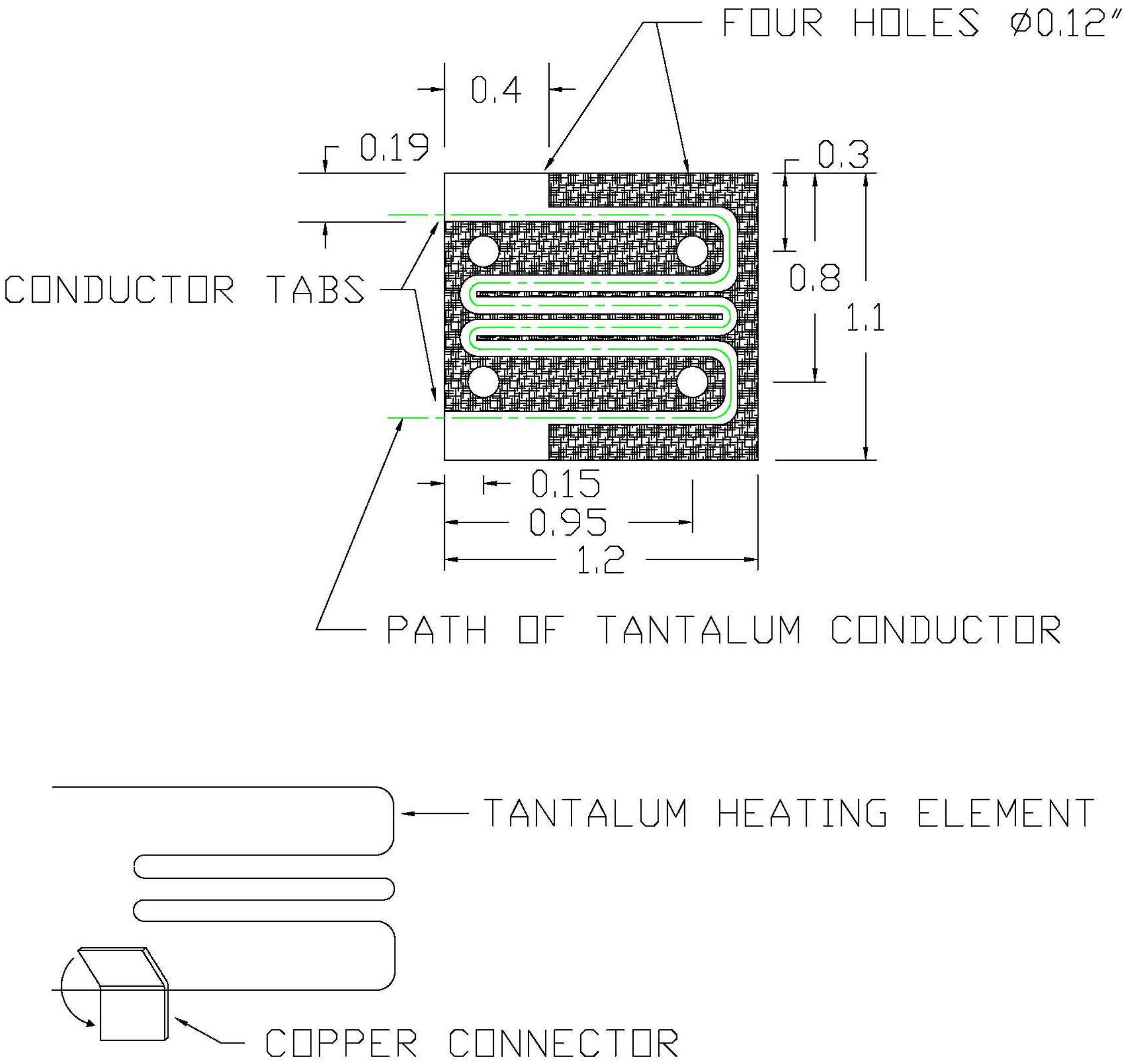

THE COPPER IS SECURED TO THE TANTALUM BY HAMMERING. HOLES ARE THEN DRILLED INTO THE FOLDED COPPER FOR CONNECTION TO A POWER SUPPLY.

Figure 2.4 Channelized boron nitride insulator diagram have found through trial and error that tantalum wire in a thickness of 0.030” is the most ideal heating filament, and it can be shaped fairly easily into the shape of the recessed channel. Tantalum was chosen for this application due to its inherently high melting point, corrosion resistance, workability, and relatively high electrical resistivity. Tantalum wire, 0.030 inches in diameter (Alfa-Aesar No. 43013), was cut to the required length and shaped to fit the contours of the channel that was cut in the boron nitride. Heat transfer by conduction occurs between one layer of ceramic, onto the sample platen support plate, and then into the sample platen. It is for this reason that choosing materials with high thermal conductivity and melting points are of paramount importance. A rectangular backing plate made of a thin section of titanium alloy Ti-6Al-4V is constructed to provide an even distribution of stress imparted by the four fasteners that bring the heating sandwich together.

Several electrical connections need to be made both inside and outside of the vacuum system. Firstly, the tantalum heating filament wire must be attached to small copper tabs to facilitate connection to the power supply. This was accomplished by using a small rectangular section of 25 mil thick copper foil. The copper foil was folded onto itself, with the end of the tantalum filament fully encased in the copper fold. This junction was solidified by carefully hammering the copper until no gap exists between the tantalum and copper. This pressure bonded joint has proven to be an effective method for creating a permanent bond between these two dissimilar metals. Copper was chosen for use as connection tabs because of its ductility and electrical conductivity. Creating an electrical current “bottleneck” with the tantalum wire is important so that the wire becomes the chief heat source without creating heat at some other point in the circuit. Finally, the opposite end of the copper tab was cut to the appropriate length and a hole drilled in it to accommodate a connection screw and washers. Secondly, the power source connections at the feedthroughs were created by using copper-beryllium contacts for 1/4" solid conductors (Ceramaseal #7332-06-A). Inside the vacuum chamber, a flat copper braid (Alpha Wire No. 1233/2) was chosen to carry the heating current due to its low resistivity and predictable travel when linear motion is applied via the linear motion feedthrough. Copper connectors were crimped to the heater end of the flat braid to facilitate connection to the ends of the copper tabs described previously. For the electrical connections outside of the vacuum system, insulated copper braid (6 AWG) was used to provide the current to the heating system. The current source used in the authors’ laboratory was a Hewlett-Packard 6259B direct current power supply, capable of delivering up to 100 A of current and a maximum voltage of 20 V.

For temperature measurement, a chromel-alumel (type K) thermocouple was used in the author's system. Under vacuum, the thermocouple feedthrough (MPF A0391-2-CF) was supplied with screw connectors to which a fine gauge thermocouple probe was attached (Omega #CHAL-015). The probe can be attached to any part of the heating assembly, but ideally will be located at some point close to the sample platen [38]. On the outside of the system, thermocouple wire can be used to display the temperature on any standard type K compatible temperature indicator.

2.5.5 Heater Operation

Specimens were first loaded at atmospheric pressure into the introduction assembly and inserted into the main analysis chamber using the introduction load-lock and transfer rod. Once the platen was inside the spectroscopic chamber, the isolation UHV valve to the introduction assembly was closed and the sample platen can be retrieved using the reaction cell load-lock and transfer rod. The isolation UHV valve leading to the main spectroscopic chamber was closed after the sample platen entered the reaction cell, and the platen can then be transferred from the load-lock transfer rod/fork to the heating system transfer fork. Once this transfer was made, the heating system is ready for use. The electrical requirement varied depending on the ultimate desired temperature. Temperatures of 1013 K have been obtained in the author's laboratory using a current of 20 A at 6.25 V in approximately 19 minutes. Figure 2.5 is a heating curve generated while operating under these settings. Normally, reactant exposures were begun after reaching the temperature of interest and allowing several minutes for temperature equilibration. Once the treatment was completed, the reaction cell is evacuated and the power supply was turned off to allow the platen to cool back to room temperature. The platen can then be moved back onto the reaction cell load lock transfer rod and back into the spectroscopic chamber when the appropriate vacuum level is achieved in the reaction cell.

2.6 EXPERIMENTAL CONDITIONS

A variety of experimental conditions were used in this study to enhance the overall understanding of SO_2 adsorption on this family of metal oxide materials. Ceria and zirconia solid solutions were prepared in accordance with the co-precipitation technique described in section 2.1. The compositions used in this study included samples with ceria:zirconia molar ratios of 1:0, 9:1, 7:3, 5:5, 2:8, and 0:1.

With the design and construction of a reliable heating system, several temperatures were incorporated into the experimental protocol.

For all six compositions, exposures were conducted at temperatures of 298, 473, and 673 K. These temperatures represent conditions that fall within the realistic operating temperature range for automobile catalytic converters [2].

The gas pressure employed in this study was 1000 torr (T), and the simulated exhaust gas was a 20 ppm SO_2 and nitrogen gas mixture. The 20 ppm SO_2 level is perhaps a slightly higher exhaust SO_2 level than is currently being experienced in many parts of the United States due to new regulations. However, since the exposure time is only 15 minutes, this protocol can be thought of as a short-term accelerated test. The 1000 T total pressure corresponds to a SO_2 partial pressure of 0.02 T.

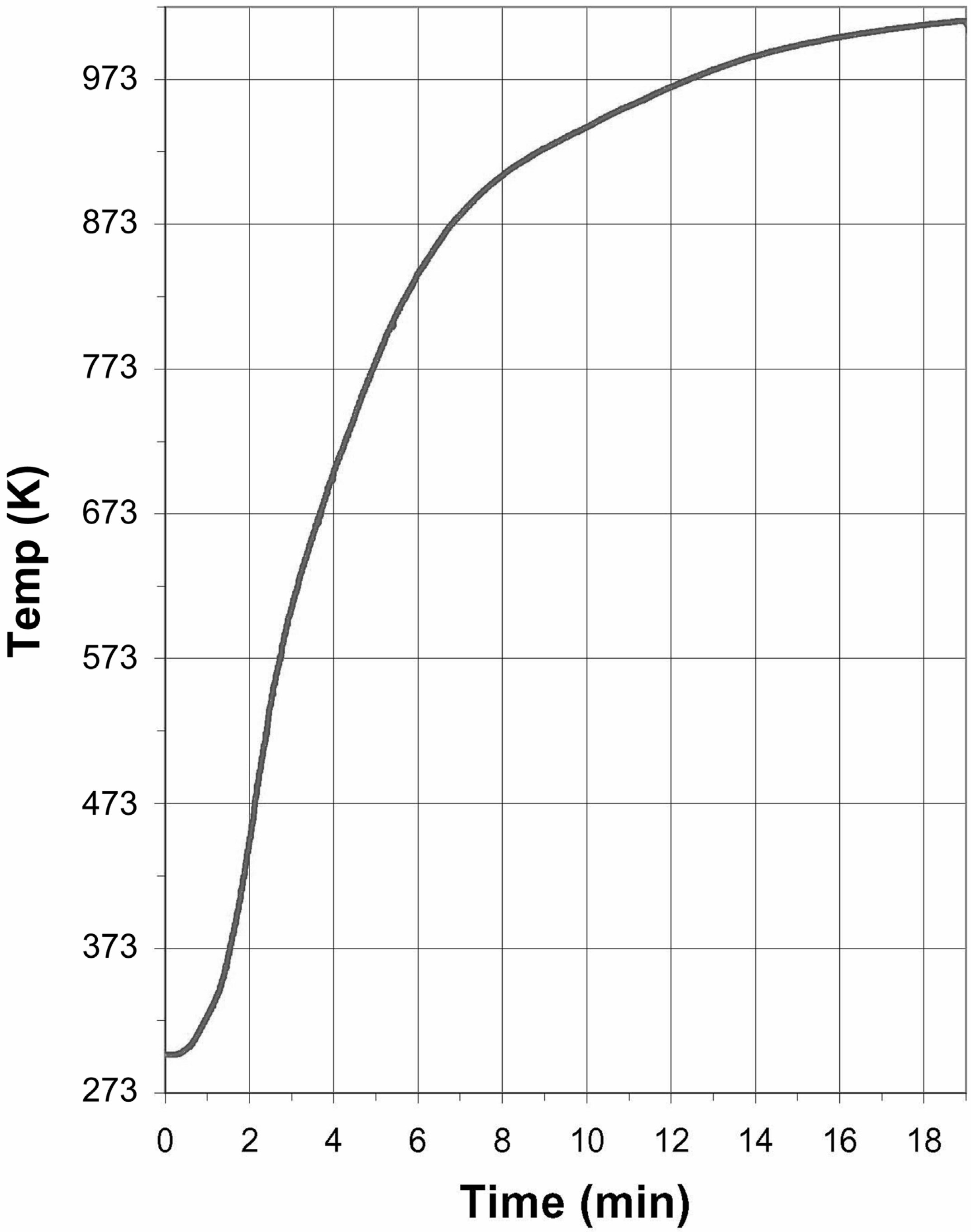

Figure 2.5 Heating system performance graph

CHAPTER III

SO_2 ADSORPTION ON CSZ MIXED-METAL OXIDES

3.1 APPARATUS PARAMETERS

A Physical Electronics Model 1600 Multitechnique UHV system was employed in this study (base pressure of 5×10^{-10} torr), which is capable of AES, ISS, and XPS analyses. The electron energy analyzer is a multichannel spherical capacitance analyzer (SCA) operated with a 23.5 eV pass energy. The X-ray source is a dual-anode source capable of delivering achromatic Mg Kα and Al Kα X-rays. During all experiments, spectra were obtained using Mg Kα X-rays at 15 kV and 300 watts, under vacuum maintained at or below 5×10^{-9} torr (T). The energy resolution of the SCA is 1.07 eV, which was determined by finding the full-width at half maximum (FWHM) of the $4f_{7/2}$ gold core electron line as obtained using a suitable gold calibration foil.

In addition to the main UHV analysis chamber, a custom-modified and isolatable UHV chamber was attached to the system as a stand-alone reaction cell as described in sections 2.4 and 2.5. This reaction cell allowed in-situ heating, sample translation to and from the main analysis chamber, and exposure to reactant gases at pressures reaching

1000 T. The reaction cell had dedicated rotary vane, turbomolecular, and triode ion sputter pumps to maintain UHV conditions inside the cell.

The photoemission spectral data were acquired using PHI Surface Analysis Software. Spectra were charge compensated to the adventitious Carbon 1s line at 284.8 eV as described in the literature [41]. Data analysis and curve deconvolution was accomplished using XPS International Spectral Data Processor software v. 4.1.

3.2. DATA ACQUISITION

The characterization of SO_2 interactions with the mixed metal oxides was performed in a systematic manner. The unexposed wafers were first analyzed using XPS to check for contamination and to obtain baseline information on all ceria and zirconia features prior to exposure to SO_2. Immediately following spectrum acquisition, the sample was moved under UHV conditions to an in-situ reaction cell. The vacuum pumps on the reaction cell were then isolated from the cell and a 20 ppm SO_2 and N_2 gas mixture was admitted into the cell until the desired pressure was reached. Reaction cell pressure was monitored simultaneously using a Phillips-Granville convectron-tube pressure gauge and a Hastings vacuum gauge. Once the desired gas pressure was attained in the reaction cell, the heating cycle was started. Approximately 15 minutes were required for the sample to reach the desired reaction temperature. Once the desired exposure time of 15 minutes had elapsed, the reaction cell was carefully evacuated and the sample allowed to cool to below 333 K. In accordance with general UHV operating guidelines, a satisfactory vacuum for reintroduction into the analysis chamber (9 x 10^{-8} T) must be attained before translation back into the analysis chamber. The evacuation, cooling, and reintroduction process lasted no longer than 1 hour. Photoemission spectra were collected as soon as feasibly possible after reintroduction.

3.3 SAMPLE TEMPERATURE AND COMPOSITION EFFECTS

The photoemission spectra collected during the adsorption of SO_2 onto the surfaces of six different compositions of CZMMO materials were examined. Previous studies using similar types of instrumentation have shown that the sulfur 2p signal amplitude is dependent on the treatment pressure [42]. For this reason, a treatment pressure of 1000 T was chosen for this study because this pressure is closer to the actual pressure a catalyst will experience in a typical catalytic converter. Figure 3.1 shows the high resolution spectra obtained for the sulfur 2p region at an exposure temperature of 473 K as a function of MMO composition. In this figure, the feature labeled A is attributed to the sulfur 2p photoemission. The triple lobed feature in this figure, with individual peaks labeled B, C, and D, are attributed to zirconia 3d satellite features

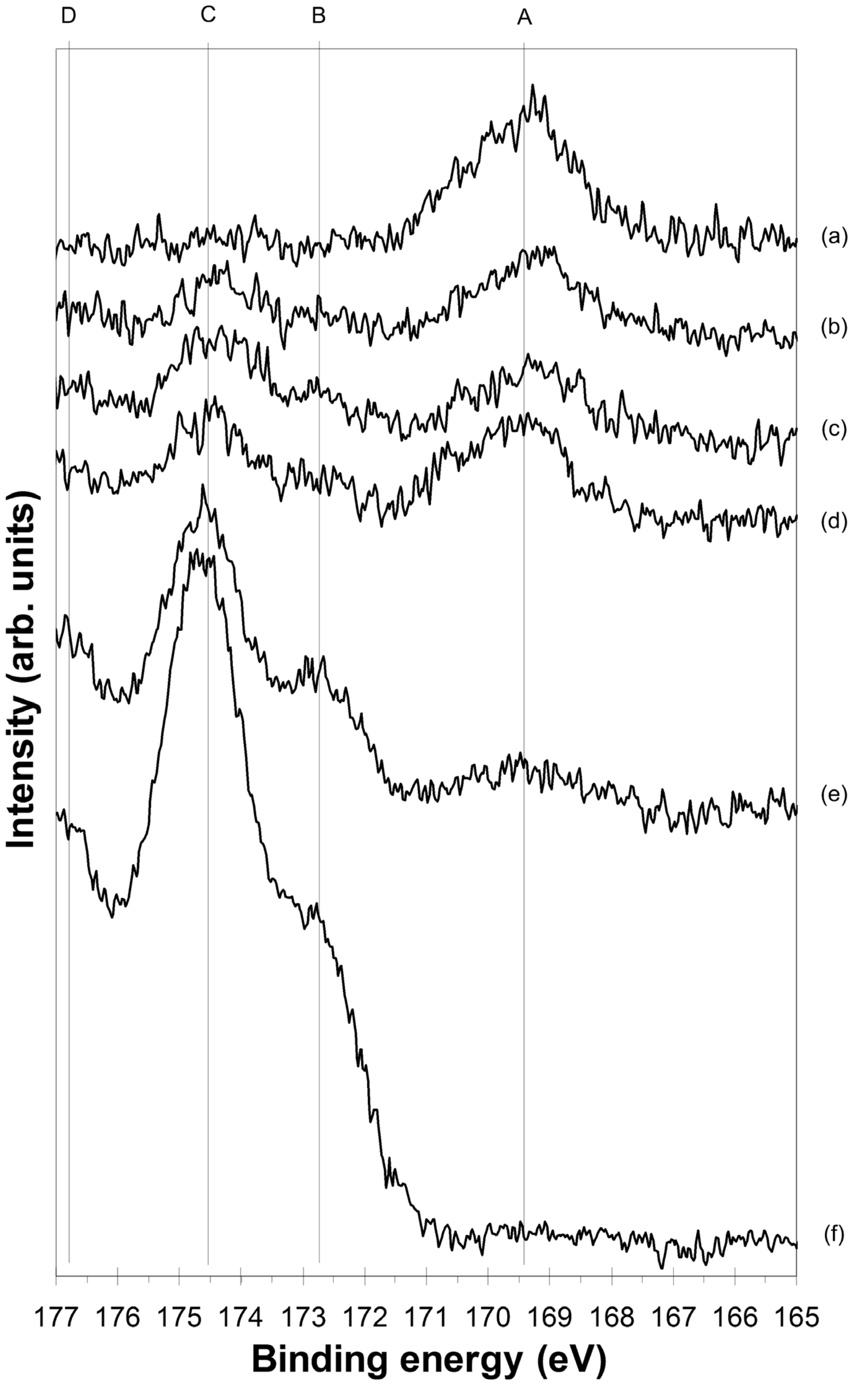

Figure 3.1 High resolution XPS spectra taken after SO_2 exposure at 473 K for six compositions, (a) Ce/Zr=1:0, (b) Ce/Zr= 9:1, (c) Ce/Zr= 7:3, (d) Ce/Zr= 5:5, (e) Ce/Zr= 2:8, (f) Ce/Zr= 0:1

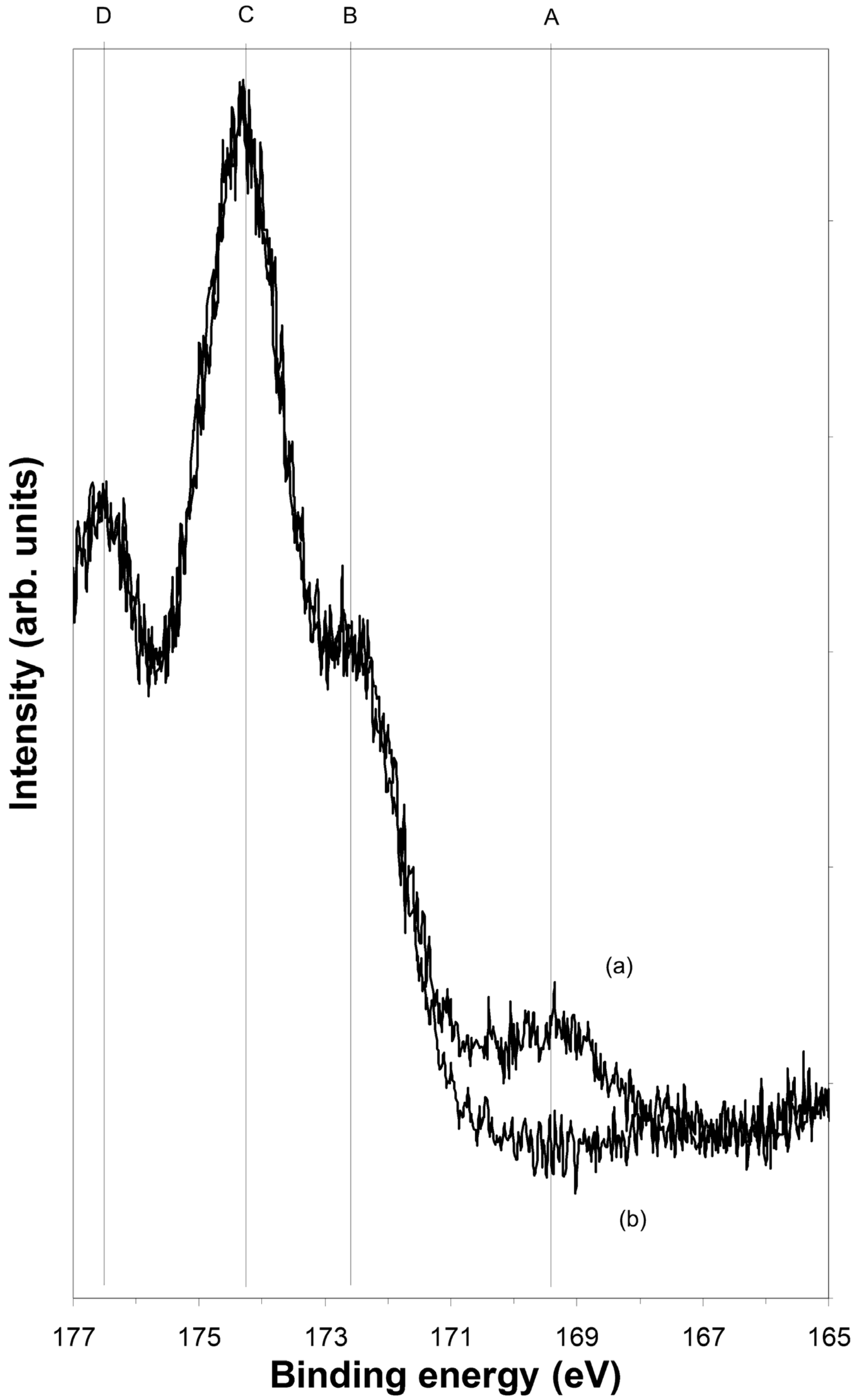

Figure 3.2 High resolution XPS spectra for ZrO_2 before (b) and after (a) exposure to SO_2 at 673 K showing the three lobed zirconia 3d satellite feature encountered in this energy range

and have been verified by observing unexposed spectra of the same energy segment for various MMO compositions. Figure 3.2 shows the 100 mol % zirconia satellite features for the (b) raw zirconia and (a) zirconia after exposure to the SO_2/N_2 gas mixture at 673 K. Figure 3.1(a) shows the S(2p) feature observed for the 100 mol% ceria composition at an approximate binding energy of 169.3 eV. This binding energy is in the binding energy range normally associated with sulfur compounds [25]. This feature is approximately 4 eV wide which demonstrates that it is composed of multiple oxidation states of sulfur. The S(2p) feature is also observed in Figure 3.1 for the other compositions examined. In Figure 3.1, the spectra are labeled (a) to (f) in order of increasing zirconia molar ratio. Therefore, spectra (a) corresponds to pure ceria and (f) corresponds to pure zirconia in the set of compositions that were examined. Interestingly, as the mole fraction of ceria was increased, the S(2p) normalized area also increased. Similarly, Figure 3.3 represents the same experiments run at 673 K. Here, it should be noted that elevated temperatures increase the amount of SO_2 adsorption onto all compositions of CZMMO materials that were examined. In particular, the small S(2p) feature present in Figure 3.3(f) shows that zirconia adsorbed some SO_2 at more elevated temperatures, whereas at 473 K, as in Figure 3.1(f), the zirconia showed negligible interaction with SO_2. The SO_2 adsorption on zirconia at elevated temperature can be further

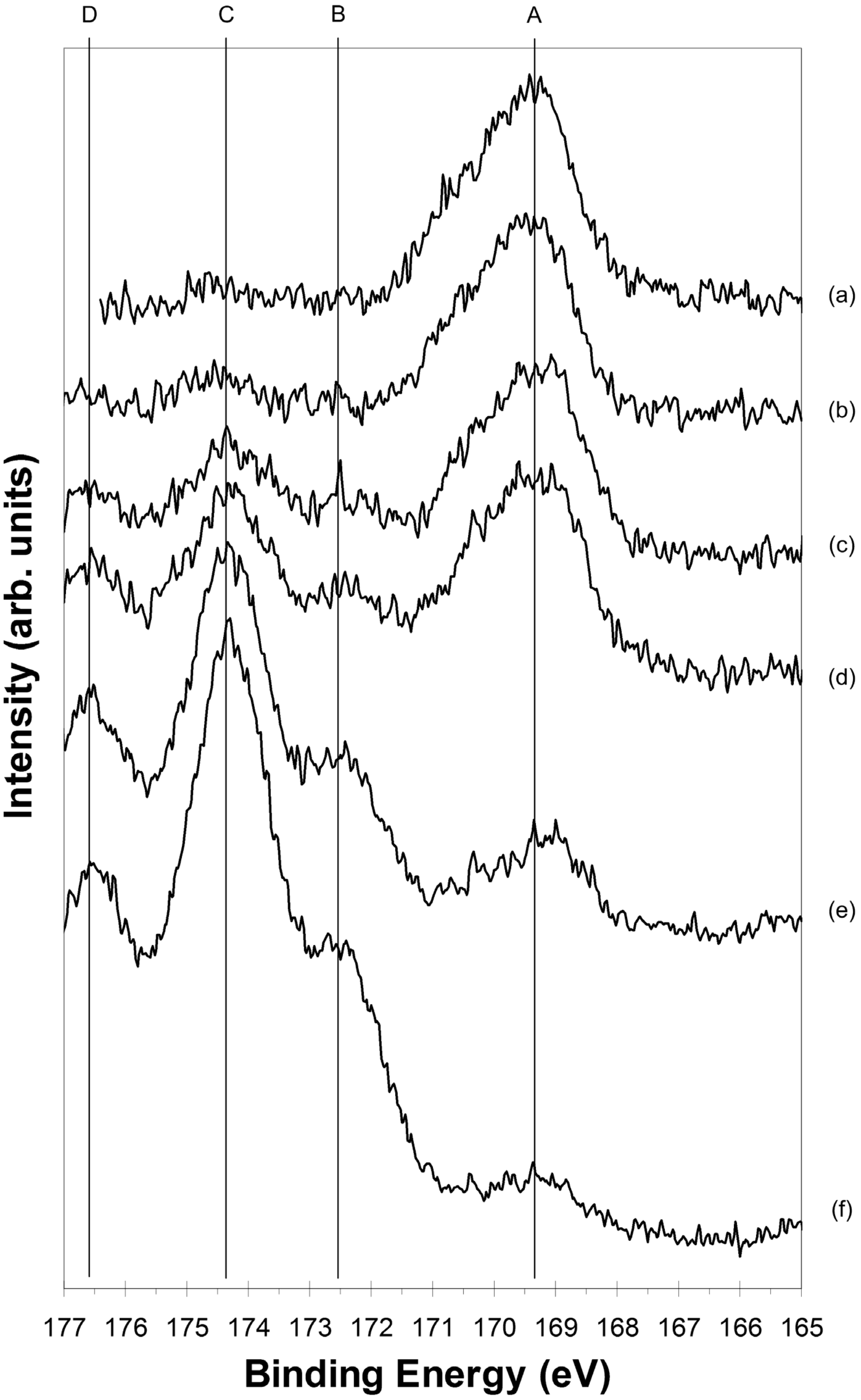

Figure 3.3 XPS spectra after SO_2 exposure at 673 K for six compositions, (a) Ce/Zr=1:0, (b) Ce/Zr= 9:1, (c) Ce/Zr= 7:3, (d) Ce/Zr= 5:5, (e) Ce/Zr= 2:8, (f) Ce/Zr= 0:1

visualized in Figure 3.2. This is a composite of two spectra collected for pure zirconia at 673 K after exposure (Fig. 3.2(a)) and before exposure to SO_2 (Fig. 3.2(b)). The maximum S(2p) intensity occurs with the 100 mol% ceria composition at both 473 and 673 K. In all cases, the S(2p) peak position does not vary. Figure 3.4 is a summary of the temperature and compositional dependencies displayed by the S(2p) signal in the acquired data sets. The dependence on temperature seems to affect more strongly the amplitude of the sulfur 2p signal than does composition.

3.4 SULFUR LINE ANALYSIS

For some of the experiments, a well defined S(2p) feature could be analyzed for chemical shift effects. After S(2p) curve deconvolution as in Figure 3.5 for 100 mol% ceria at 673 K, the presence of two distinct surface sulfur-bearing species can be discerned due to the appearance of a pair of doublets. The deconvolution of the S(2p) feature takes into account the known 2:1 intensity ratio between the $S(2p_{1/2})$ and $S(2p_{3/2})$ spin-orbit states, the known binding energy Δ(BE) between these spin-orbit states of 1.18 eV, and constant instrument electron energy resolution of 1.1 eV (FWHM). The doublet occurring at higher binding energies is assigned to the formation of surface SO_4 species while the doublet at lower binding energies is assigned to the formation of surface

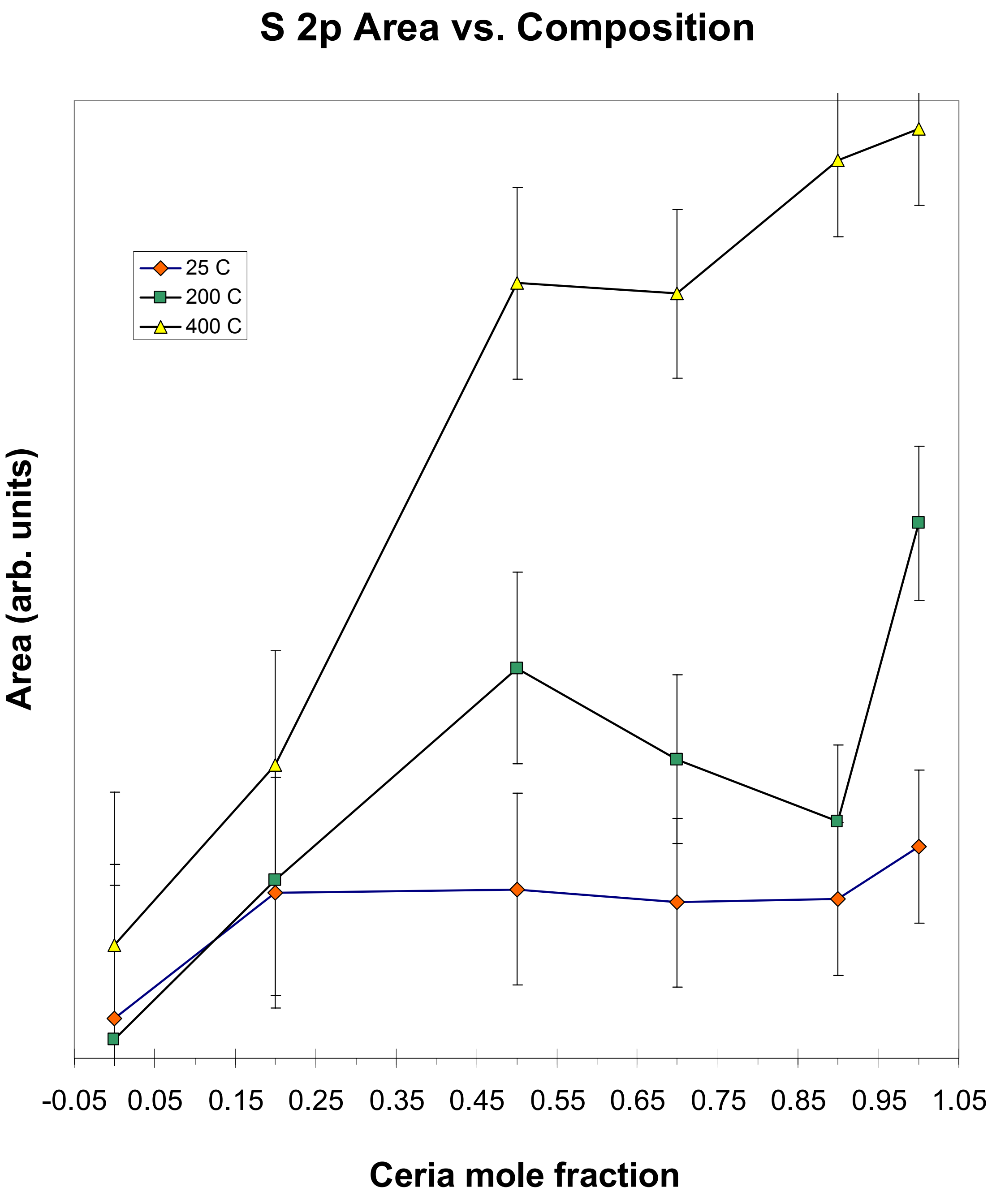

Figure 3.4 Plot of S(2p) normalized peak area vs. ceria (or zirconia) molar ratio for exposures to SO_2 at 298, 473, and 673 K

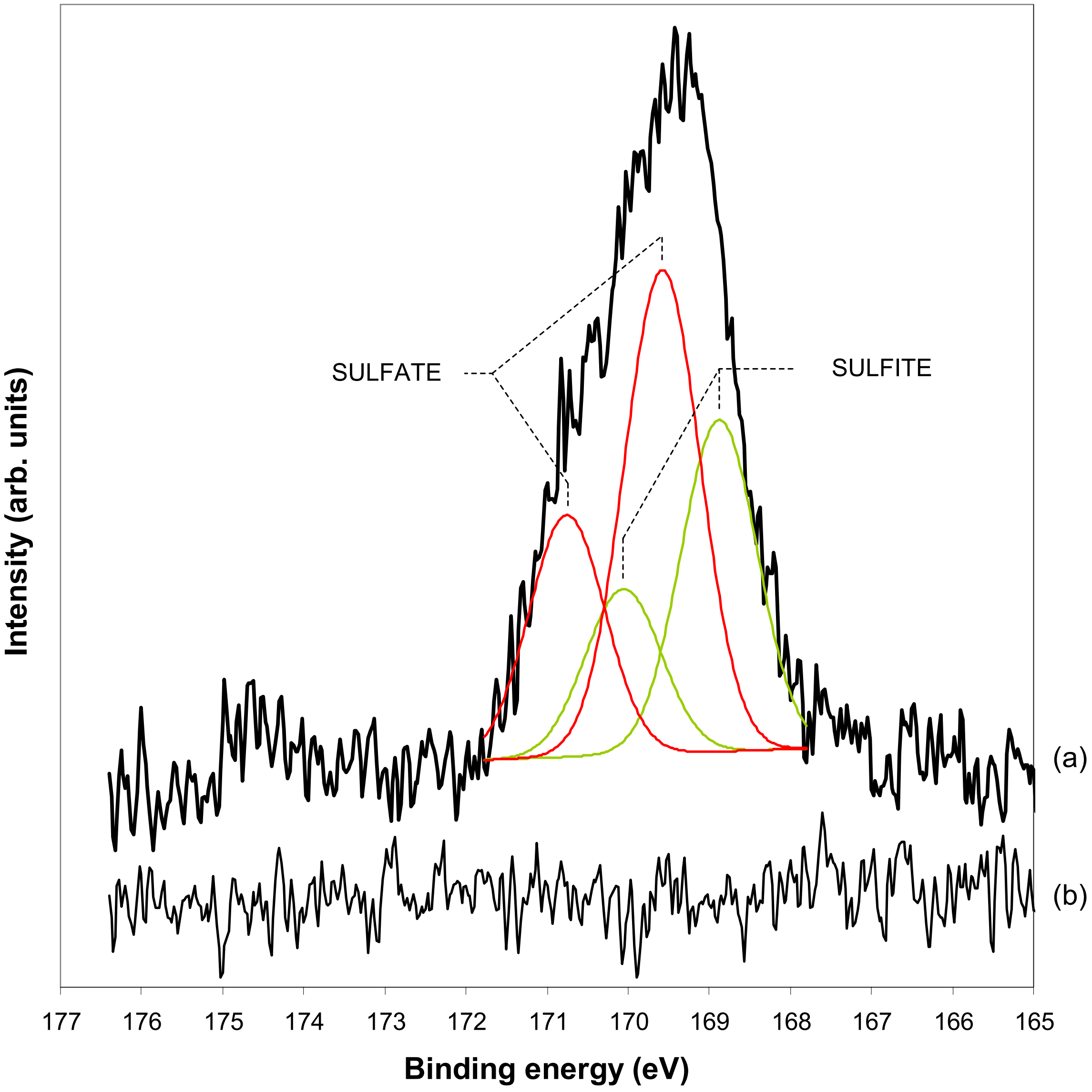

Figure 3.5 S(2p) curve deconvolution for pure ceria exposed to SO_2 at 673 K

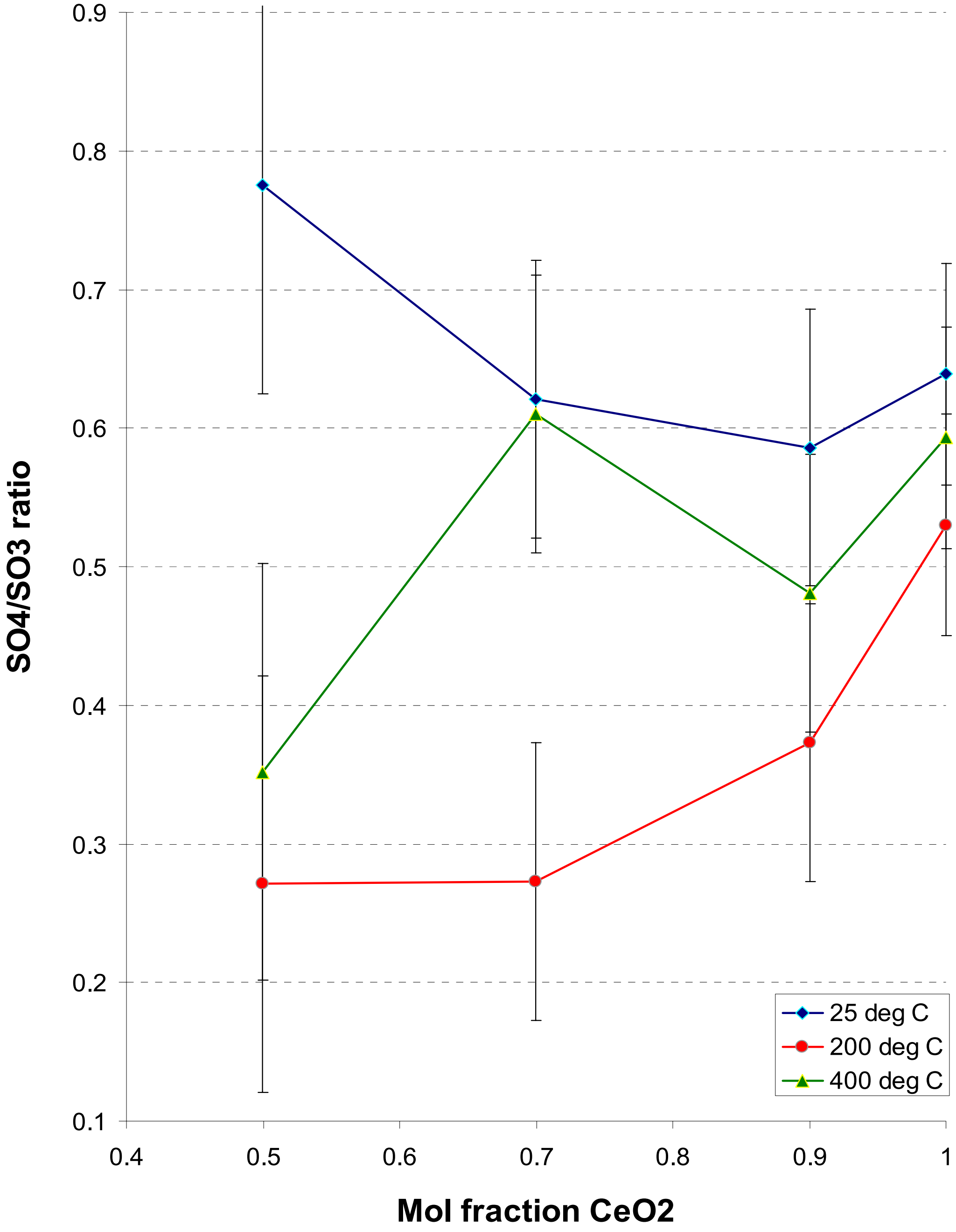

Figure 3.6 Plot of sulfate-to-sulfite area ratio vs. ceria mole fraction for exposures to SO_2 at temperatures of 298, 473, and 673 K

SO_3 species. This shows similarities with the results found by other researchers who have performed studies focused on ceria [43-46].

Theoretically, a quantitative ratio between the SO_4 and SO_3 contributions could be made for all the samples tested. Figure 3.6 is an attempt to do so, but it is not possible to draw any conclusions from this graph other than that there is no trend visible for this ratio. This is in part due to the low S(2p) signal intensity for those compositions whose molar ratio is high in zirconia. Sulfur 2p line deconvolution was not attempted for the 100% zirconia samples due to the small signal generated as shown in Figure 3.2. The 2:8 CeO_2/ZrO_2 spectra were also difficult to process in this manner due to the low signal to noise ratio and small signal amplitude, giving high uncertainties.

3.5 DISCUSSION

3.5.1 Sulfate and Sulfite Surface Species Identification

The characterization of the surface species formed during the interaction of SO_2 and ceria-zirconia mixed-metal oxides is important for the designers of catalytic systems who want to produce catalysts that are tolerant to SO_2 exposure. Table 3.1 shows the various photoemission peak assignments in the literature for SO_2 on ceria. A study by Overbury *et al.* concluded that SO_2 adsorbs on anionic sites on ceria to yield a sulfite (SO_3^{2-}) complex and that there is no evidence for the formation of

Table 3.1 Reported literature values for binding energies and species identified during photoemission experiments conducted for SO_2 adsorption on ceria

	SURFACE SPECIES	B.E. S $2p_{3/2}$	MATERIAL ANALYZED
D. Beck, GM Research Labs	SO_3 SO_4	167.5 eV 169.1 eV	Commercial TWC and monolith
S.H. Overbury, Oak Ridge NL	SO_3^{2-} SO_4	168.4 eV 171 eV	CeO_2(111)/(110) on Ru (thin film)
J. Rodriguez, Brookhaven NL	SO_2 SO_3 SO_4	166 eV 167 eV 168-169 eV	Polycrystalline CeO_2 on Pt(111) (thin film)
Gorte and Vohs, Univ. of Pennsylvania	S^{2-} $SO_2/(SO_3)^{2-}$ SO_4^{2-}	160 eV 166 eV 167.5 eV	Polycrystalline CeO_2 on Mo(100) (thin film)

a sulfate species [43]. Waqif *et al.* have shown in one FTIR study that SO_2 adsorption can occur on a variety of sites found on metal oxides. In particular, basic O^{2-} and hydroxyl groups have been shown to interact with SO_2 to form sulfite species on several different oxide materials [47]. The same study shows the formation of sulfate species upon exposure of the oxide to SO_2 at elevated temperatures [47]. In another FTIR study, Waqif *et al.* show that surface sulfate species which form on ceria are thermally stable up to 973 K after evacuation [48]. In contrast to the study by Waqif *et al.*, Rodriguez *et al.* has shown using X-ray absorption near-edge spectroscopy (XANES) that sulfates can form on ceria at temperatures as low as 300 K and that the sulfate decomposes at temperatures reaching 700 K by primarily desorbing SO_2 and small amounts of SO_3 while a substantial fraction of the sulfate oxygen remains in the ceria matrix [45]. Yet another study of SO_2 interaction with ceria by Ferrizz *et al.* supports the work by Waqif *et al.* that the formation of surface sulfates is a thermally activated process [46]. However, the SO_2 adsorbed at 298 K forms primarily sulfite species, but a much smaller fraction forms sulfate species at this temperature [46]. While there is some variation in surface species formation in the literature, it is clear that generally sulfate and sulfite species are formed from the interaction of SO_2 with ceria.

This study focuses on the characterization of the surface sulfur species that form on ceria-zirconia mixed-metal oxides upon exposure of the MMO materials to a mixture of SO_2 and N_2 at elevated temperatures and pressures. The surface sulfur species that form upon exposure to a SO_2 and N_2 gas mixture are inevitably forming by the adsorption of SO_2 onto anionic lattice oxygen centers or surface hydroxyl groups that may be present on the oxide's surface. Elemental sulfur has a binding energy in the range of 166 eV [25]. As the sulfur atom's oxidation state increases and bonding with oxygen occurs, the sulfur 2p binding energy will increase from the elemental sulfur binding energy value [25]. As the oxidation state of sulfur increases, each sulfur atom will have additional oxygen atoms bonded to it, which yields an incremental increase in the S(2p) binding energies. Physisorbed SO_2 binding energies on ceria have been examined by Rodriguez *et al.* in the literature, and have reported $S(2p_{3/2})$ binding energies in the range of 167-168 eV [45]. However, sulfur dioxide, having a sulfur oxidation state of +4 should presumably have a binding energy that is lower than that of a sulfur molecule in which the sulfur atom is bound to additional oxygen atoms or is present in a +6 oxidation state. Two sulfur species, a sulfate and a sulfite, have been identified in this work and possess $S(2p_{3/2})$ binding energies of approximately 169.6 and 168.9 eV. These values are fairly consistent with other reported values. These results suggest that the sulfur atoms are present in a +4 and +6 oxidation state on these materials in the form of sulfate and sulfite species.

3.5.2 Effect of Temperature on SO_2 Adsorption

The SO_2 adsorption sites can consist of terminal lattice oxygen atoms or surface hydroxyl groups for the formation of sulfite and sulfate surface species. The apparent increase in the amount of SO_2 adsorbed at higher temperatures indicates an increase in the surface energy of the oxide, allowing the SO_2 to react more completely with the available surface features in the allotted amount of time. Rodriguez *et al.* report that the population of oxygen vacancies in bulk ceria favors the formation of sulfite species at the expense of sulfate species [45]. In the same body of work by Rodriguez *et al.*, the authors propose that heating the ceria thin films to 673 K removes any residual hydroxyl groups from the surface [45]. However, the authors do not provide any evidence which demonstrates the existence of or the removal of the hydroxyl functional groups that may or may not be present. In another work by Badri *et al.,* surface hydroxyl groups on ceria are characterized using FTIR techniques [49]. These researchers have found that hydroxyl groups on ceria can be singly, doubly, or triply coordinated [49]. Interestingly, the doubly bridged hydroxyl groups show thermal stability at 573 K, the highest temperature used in that study [49]. In addition, Badri *et al.* showed that the ceria which was calcined at 673 K contained anionic oxygen vacancies adjacent to doubly bridged hydroxyl groups after outgassing at temperatures above 473 K [49]. This is in stark contrast with respect to the ceria subjected to calcination and subsequent sintering at 1123 K, in which no evidence is found for the existence of oxygen vacancies at any outgassing temperature [49].

In effect, the spectral data show that hydroxyl groups or lattice oxygen atoms cannot be ruled out as key components in the formation of sulfite and sulfate surface species under the conditions of this study.

CHAPTER IV

CZMMO OXYGEN PHOTOEMISSION

4.1 OXYGEN 1s HIGH RESOLUTION PHOTOEMISSION SPECTRA

In the previous chapter and references cited therein, oxygen has been shown to play an important role in the adsorption of SO_2 on many metal oxides. From the completed experimental work on the base mixed-metal oxides, it is evident that sulfur dioxide interacts with lattice oxygen atoms or possibly with the oxide's metal centers with subsequent transfer of oxygen from the nearby lattice to the newly formed surface sulfur complex to form oxygen-rich sulfite and sulfate surface species. Therefore, due to the great importance of key oxygen intermediates in catalysis by ceria, it is important to monitor changes in the fine structure of the oxygen 1s photoemission under the conditions of this study [51].

X-ray photoelectron spectroscopy (XPS) has been shown to be a valuable tool in distinguishing the various forms of oxygen found in a variety of solid materials [25,30,31,52,53]. In general, the binding energy for the O(1s) photoemission lies in the 528 to 534 eV range [25]. Most metal oxides have O(1s) binding energies from 528 to 531 eV [25].

Another unique capability of XPS is the ability to determine the presence of surface-terminating hydroxyl groups on metal oxide surfaces [25]. These hydroxyl-terminated surfaces often act as Bronsted acids, or proton donors, and hence are very important in the study of modern heterogeneous catalysis [2,30]. The presence of terminal hydroxyl groups on solids is the subject of many research efforts in solid acid catalysis [54-56]. However, the focus of this study is not to quantify the acid/base properties of the materials themselves, but to further disseminate the role which these acidic sites play in the adsorption of sulfur dioxide on ceria-zirconia model catalytic systems.

Many techniques, such as FTIR, MASNMR, XPS, and wet chemical techniques, are available to determine and quantify the concentration of hydroxyl groups present in solid materials [55-56]. More specifically, many studies have addressed this issue for some of the materials of interest in this investigation, such as cerium oxide [49,57-63]. However, XPS offers a unique viewpoint due to the high degree of surface sensitivity, which in general is much more surface sensitive than the other techniques listed [25]. The theory behind XPS as an analytical technique was presented in Chapter 2.

4.2 TERMINAL HYDROXYL GROUPS ON METAL OXIDES

In general, the origin of hydroxyl groups on metal oxides occurs from differences in starting materials and calcination treatments. Alumina is by far the most common metal oxide and also displays some degree of surface hydroxyl functionalization [2]. During synthesis, various crystalline alumina hydrates are precipitated in aqueous basic or acidic solutions [2]. The resulting boehmite or bayerite crystals are then calcined to produce crystalline alumina. The final crystal structure is determined by the calcination procedure and ultimate temperature [2]. However, calcination temperatures above 1423 K result in the complete loss of surface hydroxyl functionalization and a minimization of physical surface area in the alumina due to sintering [2].

Synthesis procedures for other metal oxides which rely on aqueous precipitation techniques, such as the one employed in this study for ceria and zirconia, are responsible for the inclusion of a certain amount of hydroxyl functionality on these materials. Ceria has been shown to sinter at 1073 K, posing problems for the modern automotive emissions catalyst because of higher exhaust operating temperatures [2,15]. Higher operating temperatures are the result of initiatives to increase fuel economy while also increasing the average speed driven on roadways [2]. Close-coupling of the catalytic converter, devised to shorten the time required from a cold engine start to catalyst light-off, also results in higher ultimate catalyst operating temperatures [64]. Depending on these factors, driving conditions, and engine operating parameters, the modern emissions catalyst can be exposed to, and must withstand temperatures reaching 1323 K [2].

For these reasons, thermal stabilizing agents, such as zirconia have been used in conjunction with the critical OSC component, ceria, in solid solutions for incorporation in modern emissions control catalysts [2,15]. In this investigation, calcination conditions were 773 K for one hour under an air atmosphere in a laboratory furnace. This calcination temperature is well below the sintering temperature for both ceria and zirconia. Additionally, since the synthesis protocol used aqueous salt solutions and ammonium hydroxide for precipitation, it is likely that some residual hydroxy groups would remain in the calcined metal oxide powders. This provides additional justification for a closer look at the O(1s) photoemission of the materials used in this study.

From a practical point of view, the formation of hydroxyl groups on a commercial catalytic converter is a subject of great relevance. In a internal combustion engine, complete oxidation of hydrocarbon fuel yields water and carbon dioxide as the two principle exhaust components [2,6]. The constant presence of water in the exhaust stream would make the formation and replenishment of hydroxyl groups on the catalyst a real possibility.

4.3 PREVIOUS XPS INVESTIGATIONS ON CERIA

In previous studies it has been shown that hydroxyl groups do indeed form on cerium or cerium oxide from exposure to water vapor, and that these hydroxyl groups can be detected using XPS [58,62]. However, it should be noted that elementally, XPS cannot detect hydrogen. So the determination of the presence of surface hydroxyl groups using XPS will depend solely on the fine structure of the O(1s) photoemission. Mullins *et al.* reported that the O(1s) binding energy for surface hydroxyl groups on argon ion sputtered ceria (001) and (110) thin films was 533.5 eV [58]. Koel *et al.* reported the same O(1s) feature, except formed from the interaction between cerium metal and water, at a binding energy of 532.7 eV [62]. The difference in the reported binding energies from these two groups may be attributed to differences in spectrometer calibration or method of static charge correction. Nevertheless, these two groups of investigators have an excellent agreement for the reported binding energy difference of 3.1 eV between the hydroxyl O(1s) binding energy and the lattice oxygen binding energy for the Ce(IV) oxide [58,62]. The binding energy difference between the hydroxyl O(1s) and Ce(III) oxide O(1s) features are not met with the same agreement, but are still considered to be within experimental error at 2.8 and 2.4 eV, respectively [58,62]. The reported binding energy values reported by these two research groups are presented in Table 4.1.

Table 4.1 Reported literature values for O(1s) binding energies (eV) of reported species identified during photoemission (XPS) experiments on cerium oxides [58,62]

Investigators	Ce(IV) oxide	Ce(III) oxide	Hydroxyl (-OH)
Mullins *et al.*	530.4 eV	530.7 eV	533.5 eV
Koel *et al.*	529.6 eV	530.2 eV	532.7 eV

4.4 DATA ACQUISITION

As in the acquisition of the S(2p) spectra, the system employed in the acquisition of O(1s) spectra consisted of a Physical Electronics Model 1600 Multitechnique UHV system with a base pressure of 5×10^{-10} Torr. The system is capable of AES, ISS, and XPS analyses. The electron energy analyzer is a multichannel spherical capacitance analyzer (SCA) operated with a 23.5 eV pass energy. The X-ray source is a dual-anode source capable of delivering achromatic Mg Kα and Al Kα X-rays. During all experiments, spectra were obtained using Mg Kα X-rays at 15 kV and 300 watts, under vacuum maintained at or below 5×10^{-9} Torr. The energy resolution of the SCA is 1.07 eV, which was determined by finding the full-width at half maximum (FWHM) of the $4f_{7/2}$ gold core electron line as obtained using a suitable gold calibration foil.

The high resolution photoemission spectral data were acquired using PHI Surface Analysis Software in the Multiplex data acquisition mode (to collect several spectral regions simultaneously). Spectra were charge compensated to the adventitious Carbon 1s line at 284.8 eV as described in the literature [41]. Data analysis and curve deconvolution is accomplished using XPS International Spectral Data Processor software v. 4.1. The O(1s) spectra were collected before and after controlled exposures to SO_2/N_2 gas as described in Chapter 3.

4.5 RESULTS

4.5.1 O(1s) Spectral Symmetry

The collected O(1s) spectra for ceria samples have strong symmetrical likeness with the data presented in the literature by Mullins *et al.* and Koel *et al.* In addition, the binding energy positions for ceria-rich samples are also very similar to those reported, especially those obtained by Koel *et al.* The O(1s) spectra, before and after a 15 minute exposure to 20 ppm SO_2/N_2 gas at 673 K and 1000 torr, are presented as offset spectra in Figures 4.1 and 4.2 for pure ceria and zirconia, respectively. Overlaying the same spectra provides additional insight into the changes which are occurring on these surfaces. Figures 4.3 and 4.4 are the same group of four spectra, displayed in an overlaid fashion, to show spectral differences more readily. The spectra collected under these conditions were chosen for closer examination because they represent the most sulfating conditions employed in this study, as described by the sulfur 2p data and results in Chapter 3.

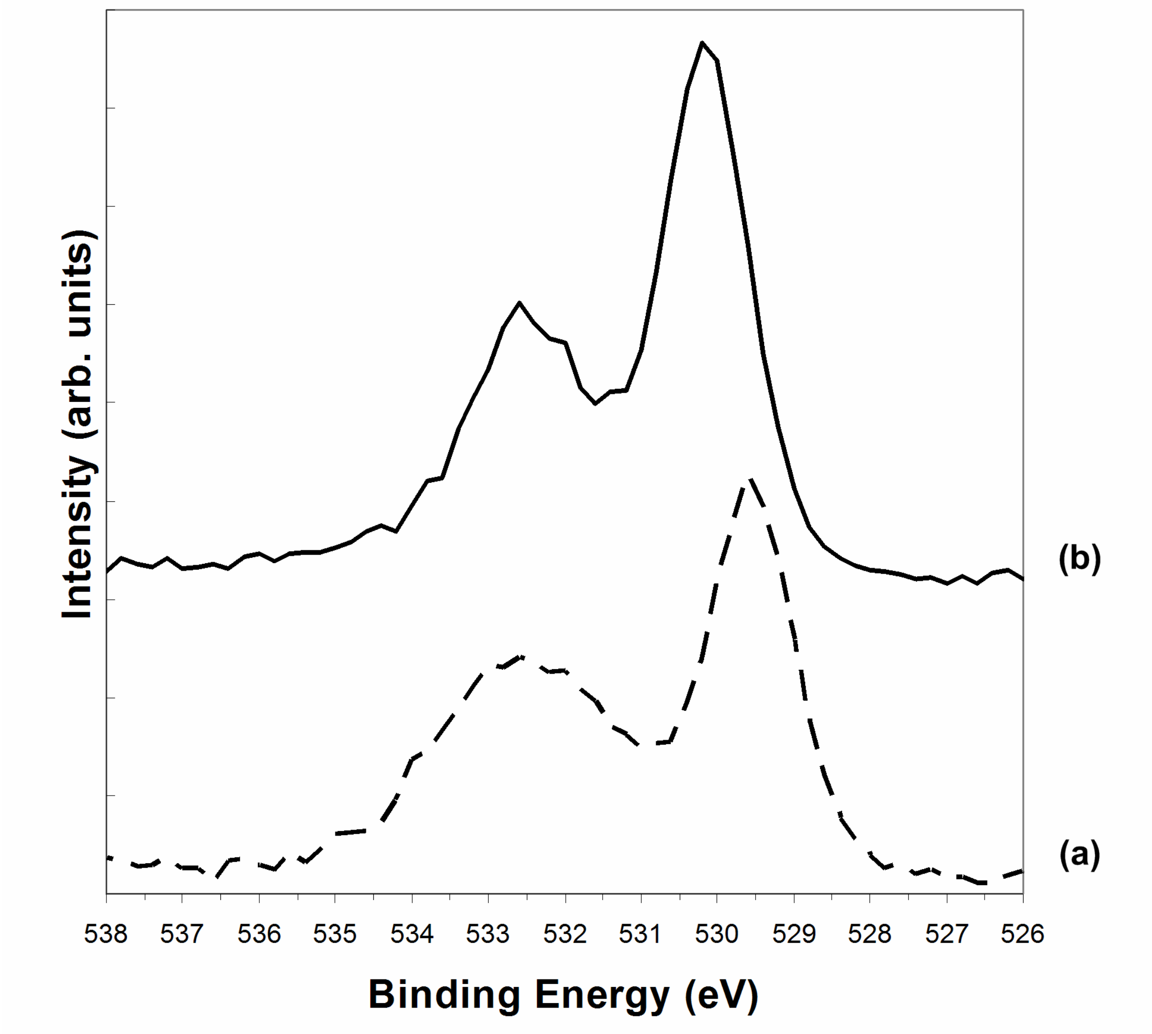

Figure 4.1 High resolution O(1s) XPS spectra of pure ceria taken (a) prior to exposure and (b) after a 15 minute exposure to 20 ppm SO_2/N_2 gas at 673 K and 1000 torr

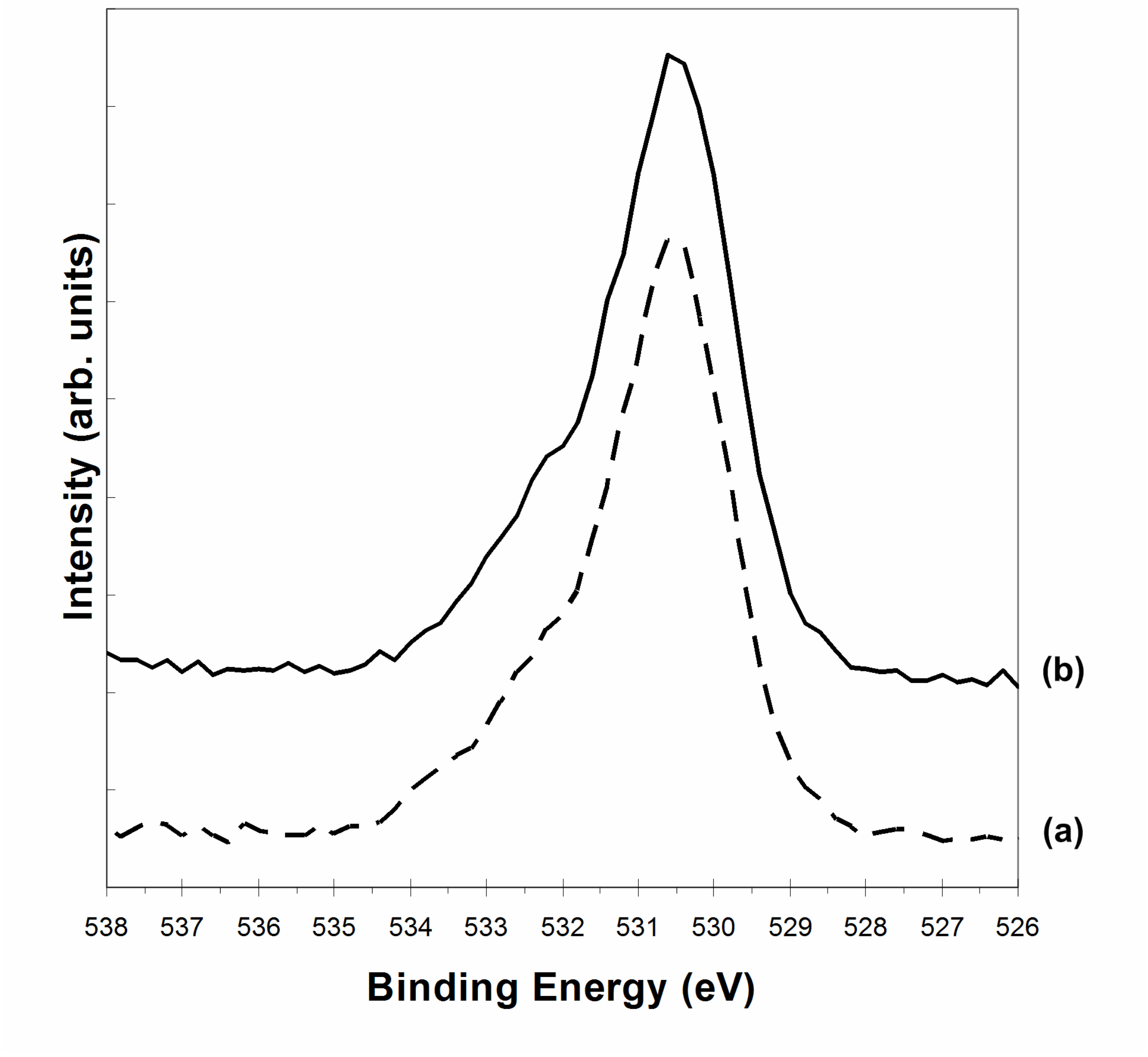

Figure 4.2 High resolution O(1s) XPS spectra of pure zirconia taken (a) prior to exposure and (b) after a 15 minute exposure to 20 ppm SO_2/N_2 gas at 673 K and 1000 torr

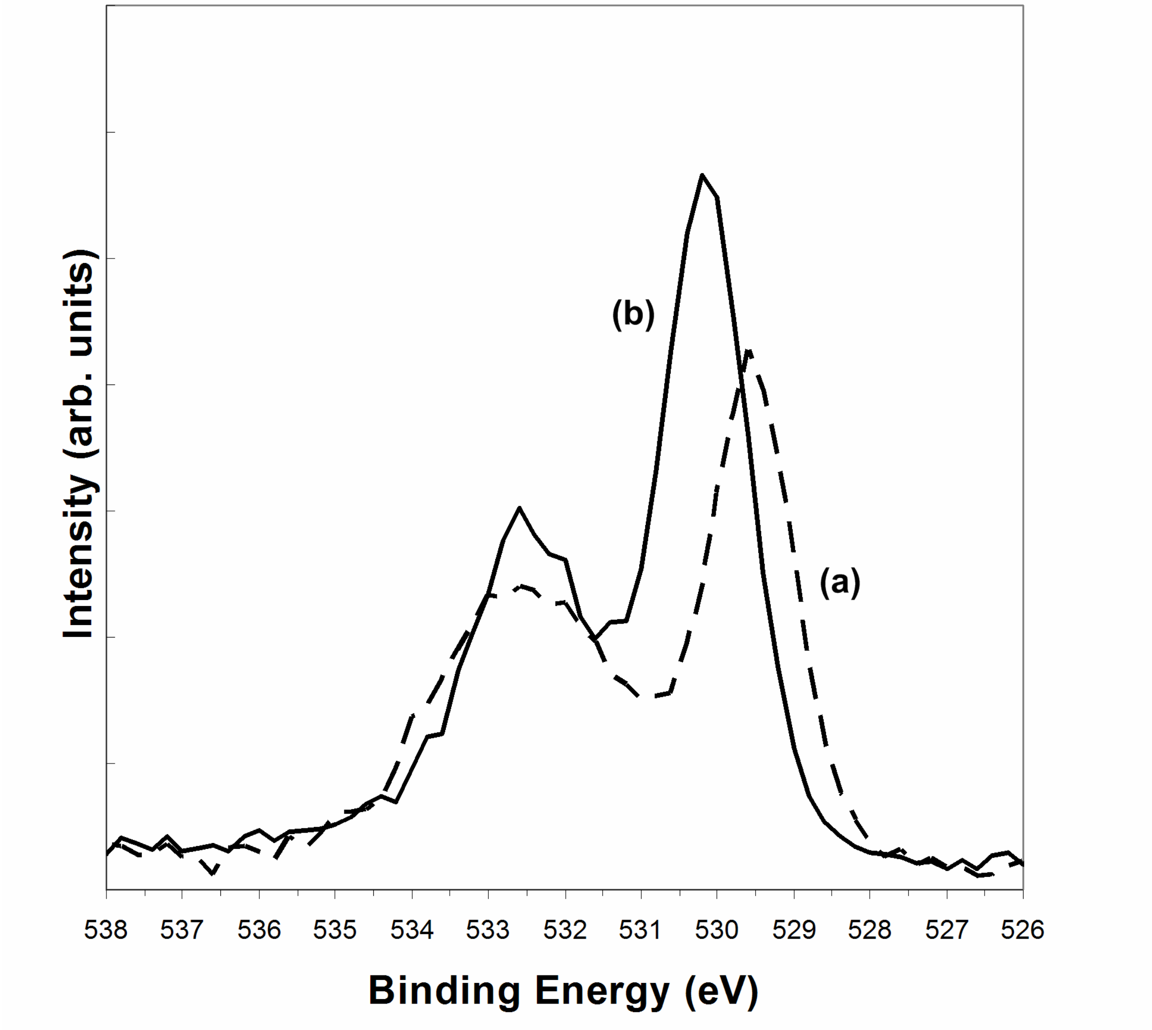

Figure 4.3 High resolution O(1s) XPS spectra of pure ceria taken (a) prior to exposure and (b) after a 15 minute exposure to 20 ppm SO_2/N_2 gas at 673 K and 1000 torr

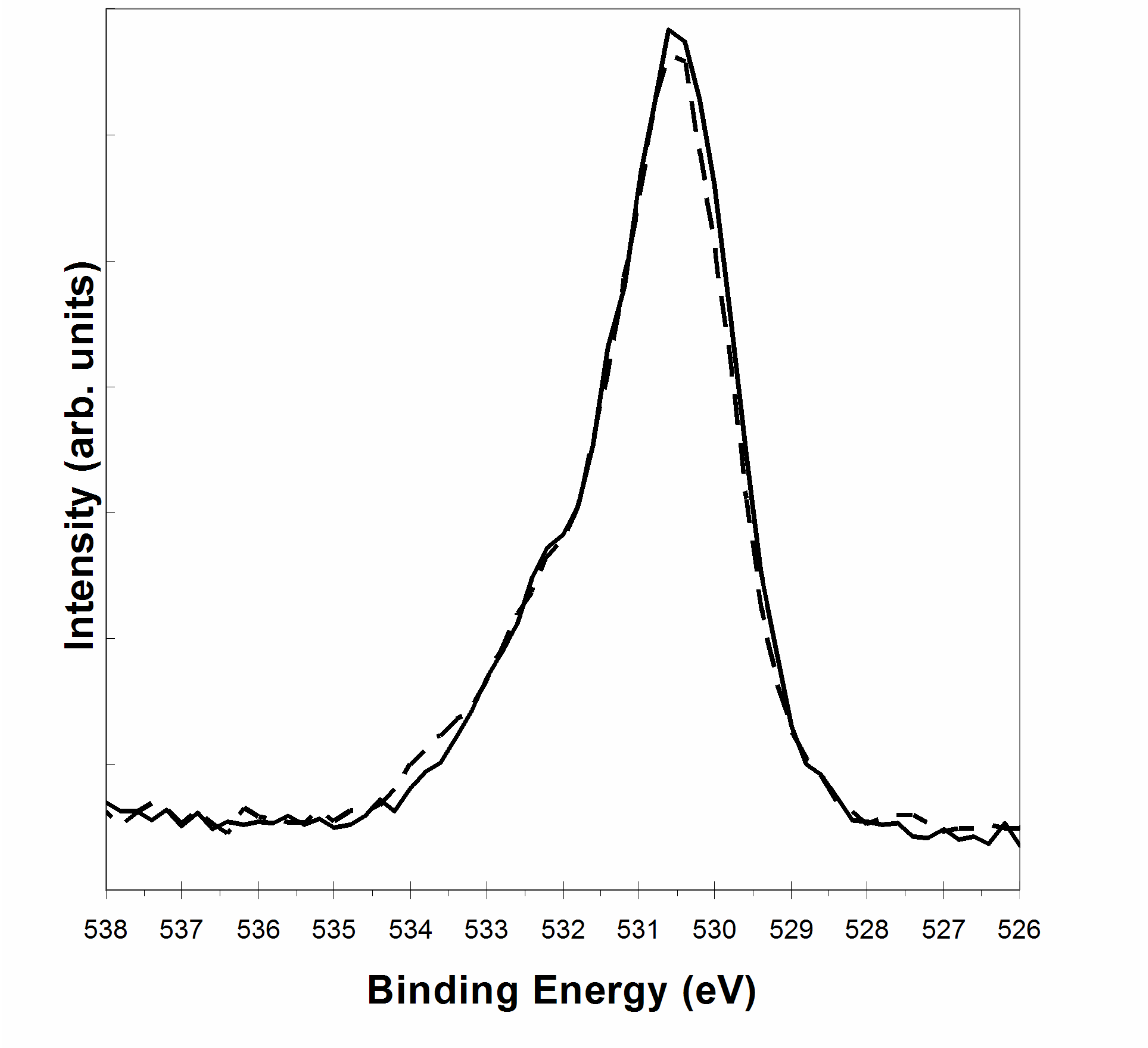

Figure 4.4 High resolution O(1s) XPS spectra of pure zirconia taken prior to exposure (dashed), and after a 15 minute exposure to 20 ppm SO_2/N_2 gas at 673 K and 1000 torr (solid line)

In Figure 4.3, the overlay spectra show subtle, yet very important, differences in the O(1s) high resolution (HR) XPS spectra for ceria. It is evident from the curve symmetry that there are two features present, one at a lower binding energy and another at a somewhat higher binding energy. The principal O(1s) feature, at approximately 530 eV binding energy, is attributed to the metal oxide's lattice oxygen atoms, which is in good agreement with values reported in the literature [58,62]. The line feature at higher binding energy is attributed to the presence of surface terminating hydroxyl groups, and is centered at a binding energy between 532 and 533 eV, again in good agreement with the values reported in the literature [58,62].

In Figure 4.4, the O(1s) HR spectra for zirconia are overlaid after employing the same exposure conditions as those used for ceria in Figure 4.3. Remarkably, no significant change in the O(1s) feature is visible due to exposure of the metal oxide to the most sulfating conditions employed in this study. However, it should be noted that, as in the case of ceria, there are two O(1s) features for zirconia as evidenced by the asymmetrical shape of the spectra on the high-binding energy side of the O(1s) feature.

4.5.2 Curve Peakfitting

Curve peakfitting allows a more precise measurement of binding energies and relative peak areas for any of the features identified in the group of O(1s) spectra. Figures 4.5 thru 4.8 show the peakfitted O(1s) data for ceria and zirconia as obtained using XPS International Spectral Data Processor v. 4.1.

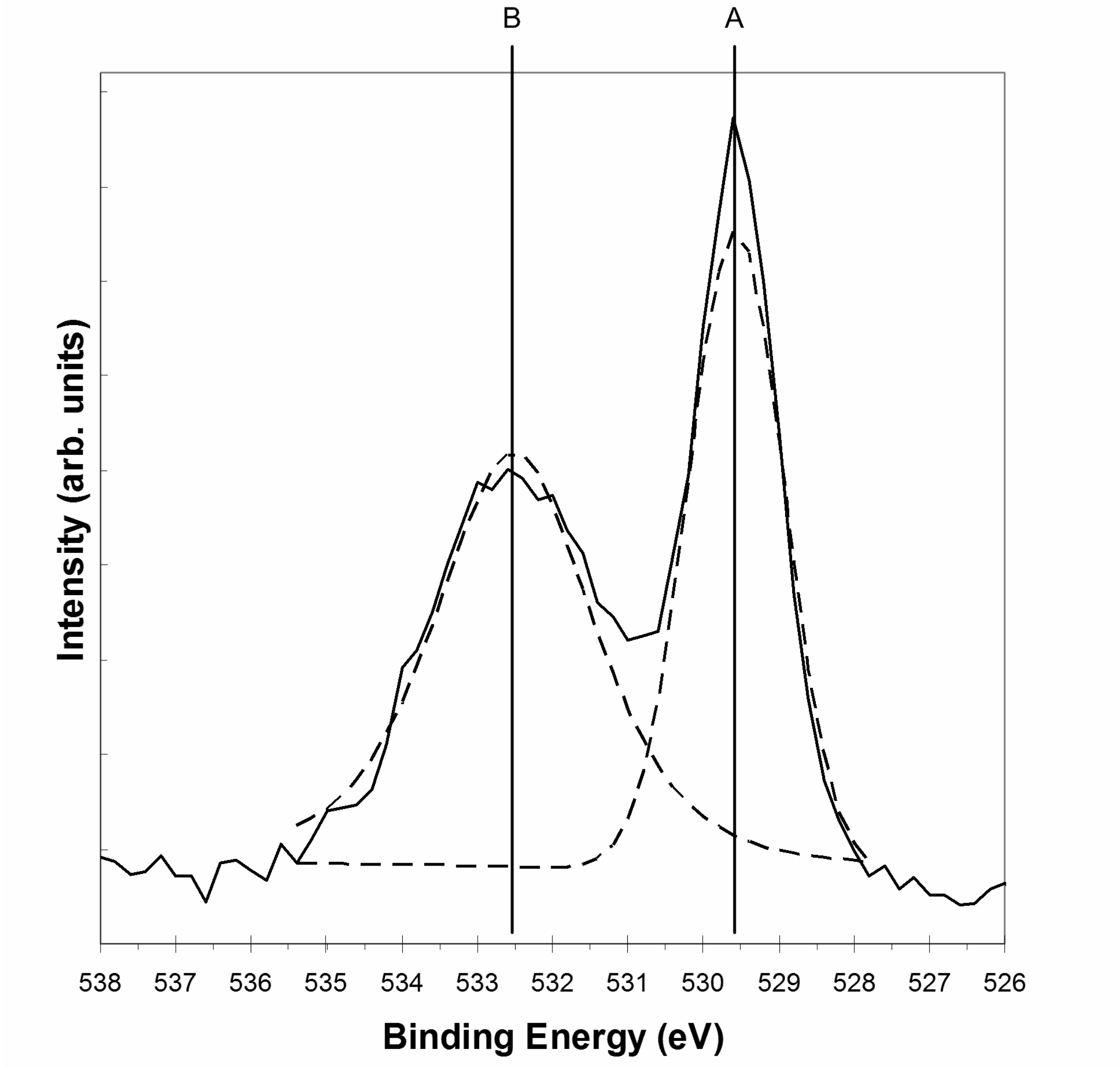

Figure 4.5 High resolution O(1s) XPS spectra and curve deconvolution for pure ceria taken prior to SO_2 exposure. Peak A is attributed to metal oxide lattice oxygen atoms and Peak B is due to oxygen atoms bound in surface hydroxyl groups

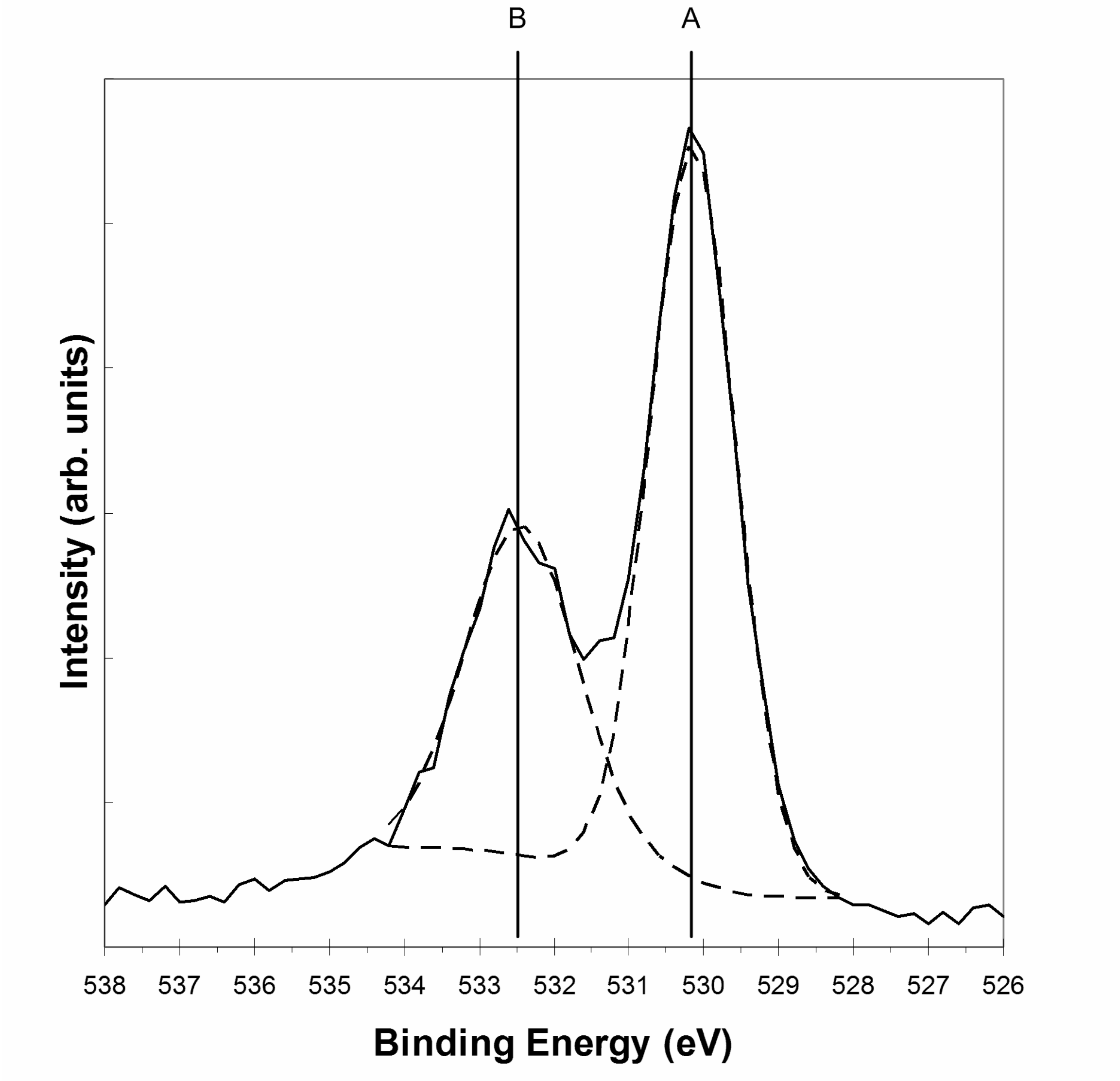

Figure 4.6 High resolution O(1s) XPS spectra and curve deconvolution for pure ceria taken after a 20 ppm SO_2 gas exposure at 673 K and 1000 T for 15 minutes. Peak A is attributed to metal oxide lattice oxygen atoms and Peak B is due to oxygen atoms bound in surface hydroxyl groups

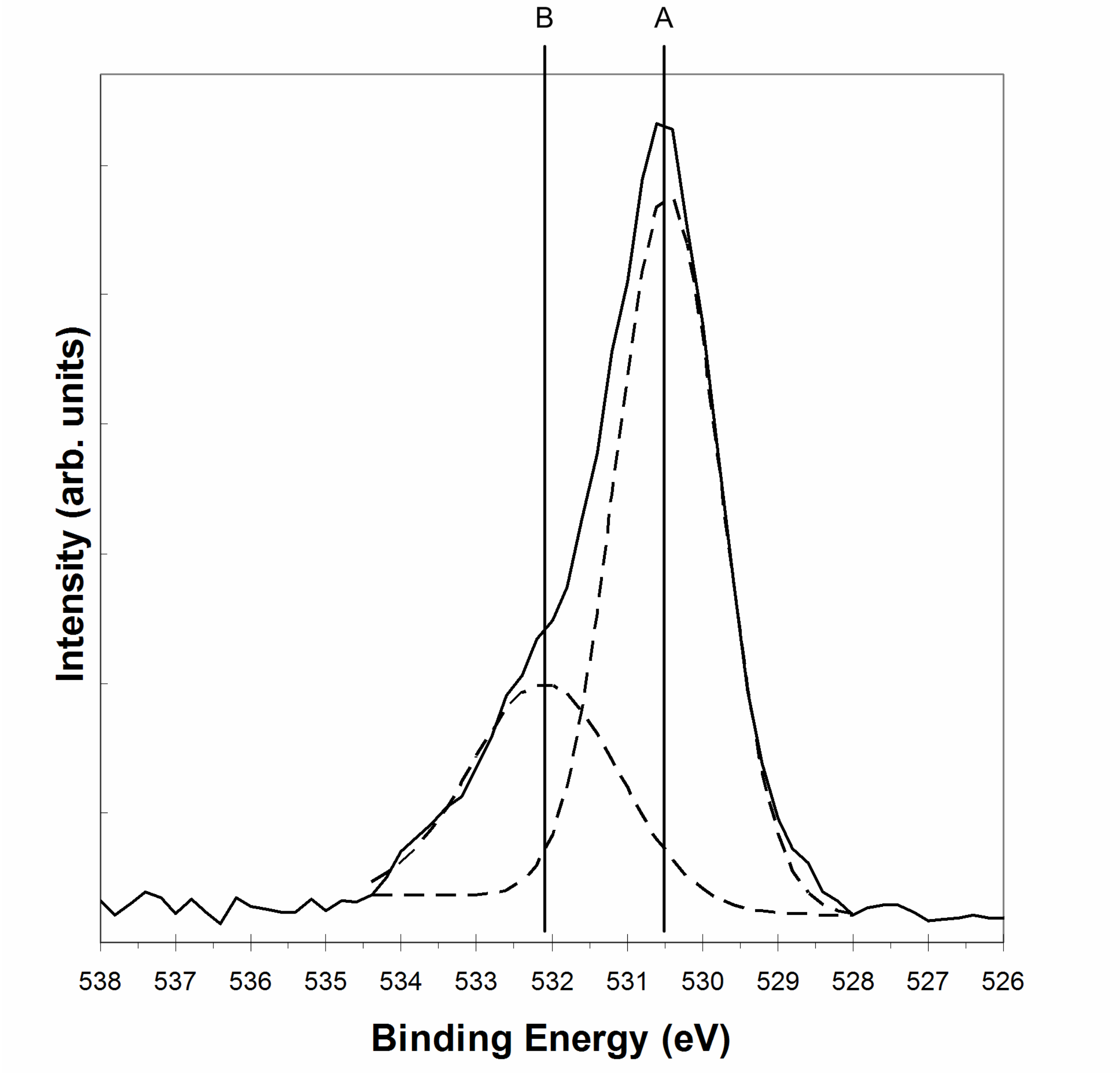

Figure 4.7 High resolution O(1s) XPS spectra and curve deconvolution for pure zirconia taken prior to SO_2 exposure. Peak A is attributed to metal oxide lattice oxygen atoms and Peak B is due to oxygen atoms bound in surface hydroxyl groups

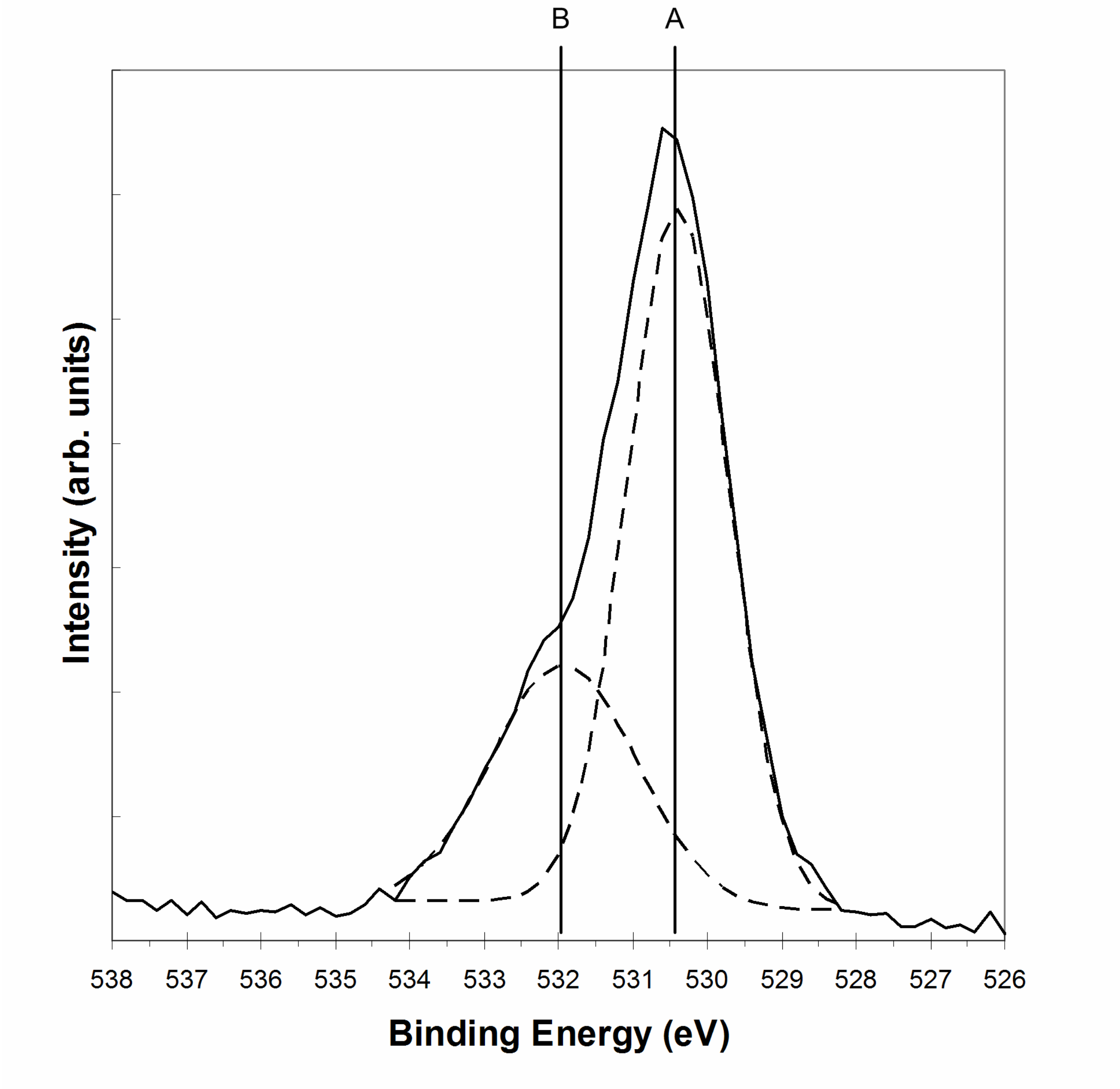

Figure 4.8 High resolution O(1s) XPS spectra and curve deconvolution for pure zirconia taken after a 20 ppm SO_2 gas exposure at 673 K and 1000 T for 15 minutes. Peak A is attributed to metal oxide lattice oxygen atoms and Peak B is due to oxygen atoms bound in surface hydroxyl groups

In the case of ceria, it is interesting to note the slight shift in the binding energy attributed to lattice oxygen upon exposure to the SO_2/N_2 gas at the aforementioned conditions. This binding energy shift of 0.6 eV, as measured, indicates the reduction of cerium from Ce(IV) to Ce(III) is in fact taking place under these exposure conditions as reported in the literature [58,62].

The negligible changes in the zirconia O(1s) signatures from exposure to sulfating conditions are supported by almost identical peak fitting data for post- and pre-exposure spectra. The peakfits do, however, reveal the presence of a second O(1s) feature, partially hidden in the asymmetry of the principal O(1s) signature, that is much closer to the principal O(1s) feature than observed in the case of ceria.

The broadness of all the O(1s) peaks encountered indicate some degree of static charge buildup. The buildup of static charge is a well-known phenomena on the surface spectroscopy of these metal oxides [31,58]. This is likely due to the extremely thick nature of the samples employed and the inherent electrical insulating properties of the oxides employed in this study [58].

Table 4.2 summarizes the binding energy data for the species identified using the O(1s) XPS data for ceria and zirconia. In addition, Table 4.3 and 4.4 summarize the relative peak areas of each type of oxygen signature, lattice or hydroxy, that is found on the spectra for each of the six compositions described in Chapter 3. The data presented in Tables 4.3 and 4.4 make it possible to create a chart showing composition and/or exposure temperature trends, if any exist under the conditions examined.

Table 4.2 Reported values for O(1s) XPS binding energies of reported species on pure ceria and zirconia metal oxides. Exposure condiitons of 15 min., 20 ppm SO_2, 1000 T, and 673 K

Metal Oxide	Ce(IV) oxide	Ce(III) oxide	Zr(IV) oxide	Hydroxyl
Ceria (pre-exposure)	529.6 eV	-	-	532.6 eV
Ceria (post-exposure)	-	530.2 eV	-	532.6 eV
Zirconia (pre-exposure)	-	-	530.5 eV	532.1 eV
Zirconia (post-exposure)	-	-	530.4 eV	531.9 eV

Table 4.3 Relative O(1s) peak areas attributed to hydroxy and lattice oxygen atoms prior to treatment with SO_2 for all CZMMO compositions examined

Composition (mol% ceria)	298 K		473 K		673 K	
	Hydroxy	Lattice	Hydroxy	Lattice	Hydroxy	Lattice
100	7333.2	6756.3	9014.8	6636.1	8535.5	6859.9
90	9508.2	6882.6	9560.1	5859.9	9557.7	7271.1
70	10488.6	6412.9	9965.3	6922.6	8851.2	7299.4
50	8037.4	6757.7	9524.0	6639.4	9710.2	7116.7
20	8866.5	7975.3	8865.2	6379.4	8865.1	8853.8
0	6320.0	10315.8	6428.1	11609.9	6467.3	11890.8

Table 4.4 Relative O(1s) peak areas attributed to hydroxy and lattice oxygen atoms after 15 minute exposure to 20 ppm SO_2 at 1000 T and the temperature listed in the table for all CZMMO compositions examined

Composition (mol% ceria)	298 K		473 K		673 K	
	Hydroxy	Lattice	Hydroxy	Lattice	Hydroxy	Lattice
100	8133.7	6780.4	5169.9	8425.4	5937.7	9800.2
90	9561.0	5813.2	5608.4	8330.5	6784.9	8816.9
70	9451.5	6043.1	6011.9	8008.7	6735.7	9434.7
50	8733.4	6478.6	5919.9	8571.2	6959.9	10651.2
20	9028.3	7767.6	4651.2	8996.5	5663.8	11719.8
0	6208.8	10050.4	4362.9	15287.9	3885.3	14461.3

Figures 4.9 and 4.10 utilize the aforementioned data to illustrate the change in the percentage of O(1s) signature attributed to hydroxyl oxygen as a function of composition and exposure conditions on the CZMMO materials that were investigated. The trends that are visible include a noticeable decrease in the hydroxyl O(1s) signature as the composition becomes zirconia rich, which is independent of post- or pre-exposure measurements. Additionally, a strong temperature dependency exists, with higher SO_2/N_2 treatment temperatures resulting in significant drops in the O(1s) – hydroxyl oxygen peak areas relative to the overall oxygen signature. However, the difference between the exposures performed at 473 and 673 K show only a small difference that is within the error assumed with the peakfitting routine and data acquisition processes.

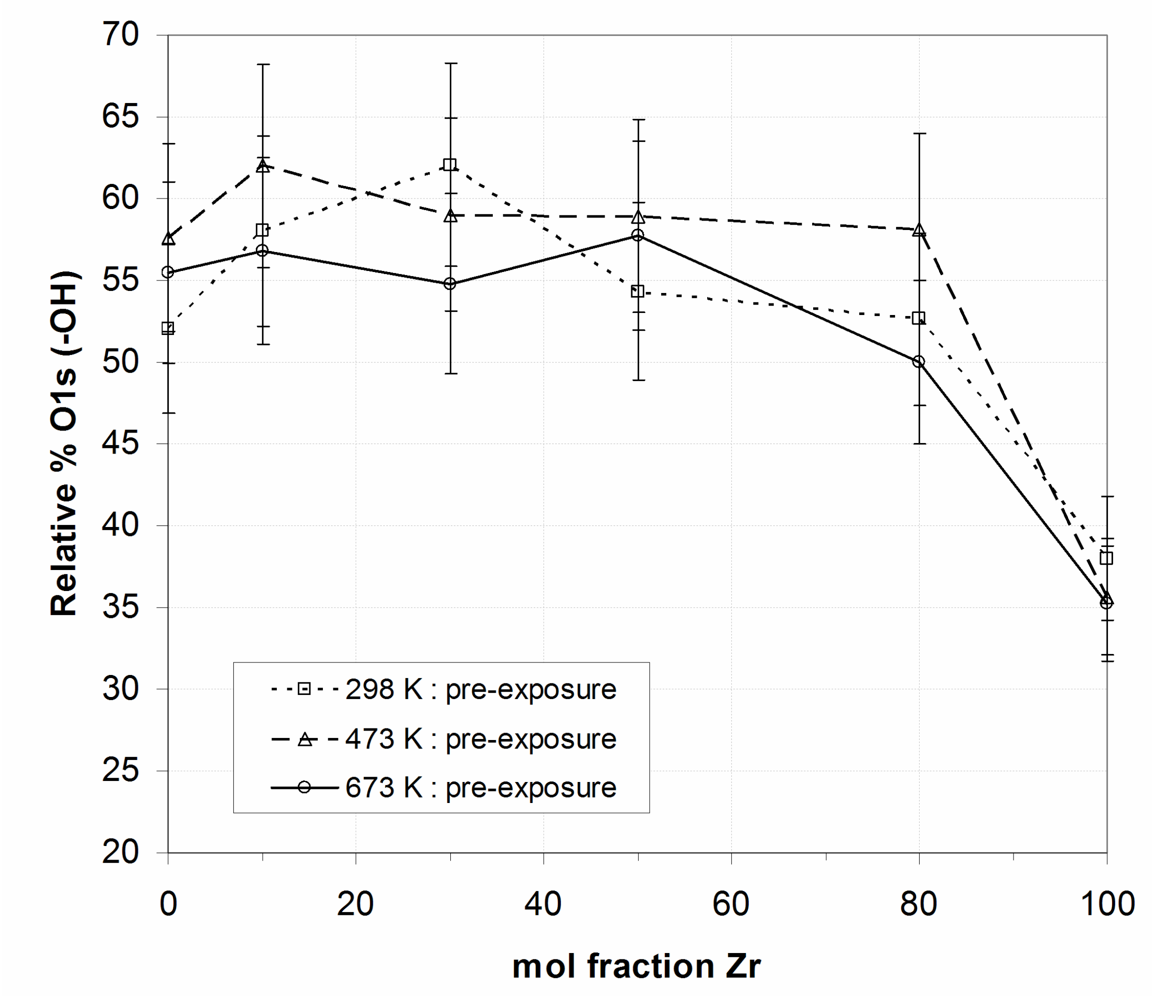

Figure 4.9 Percentage of O(1s) peak area attributed to hydroxyl (-OH) oxygen species, prior to any treatment

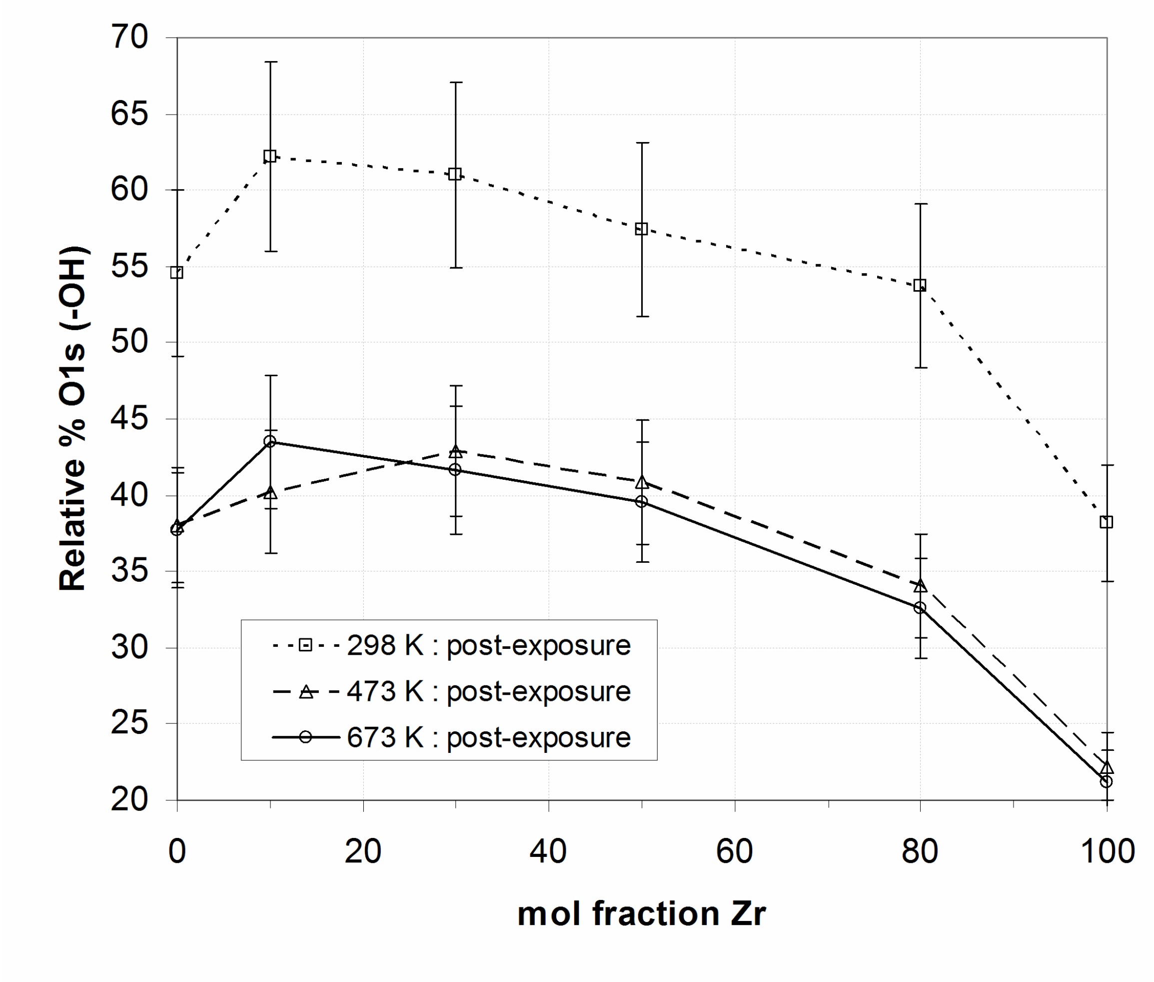

Figure 4.10 Percentage of O(1s) XPS peak area attributed to hydroxyl (-OH) oxygen species, after a 15 minute 20 ppm SO_2/N_2 treatment at 1000 T and 298, 473, or 673 K

4.6 DISCUSSION

The presence of terminal hydroxyl groups on this class of materials comes as no surprise, since the synthesis procedure employs an aqueous salt co-precipitation technique described elsewhere [22-24]. In this synthesis technique, hydroxyl species are readily available - partly from the water used to make the aqueous salt solution. Water has been shown to dissociate into hydroxy species on cerium metal surfaces [62]. In addition, the salt solution used in the synthesis procedure has its pH adjusted for precipitation using excess ammonium hydroxide. This fact ensures that hydroxide ions will be present to form stable surface hydroxyl groups as the metal oxide is precipitated out of solution. These stable surface hydroxyl species cannot escape with the other entrained ammonium, nitro, and oxynitrate compounds during the water washing and calcination steps.

The collected XPS data show the presence and the binding energies associated with these hydroxyl species on the CZMMO compositions that were examined. The data acquired for ceria is very comparable to that reported in the literature [58,62]. The ease with which ceria transitions from the Ce(IV) to Ce(III) oxidation state is an illustration of its commercial importance in the production of emissions control catalysts. Likewise, this unique property can also be detrimental, since ceria has also shown a higher propensity for adsorption of SO_2 as described in

Chapter 3. The deactivation of ceria-based catalysts arising from exposure to SO_2 may be attributed to an irreversible reaction from the Ce(IV) to Ce(III) oxidation state in conjunction with the consumption of surface-terminating hydroxyl groups.

The unwavering nature of the zirconia O(1s) signature under the conditions of this study demonstrates that zirconia is a very stable addition to emissions control catalyst compositions. As demonstrated in Chapter 3, zirconia-rich MMO's do not adsorb SO_2 with the propensity that ceria does, indicating that zirconia may help reduce long-term catalyst deactivation phenomena. However, the effect of zirconia on the oxygen storage capacity (OSC) of a catalyst composition may or may not be beneficial. Zirconia is known to be an excellent oxygen anion conductor, but further measurements of the effects of zirconia on OSC properties of a catalyst is beyond the scope of this investigation [2].

The loss of surface hydroxyl species must be due to a reaction occurring with SO_2. The highest SO_2 treatment temperature was 673 K. More importantly, significant loss of surface hydroxyl functionalization was experienced with SO_2 treatments performed at temperatures as low as 473 K. Hydroxyl group loss cannot be attributed to heating alone, since the SO_2 treatment temperatures and durations are significantly lower than the CZMMO calcination conditions of 773 K for one hour. In addition, the stability of the surface hydroxyl species under heating to 673 K was verified spectroscopically by XPS.

Interestingly, the greatest net loss of hydroxyl group signature upon exposure to sulfur dioxide occurs for the conditions which have simultaneously been shown to have the most significant level of sulfate and sulfite surface sulfur species formation. This finding shows that the loss of hydroxyl groups and the adsorption of sulfur dioxide are related phenomena. In particular, this supports the results obtained in the work by Overbury *et al.* in which hydrogen sulfite (HSO_3^-) species were reported and found to be a chemically viable transformation []. The formation of HSO_3^- species would require the transfer of a proton from a surface-residing lattice oxygen atom to a sulfur dioxide surface complex adsorbing at a specific site on the oxide surface. This, in turn, would result in diminished hydroxyl oxygen signatures in the XPS spectra, since the proton is now part of a different entity - a HSO_3^- species. The formation of hydrogen sulfites species have been shown by other investigators to be chemically viable under similar conditions, and the S(2p) and O(1s) data shown here provide evidence that this species is also forming under the conditions of this study.

CHAPTER V

CZMMO CERIUM AND ZIRCONIUM PHOTOEMISSION

5.1 HIGH RESOLUTION PHOTOEMISSION SPECTRA OF CE AND ZR

In Chapter IV, oxygen containing species on CZMMO materials have been identified and have been shown to play an important role in the adsorption of SO_2 on these metal oxides. The formation of sulfite (SO_3) and sulfate (SO_4) species on this group of metal oxides upon exposure to SO_2 indicates that the SO_2 molecules either interact with surface residing lattice oxygen atoms or hydroxyl groups. However, it is also possible that the SO_2 molecules are interacting with the metal oxide's metal centers with subsequent transfer of oxygen and formation of a bond between nearby oxygen atoms and the adsorbed sulfur atom. This transfer of oxygen from nearby lattice structure would act to locally reduce the surface of the metal oxide. Metal reduction has already been elucidated for ceria in Chapter IV using O(1s) high resolution XPS spectral data. The lack of SO_2 adsorption on zirconia-rich metal oxides and the remarkable stability of the O(1s) HR XPS data for zirconia indicate that zirconium does not have the flexibility to undergo changes in oxidation state under the conditions of this study as cerium atoms do in cerium-rich metal oxides. To support this claim, figure 5.1 shows the zirconium 3d high resolution XPS spectra taken from a pure zirconia metal oxide sample (a) prior to any heating or exposure to SO_2 and (b) after the most vigorous treatment employed in this study at the conditions of 673 K, 20 ppm SO_2/N_2 for 15 minutes at a pressure of 1000 torr. In these spectra for zirconia, remarkable reproducibility of the zirconium $3d_{5/2}$ and $3d_{3/2}$ spin-orbits are obtained for pre-exposure and post-exposure data acquisitions. The difference in the binding energy of these spin-orbit states is 2.37 eV for both data acquisitions, which is within one tenth of an electron volt from the value of 2.43 eV which is reported in the literature [25]. In addition, a Zr($3d_{5/2}$) binding energy for ZrO_2 at 181.9 eV, is fully consistent with the reported binding energy for zirconia [25]. Because of the unwavering nature of zirconia in these metal oxides, it is imperative to elaborate in detail, the fine structure and changes that take place in cerium 3d core level photoemission spectral data upon the various treatments used in this investigation.

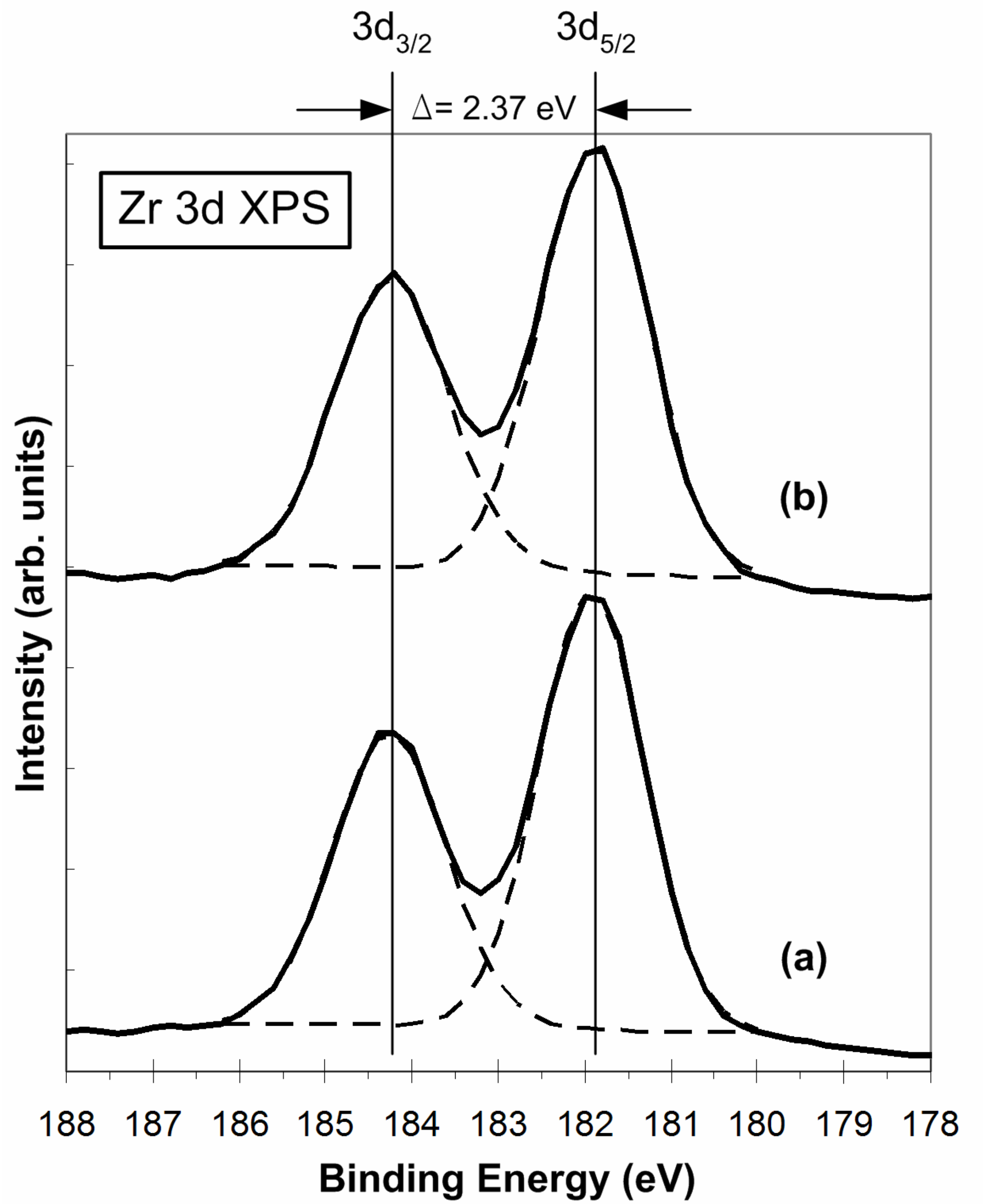

Figure 5.1 High resolution Zr(3d) XPS spectra of pure zirconia taken (a) prior to exposure and (b) after a 15 minute exposure to 20 ppm SO_2/N_2 gas at 673 K and 1000 torr pressure

5.2 CERIUM PHOTOEMISSION

5.2.1 Overview

The ability of cerium (Ce) to switch oxidation state from (IV) to (III) in ceria makes it an important commercial material and a challenge of great interest to the electron spectroscopist. XPS can be used to easily identify the oxidation state of the cerium atoms inside the sampling volume. For elemental cerium metal, the characteristic Ce(3d) photoemission occurs in two spin-orbit states, $3d_{5/2}$ and $3d_{3/2}$, which have binding energies of 884 and 902 eV, respectively [25]. There is a vast collection of literature available which details the application of electron spectroscopy in studying the Ce(3d) photoemission in cerium oxide and related materials [15,46,58,61-63,65-76].

5.2.2 XPS spectral features of cerium oxide

Complex Ce(3d) core level signatures arise in cerium oxide from variable cerium (4f) electron final occupation states [58,68-69,77-80]. Valence band techniques can be employed to study the final cerium 4f levels, however this is not an objective of this study [58]. It has been suggested that differences in the details of sample preparation and characterization methods have led to the controversy surrounding the structure of the core level Ce(3d) signatures in the literature [58]. In addition, peakfitting routines may vary from laboratory to laboratory, resulting in yet another potentially significant source of error between data obtained from different laboratories.

The deconvolution of Ce(3d) spectra from UHV cleaned cerium metal results in two peaks, one each for the spin-orbits $3d_{5/2}$ and $3d_{3/2}$ [25,62]. This can be considered the simplest-case of data for cerium oxides, which contain multiples of doublets [58,69]. Therefore, deconvolution of the Ce(3d) signal from cerium oxides is not as straightforward. Various investigators report anywhere from 4 to 10 peaks after performing Ce(3d) curve deconvolution for fully oxidized cerium (IV) oxide samples [58,61-63,66-69]. However, the overall spectral shape and unique features of the Ce(3d) data often serve as a better indication of the cerium oxidation state from the acquired spectra.

5.2.3 Determination of oxidation state

Of utmost importance in this investigation is the utility of XPS in detecting the spectral difference between cerium (IV) and cerium (III) oxide surfaces. It has been specifically shown that XPS can be used to readily distinguish fully oxidized cerium (IV) oxide surfaces from reduced cerium (III) oxide surfaces [15,58,63,69].

Perhaps no-one has shown this more clearly than Mullins *et al.* who demonstrated that fully oxidized cerium (IV) oxide possesses a unique and strong photoemission peak at a binding energy of approximately 916 eV, which is absolutely devoid in fully reduced cerium (III) oxide surfaces [58]. In addition, the work by Mullins *et al.* shows six photoemission signatures for cerium (IV) oxide with significantly clearer peak resolution than some of the earlier works [58]. This may be attributed to the increased instrumental energy resolution of modern spectrometers employing monochromators, over older systems that rely on achromatic x-rays. Mullins *et al.* quantifies the energy resolution of the system employed in their work as being <0.3 eV, which is significantly lower than the 1.1 eV line-width resolution achieved in most unmonochromated systems [58]. However, in all the references cited and without precise peakfitting, the spectral shape of the Ce(3d) region for cerium (IV) oxide results in a number of photoemission signatures in close proximity to each other at binding energies between 880 and 910 eV. These peaks, being in such close proximity to each other, have been the source of some of the controversy found in the literature in regards to peakfitting. However, the signature at 916 eV stands in relative isolation as compared to the other Ce(3d) signatures between 880 and 910 eV. This spectral feature at 916 eV is the $3d_{3/2}$ spin-orbit for the highest binding energy Ce(3d) doublet for cerium (IV) oxide. Interestingly, this feature is in relative isolation compared to the other Ce(3d) components due to the 16-18 eV separation between the two spin-orbit states and the corresponding binding energy of the $3d_{5/2}$ component, which lies in the midst of the other two doublets' $3d_{3/2}$ components [58].

Fortunately, the Ce(3d) peak at 916 eV is absent in cerium (III) oxide offering a convenient method of identifying the oxidation state of the cerium atoms in the analysis volume using XPS [58,63,68,73]. For cerium (III) oxide, only four peaks (two doublets) are present in cerium (III) oxide core level photoemission spectra [58].

5.3 DATA ACQUISITION

As in the acquisition of the other high resolution spectra acquired for use in this study, the system employed consists of a Physical Electronics Model 1600 Multitechnique UHV system with a base pressure of 5×10^{-10} Torr. The system is capable of AES, ISS, and XPS analyses. The electron energy analyzer is a multichannel spherical capacitance analyzer (SCA) operated with a 23.5 eV pass energy. The X-ray source is a dual-anode source capable of delivering achromatic Mg Kα and Al Kα X-rays. During all experiments, spectra were obtained using Mg Kα X-rays at 15 kV and 300 watts, under vacuum maintained at or below 5×10^{-9} Torr. The energy resolution of the SCA is 1.07 eV, which was determined by finding the full-width at half maximum (FWHM) of the $4f_{7/2}$ gold core electron line as obtained using a suitable gold calibration foil.

The high resolution photoemission spectral data were acquired using PHI Surface Analysis Software in the Multiplex data acquisition mode (to collect several spectral regions simultaneously). Spectra were charge compensated to the adventitious Carbon 1s line at 284.8 eV as described in the literature [41]. Data analysis and curve deconvolution is accomplished using XPS International Spectral Data Processor software v. 4.1. The Ce(3d) spectra were collected before and after controlled exposures to SO_2/N_2 gas under the same conditions described in Chapters 3 and 4. In addition, argon ion sputtering was employed to verify that the starting cerium (IV) oxide could be reduced to cerium (III) oxide using this method as reported in the literature by Mullins *et al.* [58].

5.4 RESULTS

For reference and verification of the starting cerium oxidation state in the metal oxides used in this study, pre- and post-treatment spectra were collected. The treatments used included an argon ion sputtering run for the demonstration of surface reduction leading to cerium (III) oxide surfaces. The acquisition of these data sets is important for future comparison with other spectra collected after the treatments of interest in this research. The principal interaction of interest in this study is that of sulfur dioxide (SO_2) with these metal oxides, and therefore, it is imperative to monitor any changes in the cerium oxidation state that may have occurred as the result of an interaction between SO_2 and cerium or nearby lattice oxygen atoms.

Figure 5.2 is a composite graph showing (a) the Ce(3d) spectra for a fresh ceria wafer. The spectral shape shows strong similarities to the data obtained by some of the other investigators, especially Mullins *et al.* In particular, the strong photoemission at approximately 916 eV shows that in this case the ceria surface is fully oxidized and hence, in the cerium (IV) oxidation state. Three sets of doublets can be envisioned, each with a spin-orbit splitting of approximately 18 eV. The approximate position of the peaks are shown by the arrows and letter assignments, with the letter "V" denoting the Ce($3d_{5/2}$) and "U" denoting the Ce($3d_{3/2}$) spin-orbit states, respectively. Unprimed, primed, and doubly-primed letters in this composite graph each indicate a distinct final Ce(4f) occupation state as previously discussed.

In figure 5.2(b), the same spectral region is displayed for the same ceria wafer after being subjected to 15 minutes of 1.5 keV argon ion sputtering to demonstrate reduction of the ceria surface to the cerium (III) oxidation state as described in the literature [58]. Indeed, after sputtering and subsequent evacuation, spectral differences arise that indicate the presence of a fully reduced cerium (III) oxide surface upon

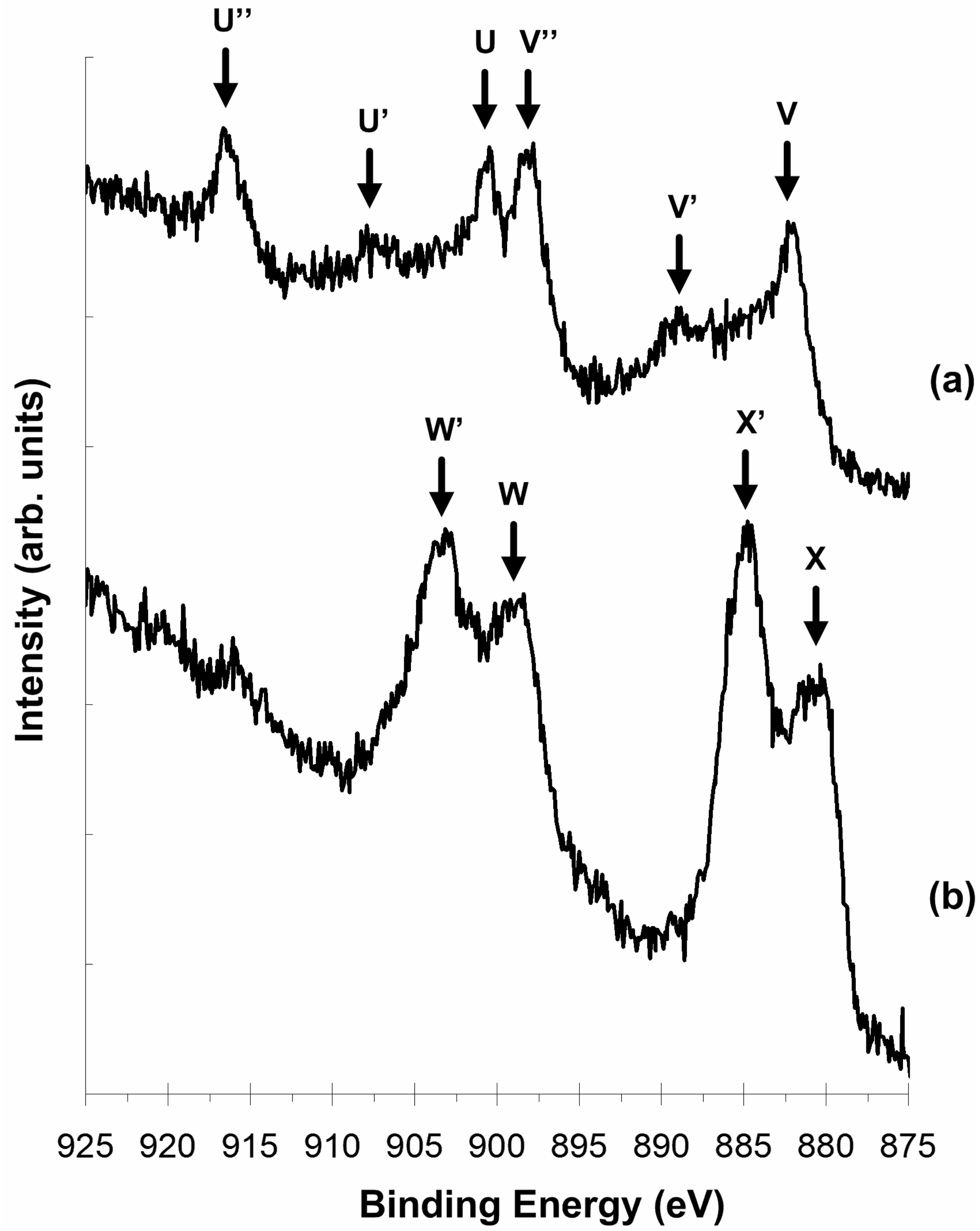

Figure 5.2 High resolution Ce(3d) XPS spectra for ceria taken (a) prior to any treatment and (b) after 15 minutes of 1.5 keV Ar$^+$ ion sputtering at θ=138°

sputtering. The most significant difference in the spectra is the complete absence of the Ce($3d_{3/2}$) photoemission that occurs at approximately 916 eV for cerium (IV) oxide. This is clear evidence that the ceria surface has been reduced to the cerium (III) oxidation state. In addition, small shifts in the binding energy and curve shape of the other Ce(3d) components is fully consistent with reported binding energy data obtained for cerium (III) oxide [58,63]. Since fully oxidized and reduced ceria Ce(3d) baseline spectra have been collected, it is now possible to investigate the effect of other treatments on the oxidation state of cerium in these metal oxides.

In particular, of most interest in this study are the set of conditions employed which yield the greatest level of sulfation after exposure to sulfur dioxide (SO_2). As evidenced by the S(2p) data collected in Chapter III, it is clear that exposures at higher temperatures introduced greater levels of SO_2 adsorption, especially on ceria. The effects of SO_2 on zirconia-rich metal oxides was found to be negligible and will not be addressed further. On ceria, noticeable changes are noted in the Ce(3d) spectra for the most extreme set of SO_2 exposure conditions used, which are 20 ppm SO_2/N_2 at 673 K and 1000 T for 15 minutes. Figure 5.3 is a composite graph showing pre- and post-treatment spectra for ceria. Figure 5.3(a) shows the pre-treatment spectra, which is the same data as that displayed in Figure 5.2(a). The

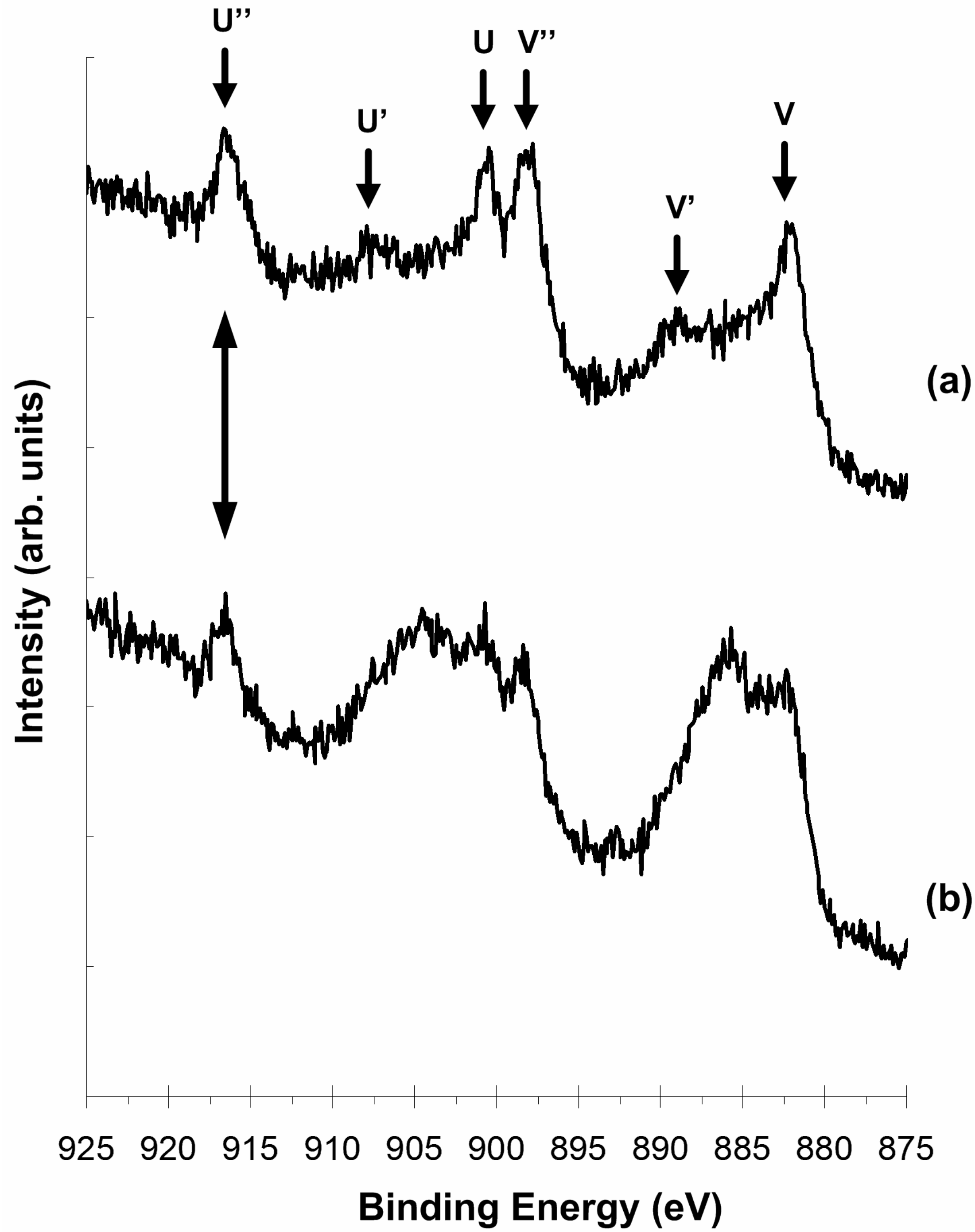

Figure 5.3 High resolution Ce(3d) XPS spectra for ceria taken (a) prior to any treatment and (b) after a 15 minute exposure to a 20 ppm SO_2/N_2 gas at 673 K and 1000 T

acquired data for ceria after a 1000 torr treatment with 20 ppm SO_2/N_2 at 673 K for 15 minutes is shown in Figure 5.3(b).

For the data collected after SO_2 treatment (Figure 5.3(b)), it is evident that some spectral changes have occurred in the Ce(3d) spectra. Most notably, the third Ce(3d) doublet's Ce($3d_{3/2}$) spin-orbit at 916 eV is still present in Figure 5.3(b), albeit at a lower intensity and peak area than that observed in the pre-treatment data. In addition, the spectral fingerprint for the other Ce(3d) signatures have undergone changes in which the Ce(3d) features take shapes increasingly more, but not completely, characteristic of cerium (III) oxide features as shown in Figure 5.2(b).

5.5 DISCUSSION

The spectral data in Figure 5.2 show that the synthesized metal oxides employed in this study are indeed fully oxidized materials. In the case of ceria, this means that the cerium atoms are in the cerium (IV) oxidation state. The condition of the ceria as synthesized is very much like what commercial ceria catalysts, as in catalytic converter wash-coats, would resemble when new. It has been demonstrated that argon ion bombardment can easily reduce the ceria surface to the cerium (III) oxidation state after only a short exposure to the flux of argon ions. After argon ion sputtering, the UHV conditions employed in the experimental apparatus prohibit the reappearance of the cerium (IV) oxide spectral features. However, exposure to some partial pressure of oxygen would reoxidize the ceria surface to cerium (IV) oxide as reported in the literature [58]. The Ce(3d) spectral shapes obtained using XPS show that this technique is highly effective in characterizing the ceria surface with respect to the most current cerium oxidation state. In addition, the UHV environment is effective in “freezing” the solid-vacuum interface from further subtle changes in oxidation state that may occur from contact with gaseous species (e.g. air). These features show that XPS is a highly effective technique in studying interactions of materials such as ceria that have some degree of flexibility in oxidation state.

The spectral data for the treatment of ceria with SO_2 reveal that under the conditions of this study, the ceria surface is undergoing partial reduction to the cerium (III) oxidation state upon exposure to SO_2 at the most sulfating conditions employed in this study. This supports the sulfur 2p XPS spectral data from Chapter III, which have been shown to consist of sulfite (SO_3) and sulfate (SO_4) species for this group of materials. Since SO_3 and SO_4 species form on the metal oxide surfaces from exposure to SO_2, it becomes clear that there must be a net transfer of oxygen to the SO_2 adsorption sites if the SO_2 is interacting with the metal centers in ceria to form SO_3 or SO_4 surface species. Therefore, in order to form SO_3 or SO_4 species from the interaction of SO_2 with cerium centers, there must be a net transfer of oxygen or hydroxyl species from surrounding metal oxide lattice or surface sites. This observation explains why there is only a partial reduction of fully oxidized ceria upon exposure to SO_2. From Chapter III and other references, it is known that SO_3 and SO_4 can also be formed by the adsorption of SO_2 on lattice oxygen sites in singly or doubly-bridged fashions [43,47-48]. There is also support in the literature for the interaction of SO_2 with metal centers in a variety of different modes [81]. Since SO_2 is classified as a cumulene ligand, it is as flexible with respect to adsorption on metal centers as it is with adsorption on lattice oxygen sites on metal oxides [81]. Reduction of some of the cerium metal centers on a ceria surface would have to take place in order for exposure to SO_2 to yield SO_3 or SO_4 surface-species on metal adsorption sites.

CHAPTER VI

PALLADIUM CZMMO PHOTOEMISSION

6.1 INTRODUCTION

Cerium and zirconium oxide are increasingly important promoter, support, and oxygen storage components in three-way catalytic converters. However, the accomplishment of the required three-way reactions would not be possible without the inclusion of a certain amount of platinum group metals [2]. Platinum, rhodium, and palladium are the three metals most commonly associated with emissions control catalysts [2]. The incorporation of these metals in many types of catalytic reactions has a long history [2,30]. Due to the scarcity and demand of these precious metals, their price has historically been high and subject to continual change [2,14,82-83]. Future technological changes in emissions control catalysis will be governed by price and supply issues related to these three metals [2]. Because of the high cost associated with this group of metals, it is important for catalyst manufacturers to disperse small amounts of these metals in conjunction with support/promoter materials for economic feasibility [2]. For first and second generation emission control catalysts, when rhodium and platinum were the predominant precious metals used in catalytic converters, typical metal loading ranges were 0.18-0.3 g and 0.9-2.3 g for rhodium and platinum, respectively [83]. At the time, this comprised 0.1-0.15% of the catalyst (by weight) [2]. For more modern third and fourth generation emissions control catalysts, precious metal content has been reduced to 0.05% by weight or lower in order to reduce the cost of production while maintaining the necessary activity [2]. In addition, fourth generation catalysts introduced the complete replacement of platinum and rhodium in most catalyst formulations with palladium technology [2]. Improvements in engine control strategies during the 1990's made possible the tight control over air-fuel stoichiometry, leading to fewer perturbations in the ratio of CO, NO_x, and hydrocarbon emissions from these engines [2]. Higher quality fuels, close-coupling of converters, and lower cost as compared to platinum and rhodium have also been key factors in making palladium the precious metal of choice for modern catalytic converters [2].

6.2 PERFORMANCE OF PALLADIUM CATALYSTS

Modern analyses of palladium-only catalyst performance show that palladium is a metal that is wholly capable of handling the emissions control requirements of modern internal combustion engines

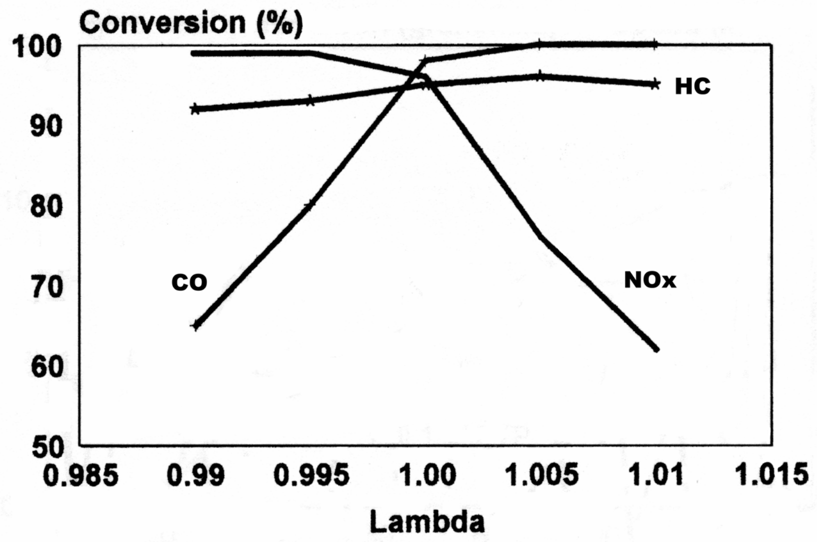

Platinum-Rhodium technology

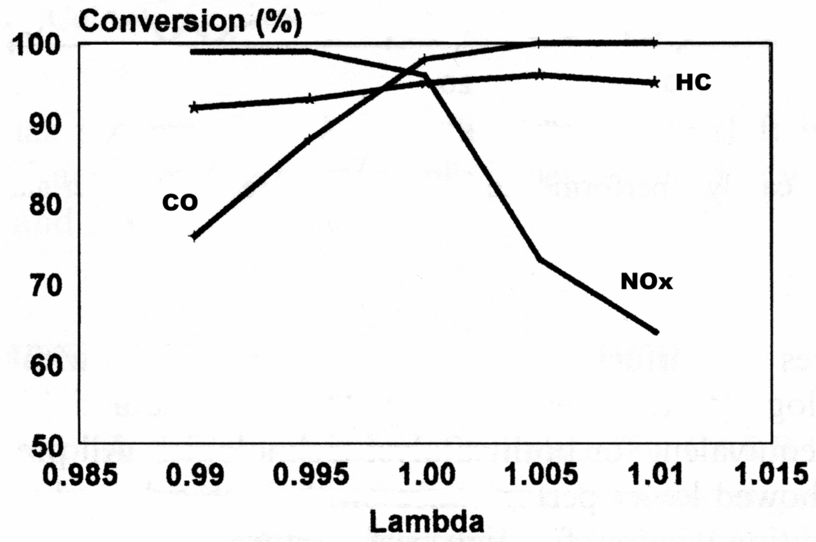

Palladium technology

Figure 6.1 Sweep test results comparing Pd-only and Pt/Rh TWC formulations for the conversion of CO, HC, and NOx emissions [2]

[2]. Figure 6.1 illustrates the results from a sweep test comparing Pt/Rh and Pd-only catalyst performance for the conversion of the three principal emissions, carbon monoxide (CO), nitrogen oxides (NO_x), and hydrocarbons (HC). The results shown in Figure 6.1 show that in that particular study, palladium containing catalysts can provide comparable benefits to emissions control as catalysts containing platinum and rhodium.

6.3 ADSORPTION OF SO_2 ON PALLADIUM CATALYSTS

There is a plethora of past research activities in regards to the fundamental interactions of palladium with various gases found in IC engine emissions [14-16,20-21,46,64,76,84-93]. In particular, there are several existing works that use photoemission studies to characterize the interaction between SO_2 and Pd model catalysts [21,46,85-86]. Most of these investigations focus on epitaxial or polished single-crystal palladium materials, but a study focusing on commercial automotive catalysts also exists [21]. The existing references have positively demonstrated the possibility of forming SO_4, SO_3, SO_2, and elemental S under the conditions employed in each respective work. However, sample preparation, photoemission system performance, and investigation conditions vary widely, so that the results need to be reviewed with care. Some sample preparation techniques, such as molecular beam epitaxy (MBE) or chemical vapor deposition (CVD), yield single crystals or thin films of metal on some substrate or support material [46,85-86]. While this type of sample preparation will provide stronger photoemission signals due to an increase in the signal-to-noise ratio, the UHV conditions in which they are kept in and formed under is not representative of the method such metals are incorporated on real catalysts. Additionally, analytical system performance can influence the quality of acquired data sets. The investigations which employ synchrotron radiation or monochromated x-ray sources have a definite energy resolution advantage compared to un-monochromated sources. In the literature, the actual experimental conditions vary widely. Some researchers have employed SO_2 exposures at cryogenic temperatures, while others expose their materials to SO_2 at elevated temperatures. Annealing treatments are also used by some investigators, adding another facet to the interpretation of the data.

6.4 MODELLING OF CERIA-ZIRCONIA SUPPORTED PALLADIUM

6.4.1 REAL PRECIOUS METAL LOADED CATALYSTS

Even though the cost of palladium is somewhat lower than that of platinum and rhodium, it still remains the most expensive commodity in the manufacture of TWC's [2]. As an active research area in catalysis, catalyst manufacturers continually research methods to minimize the amount of precious metal in their catalyst formulations without sacrificing catalyst performance. Typically, this is done by minimizing the precious metal particle size and finding ways of dispersing the particles evenly onto or within high-surface area supports such as metal oxides [30]. For the Pd-ceria-zirconia system, there are many wet chemical precursors and techniques that are known to give highly dispersed metal particles on CZMMO supports [15]. While this may be useful information for some forms of analysis, the known wet-chemical techniques are not particularly useful for photoemission studies because the impregnation of metals deep into pores places many of the precipitated metal particles below the narrow analytical volume characteristic of the XPS technique. In addition, it is extremely difficult, if not impossible, to keep surface contaminants such as carbon from hindering the quality of the surfaces produced for analysis.

The classical idea of such catalyst's functionality was that the metal had to be deposited onto the surface of a promoter oxide film (e.g. ceria), which during a previous step completely wetted the support surface (e.g. cordierite) [17]. The active catalytic sites were believed to be located at the interface between the metal and promoter materials [17]. Modern analytical techniques have helped to advance the understanding of the fundamental material morphology of such catalytic systems. HRTEM studies revealed instead, that commercial palladium-ceria catalysts have palladium and ceria particles that coexist side-by-side to each other, in close contact, but not in the superficial manner as first envisioned [17].

6.4.2 METAL-SUPPORT INTERFACIAL SITES AND SYNTHESIS

The purpose of this investigation is to study the effect of sulfur dioxide on materials with many interfacial sites between palladium metal and CZMMO materials. In order to meet this objective, the proposed materials to be studied do not represent commercial catalysts containing small amounts of highly dispersed metal particles. Instead, palladium metal particles were physically introduced to and mixed with the same CZMMO materials employed earlier in this study. The resulting mixture was then used to form wafers upon compression using a FTIR KBr pellet press at high pressures (approximately 800 MPa). In effect, the resulting sample wafers were designed to possess a large number of Pd-MMO interfacial sites that will be visible to the surface science probe (XPS) for adsorption studies employing sulfur dioxide. Since the sensitivity of XPS is on the order of 0.1 to 1 atomic percent, it is highly unlikely that XPS would detect the precious metal content in a well-dispersed commercial catalyst with a suitable signal-to-noise ratio for analysis of the interfacial areas. To counter this experimental requirement, the palladium loading for the materials employed in this investigation was set at an artificially high value of 10 mass percent Pd. This metal loading value is much higher than that used in commercial catalytic systems.

The model Pd-CZMMO catalysts were made by incorporating a fine commercial palladium powder with the appropriate amount of CZMMO powder. The mixture is lightly mixed and ground in a ceramic mortar and pestle until a uniform coloration was achieved. The commercial palladium powder employed had an average particle size of 0.25-0.55 μm (Alfa Aesar #00776). The resulting powders were then pressed into flat and thin wafers using a 13 mm FTIR potassium bromide pellet press at pressures of approximately 800 MPa. The resulting wafers were approximately 0.1 mm in thickness. The model catalyst wafers were delicate to the touch and could be fractured into smaller pieces for loading onto 1 inch OD sample platens. In general, the pieces used in this analysis were from 3 to 4 mm in diameter, which is more than sufficient since the electron spectrometer spot-size has a 0.8 mm diameter.

6.4.3 FESEM/EDX CHARACTERIZATION OF MODEL SYSTEM

Characterization was performed on a palladium-ceria wafer to investigate the morphological suitability of this material preparation method in meeting research objectives. This baseline data is used to determine the presence of palladium-MMO interfacial areas of appropriate scale and proximity. The presence of these features is important for the incorporation of these materials in the experimental plan proposed for investigating the adsorption of SO_2 on such model systems. For this purpose, a JEOL JSM-6500F field-emission scanning electron microscope (FESEM) was employed to provide visualization of morphological details found on the aforementioned palladium-ceria wafer. Concurrently, energy dispersive x-ray (EDX) spectroscopy was used to monitor the elemental composition of important morphological details captured during the acquisition of micrographs using the FESEM apparatus. Figure 6.2 shows a micrograph collected from the Pd-ceria wafer employed in this initial characterization. Under magnification, the wafer surface appeared to have regions of smooth morphology while at other areas in the immediate vicinity, the surface morphology possessed a rougher texture. In order to investigate if any differences between the different surface morphologies existed, EDX analysis was employed to gather information with respect to the constituent elements present in each type of morphology observed. Two equally-sized areas, one for each type of observed surface morphology, were chosen for area selective EDX analysis at the time the micrograph in Figure 6.2 was acquired. These areas were measured to each have an area of 0.75 μm^2, and an edge-to-edge distance of approximately 1.5 μm from each other. The resulting pair of EDX spectra are presented in Figure 6.3.

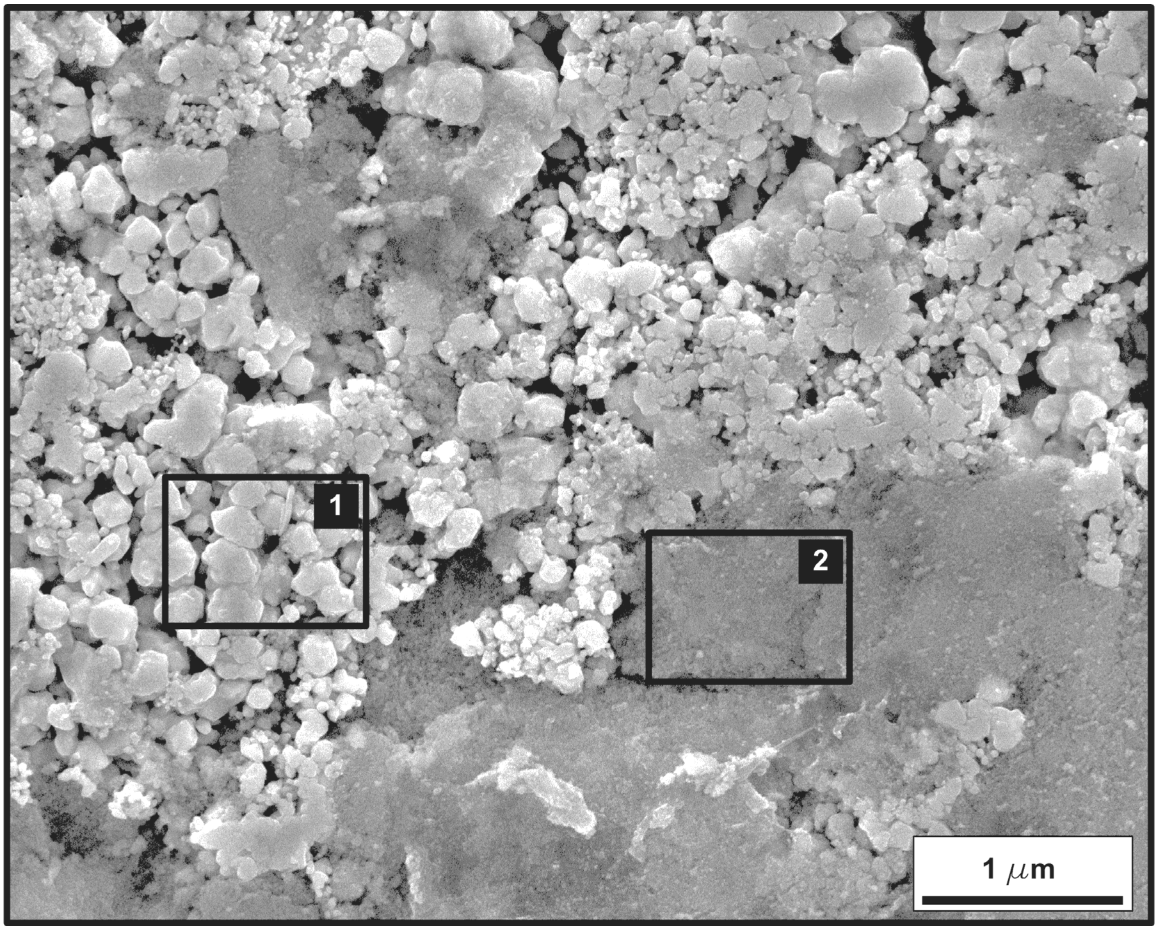

Figure 6.2 FESEM micrograph of a Pd-ceria compacted wafer of the type used in SO_2 adsorption studies (x 22,000). Rectangular areas labeled 1 and 2 were selected for EDX analysis

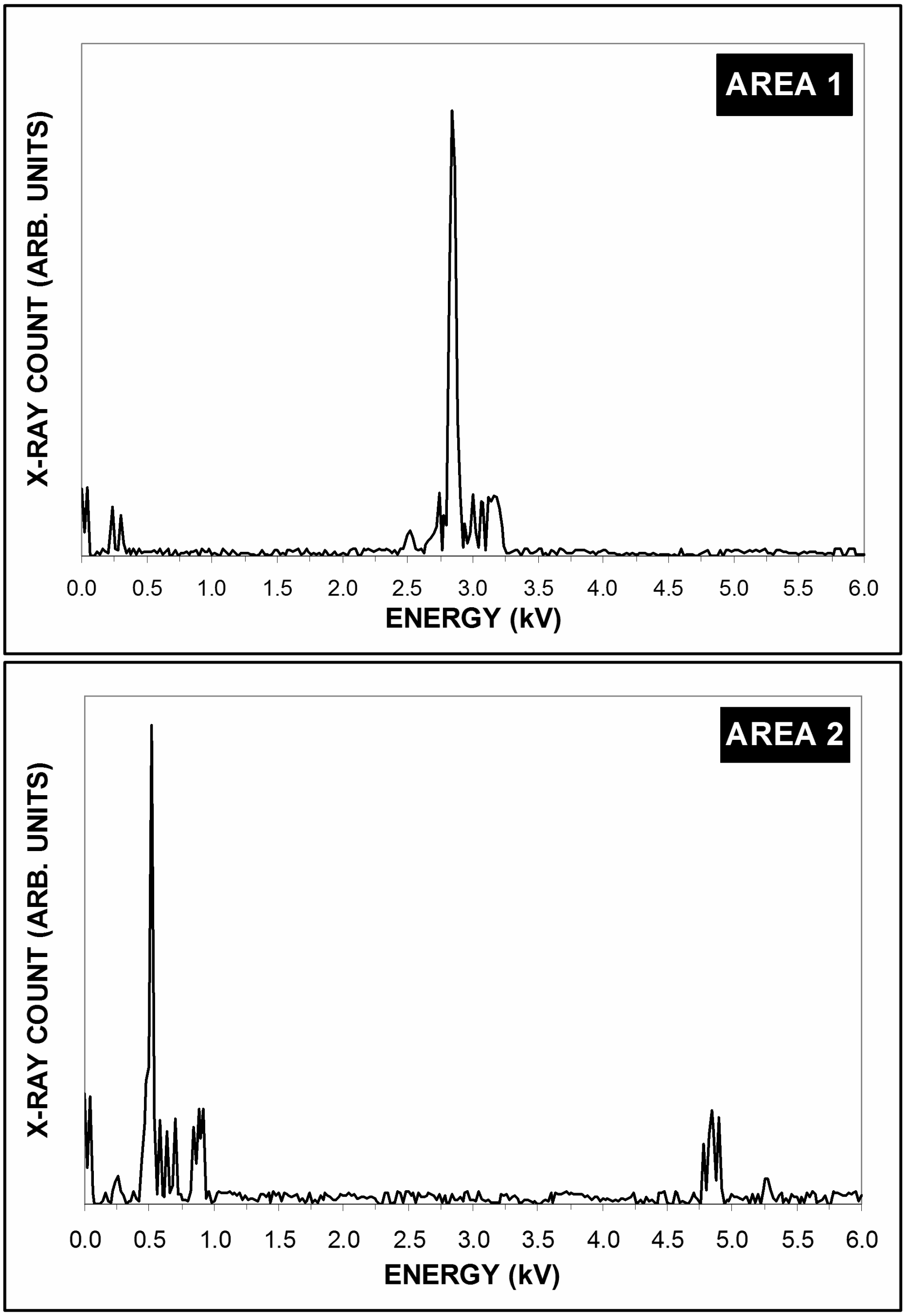

Figure 6.3 EDX spectra for two areas selected on the Pd-ceria wafer shown in Figure 6.2. This data demonstrates that Area 1, with the rough morphology, corresponds to palladium metal. Area 2, with smooth morphology, is identified as ceria

For Area 1, the EDX spectra show a strong characteristic x-ray emission at approximately 2.8 kV x-ray energy, with several much smaller x-ray emissions surrounding the strongest emission. This group of x-ray emissions is characteristic of palladium, with the strongest emission corresponding to a Pd Lα electronic transition. The smaller features correspond to weaker Pd Lβ and Lγ electronic transitions. This characteristic x-ray emission, and the lack of other emissions, is an indication that Area 1 is comprised primarily of palladium metal.

For Area 2, the EDX spectra shows a strong characteristic x-rayemission at approximately 0.5 kV x-ray energy. This strong x-ray emission corresponds to the oxygen Kα transition. Additionally, three other characteristic x-ray emissions occur at approximately 4.80, 4.85, and 4.9 kV. These emissions are attributed to cerium $L\alpha_{1,2}$, $L\beta_1$, and $L\beta_2$ electronic transitions, respectively. In addition, a weaker, but clearly distinguishable characteristic x-ray emission at 0.9 kV is due to cerium Mα and Mβ electronic transitions. From the characteristic x-ray emission evidence, it is determined that the area analyzed in Area 2 is comprised of ceria.

The FESEM and corresponding EDX data provide the necessary evidence that this material preparation method is unique and suitable for reaching the research objective. The EDX data demonstrates the abrupt interface created between pure palladium metal and metal oxide that is obtained using this technique. In addition, the electron microscopy data shows that differences in surface morphology do arise from area to area in these materials, depending on the local composition. Compressing a physical mixture of complementary-sized palladium and cerium oxide powders into wafers at high pressure is a unique method of creating a model metal-to-metal oxide interface. Since the XPS spectrometer spot size is over 5×10^5 μm^2 in area, a large number of Pd-MMO interfacial sites are available for adsorption analysis via XPS.

6.4.4 PRELIMINARY XPS CHARACTERIZATION OF MODEL SYSTEM

The intial characterization of the model Pd-MMO system via FESEM and EDX shows that this is indeed a viable method of modeling the Pd-MMO interface. Additional support for this material preparation method was sought by performing XPS characterization of model Pd-MMO wafers. Performing XPS on these materials can provide further verification that the composition in the near-surface region is representative of the desired model interface. Figures 6.4, 6.5, and 6.6 show the XPS survey and high resolution spectra for three Pd-MMO compositions, Pd-ceria, Pd-zirconia, and Pd-($Zr_{0.5}$-$Ce_{0.5}$-O_2), respectively. Figure 6.4 shows the survey scan and high resolution scans for the cerium 3d and palladium 3d spectral regions. The binding energy positions for each metal region show that cerium is fully oxidized, and

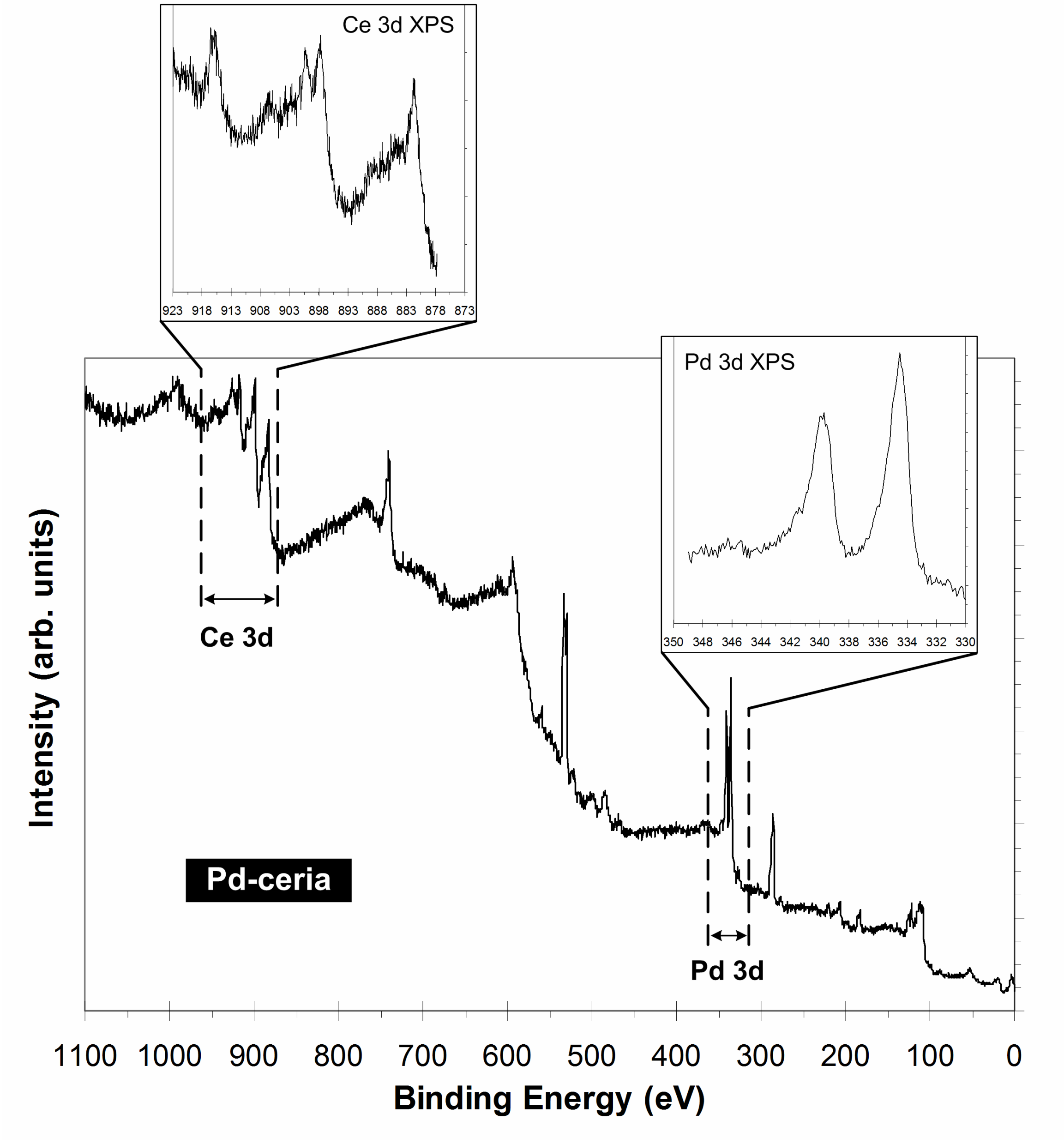

Figure 6.4 XPS survey scan for as-synthesized palladium-ceria wafer with corresponding Ce(3d) and Pd(3d) regions delineated and shown as inset XPS high resolution scans

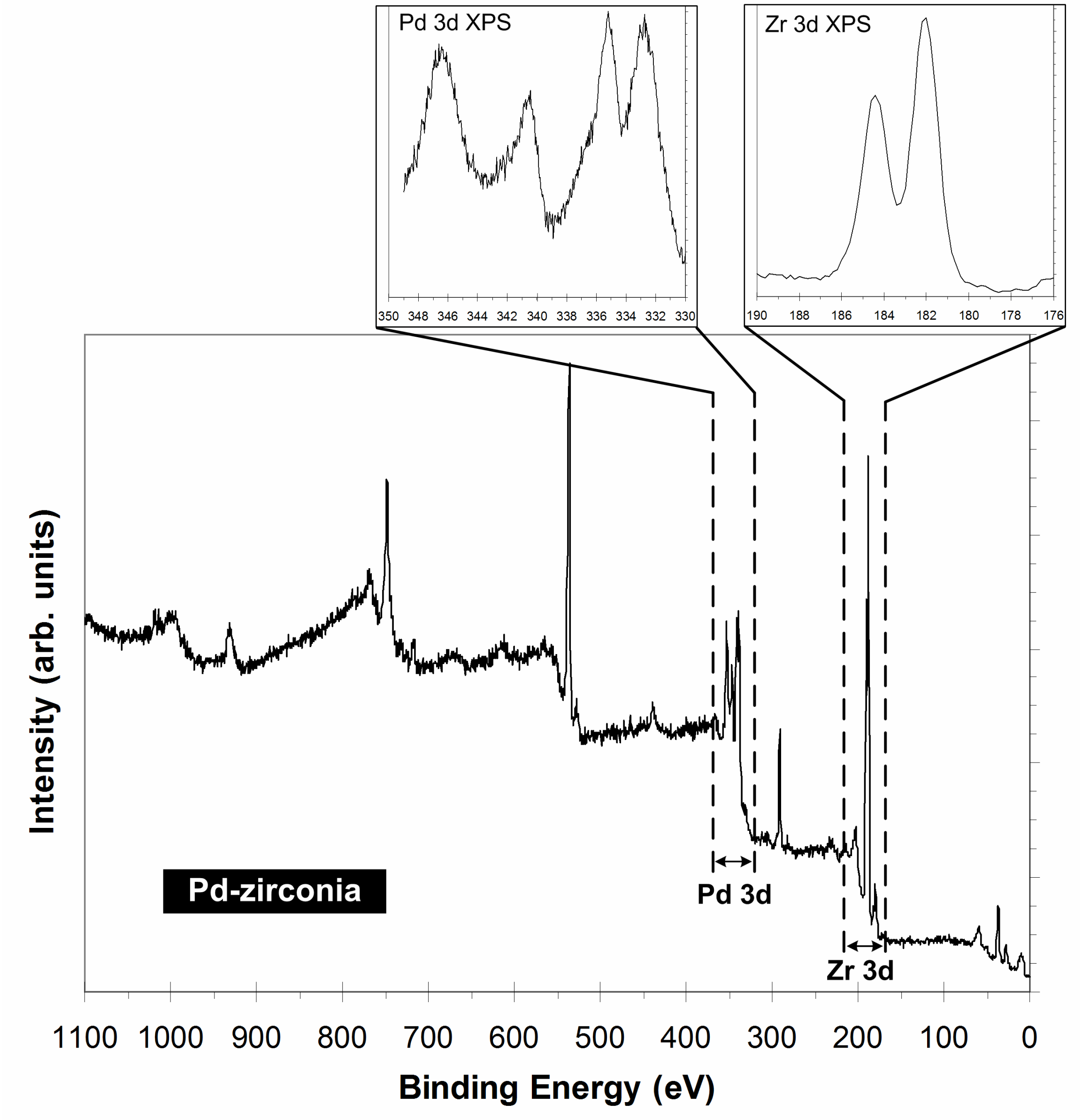

Figure 6.5 XPS survey scan for as-synthesized palladium-zirconia wafer with corresponding Zr(3d) and Pd(3d) regions delineated and shown as inset XPS high resolution scans

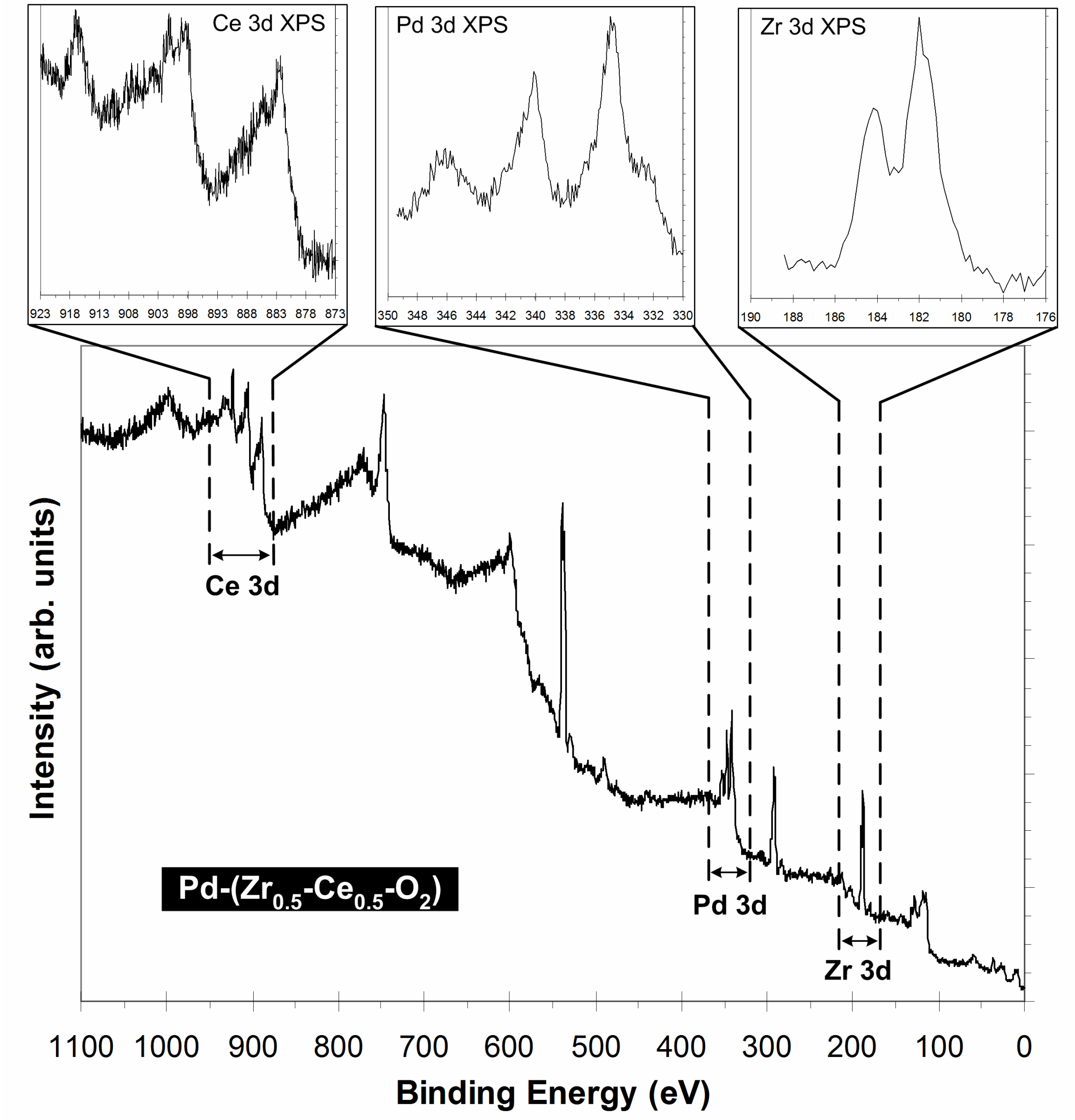

Figure 6.6 XPS survey scan for as-synthesized palladium-zirconia-ceria MMO wafer with corresponding Ce(3d), Zr(3d) and Pd(3d) regions delineated and shown as inset XPS high resolution scans

that the palladium is in the ground state. In addition, a large oxygen 1s signal is present at approximately 531 eV on the binding energy scale.

Likewise, Figure 6.5 shows that the composition in the surface region of the Pd-zirconia wafer is primarily zirconium, palladium, and oxygen. Here, the palladium 3d doublet in the high resolution spectra is more difficult to distinguish because of interference arising from the close proximity of the zirconium $3p_{1/2}$-$3p_{3/2}$ doublet to the palladium 3d signal. The Zr(3p) doublet has a difference in binding energy of 13 eV ($3p_{3/2}$ at approx. 330 eV and $3p_{1/2}$ at approx. 343 eV) [25]. The Pd(3d) doublet has a binding energy difference of 5 eV ($3d_{5/2}$ at approx. 335 eV and $3d_{3/2}$ at approx. 340 eV) [25]. So in the Pd(3d) HR spectra, the palladium doublet is observed between the zirconium 3p doublet (the palladium doublet is not fully resolved but visible as the two middle peaks). Nevertheless, the spectra demonstrate that ground-state palladium is present along with fully oxidized zirconium in this wafer.

Likewise, Figure 6.6 shows the presence of ground-state palladium in the presence of both zirconia and ceria in the only mixed-metal oxide case presented for preliminary characterization. Since the composition of each metal oxide is reduced, the corresponding cerium and zirconium signals are damped in comparison to the signals observed for the corresponding palladium and single-metal oxide cases in Figure 6.4 and 6.5.

The XPS spectra shown in Figures 6.4 through 6.6 support the qualification of this material synthesis technique as a viable Pd-MMO model for adsorption studies using SO_2. In particular, verification using XPS shows that the technique can spatially resolve the important components (Ce, Zr, O, Pd) of the model interface in the materials made using this technique.

6.5 SO_2 ADSORPTION STUDIES

6.5.1 SO_2 Exposure Conditions

The characterization of SO_2 interactions with palladium-loaded ceria-zirconia mixed-metal oxides was performed in a systematic manner. Unexposed wafers were first analyzed using XPS to check for the presence of contaminants and to obtain baseline information on all palladium, cerium, and zirconium features prior to any exposure to SO_2. Immediately following initial spectrum acquisition, the sample was translated under UHV conditions to an in-situ reaction cell. The vacuum pumps on the reaction cell were then isolated from the cell and a 20 ppm SO_2 and N_2 gas mixture was admitted into the cell until the desired pressure was reached. In this investigation, 1000 torr gas exposure pressure was employed. Reaction cell pressure was monitored simultaneously using a Phillips-Granville convectron-tube pressure gauge and a Hastings vacuum gauge. Once the desired gas pressure was attained in the reaction cell, the heating cycle was started. Approximately 15 minutes were required for the sample to reach the desired reaction temperature. Exposures were run at temperatures of 298, 473, and 673 K. Once the desired exposure time of 15 minutes had elapsed, the reaction cell was carefully evacuated and the sample allowed to cool to below 333 K before translation back into the UHV analytical chamber. In accordance with general UHV operating guidelines, a satisfactory vacuum for reintroduction into the analysis chamber (9×10^{-8} Torr) must be attained before moving the sample platen back into the analysis chamber. The evacuation, cooling, and reintroduction process lasted no longer than 1 hour. Photoemission spectra were collected as soon as feasibly possible after reintroduction to the analytical chamber.

6.5.2 Results

The observed results from this set of adsorption experiments are shown as composite high resolution spectra in Figures 6.7 and 6.8. The temperature dependency of SO_2 adsorption on these materials closely resembled that of the similar studies done using the base MMO wafers as described in Chapter III, but interesting differences arise with the addition of palladium to the MMO materials.

Figure 6.7 shows the results of the SO_2 adsorption experiments

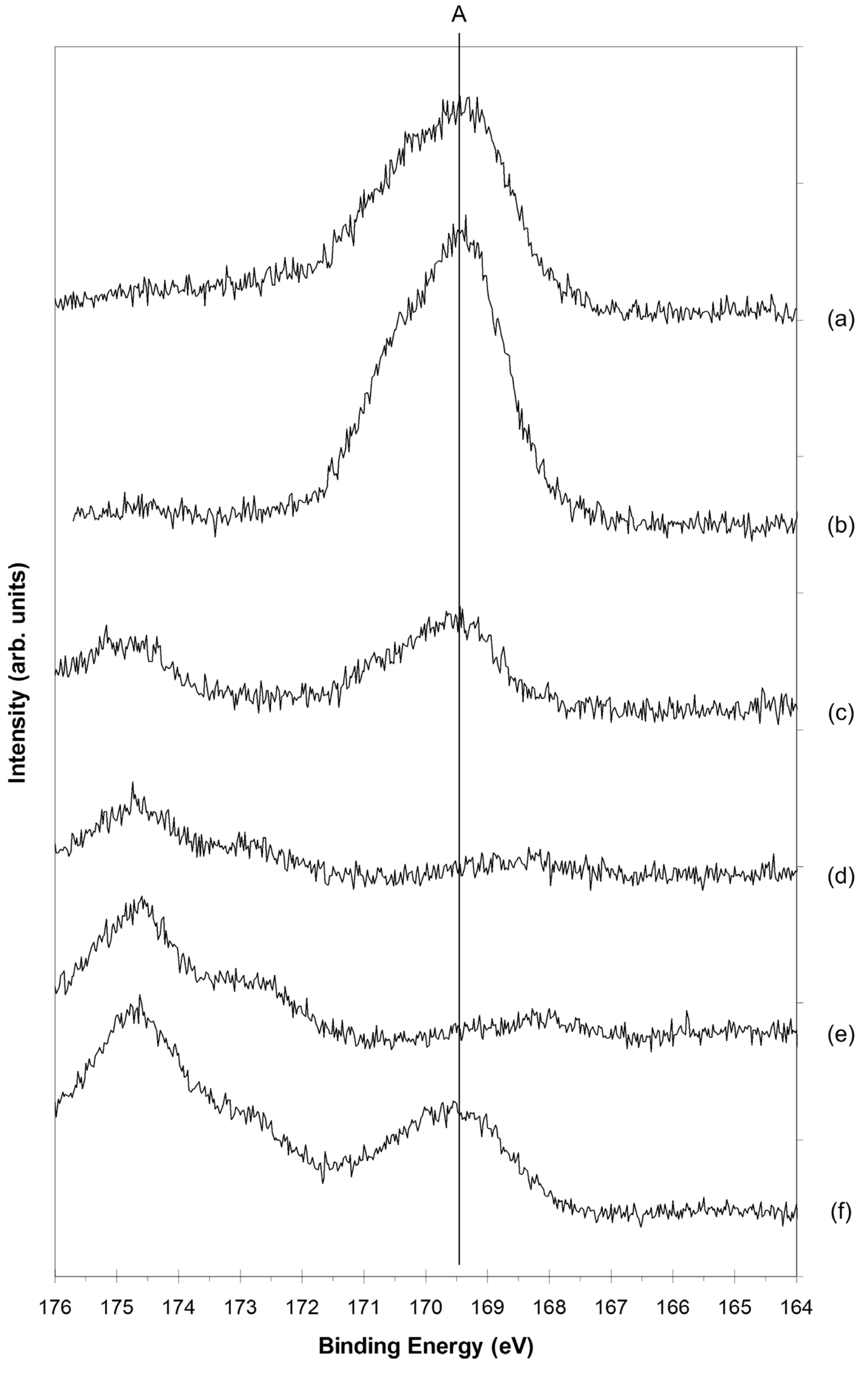

Figure 6.7 XPS spectra after SO_2 exposure at 473 K for six MMO compositions, each with a palladium loading of 10 mass% (a) Ce/Zr=1:0, (b) Ce/Zr= 9:1, (c) Ce/Zr= 7:3, (d) Ce/Zr= 5:5, (e) Ce/Zr= 2:8, (f) Ce/Zr= 0:1

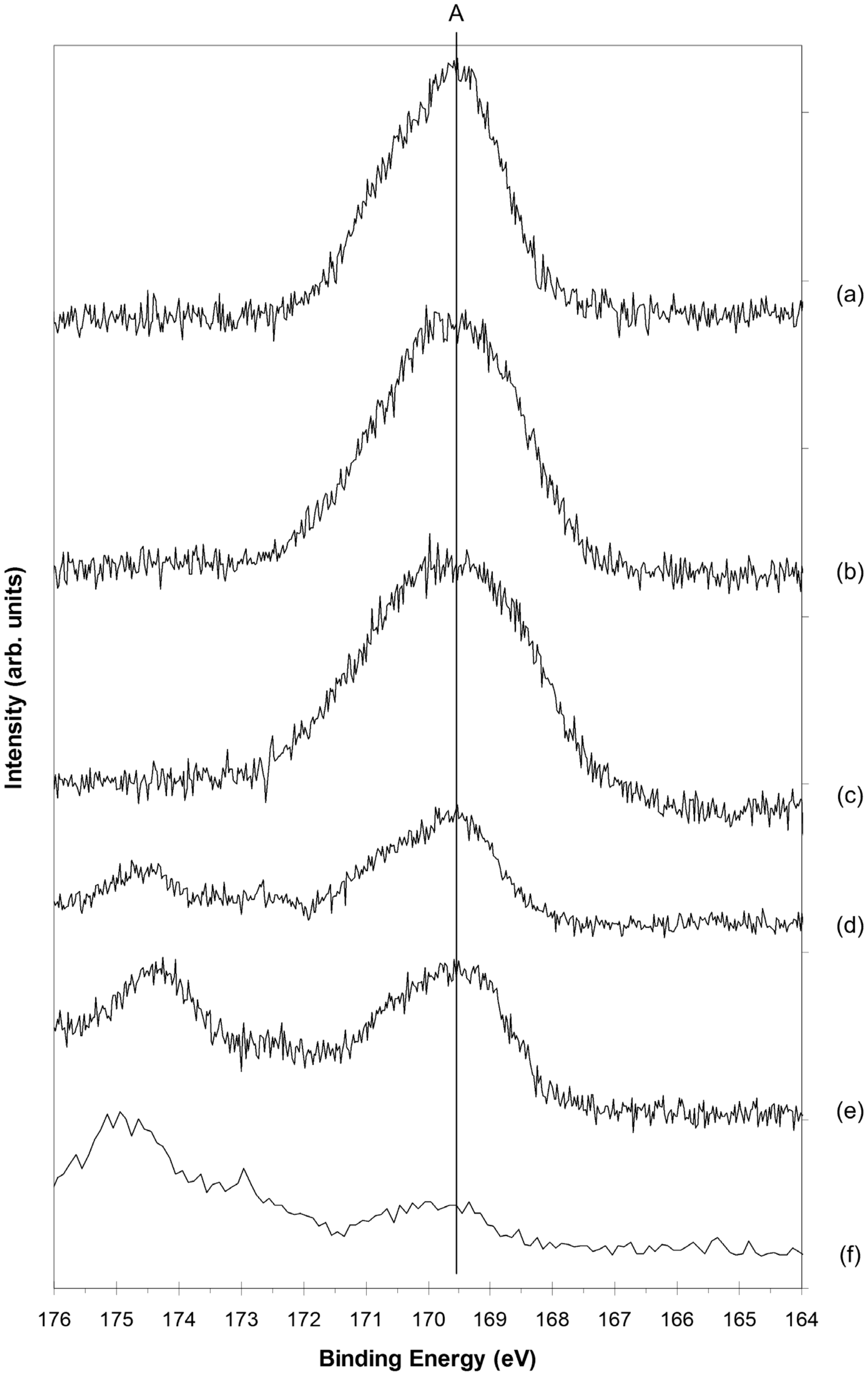

Figure 6.8 XPS spectra after SO_2 exposure at 673 K for six MMO compositions, each with a palladium loading of 10 mass% (a) Ce/Zr=1:0, (b) Ce/Zr= 9:1, (c) Ce/Zr= 7:3, (d) Ce/Zr= 5:5, (e) Ce/Zr= 2:8, (f) Ce/Zr= 0:1

that were undertaken at 473 K for the six MMO compositions used in this study. The broad and multiple lines that arise at binding energies above 172 eV in Figure 6.7 are attributed to a zirconium 3d satellite feature that lies in close proximity to the sulfur photoemission region. Spectra (a), (b), (c), (d), (e), and (f) correspond to 10 mass% palladium loaded MMO's with Ce/Zr molar ratios of 10:0, 9:1, 7:3, 5:5, 2:8, and 0:10, respectively. Of principal interest in this investigation is the S(2p) photoemission that occurs at approximately 169.5 eV binding energy. These features are labeled "A" in the figure, and have a vertical line to demonstrate the features' relative position to neighboring spectra. These S(2p) features are in excellent agreement with previously obtained binding energies, peak widths, and peak symmetries on base MMO wafers. This data indicates that the formation of sulfate (SO_4) and sulfite (SO_3) surface species is taking place. However, an interesting difference is present for the palladium-loaded 5:5 and 2:8 Ce/Zr molar ratio MMO materials. In Chapter III, it was shown that the adsorption of SO_2 is a strong function of temperature, but also of composition. In particular, as the composition becomes increasingly rich in ceria, it was shown that the propensity for SO_2 adsorption increases in a positive manner. However, this is not the same under the conditions of this investigation for the case of these palladium-loaded MMO materials. The palladium-loaded zirconia, at 473 K, shows a larger propensity for SO_2 adsorption than the

2:8 and even 5:5 Ce/Zr MMO materials. However, as the cerium content in the MMO increases past the 5:5 Ce/Zr MMO, the S(2p) signal increases at a rapid rate with increasing Ce/Zr ratio.

Similarly, Figure 6.8 shows the results obtained for the same compositions exposed to SO_2, except at 673 K. These spectral data show that the adsorption of SO_2 is also a function of temperature. The spectral data in Figure 6.8 is labeled using the same convention employed in Figure 6.7. Here, it is interesting to note the substantial increase in S(2p) signal for the 2:8 and 5:5 Ce/Zr MMO's in comparison to the spectra collected at 473 K. In addition, the 7:3 Ce/Zr composition experiences a large increase in S(2p) peak intensity as compared to the data taken after exposure at 473 K. The compositions that are rich in ceria, specifically, the 10:0 and 9:1 Ce/Zr compositions, show fairly stable S(2p) lines at the 473 K and 673 K exposure conditions.

Unfortunately, only a limited visual confirmation can be garnered from the compilation of composite spectra. The vertical scales for each spectrum are equal, so that small differences in signal amplitude may not be visible. Gathering the S(2p) peak area for each experiment provides a more quantitative comparison between the individual spectra. Figure 6.9 is a composite graph showing the normalized S(2p) peak area as a function of MMO composition. In addition to the palladium-loaded materials, the base MMO S(2p) peak areas collected in Chapter III are

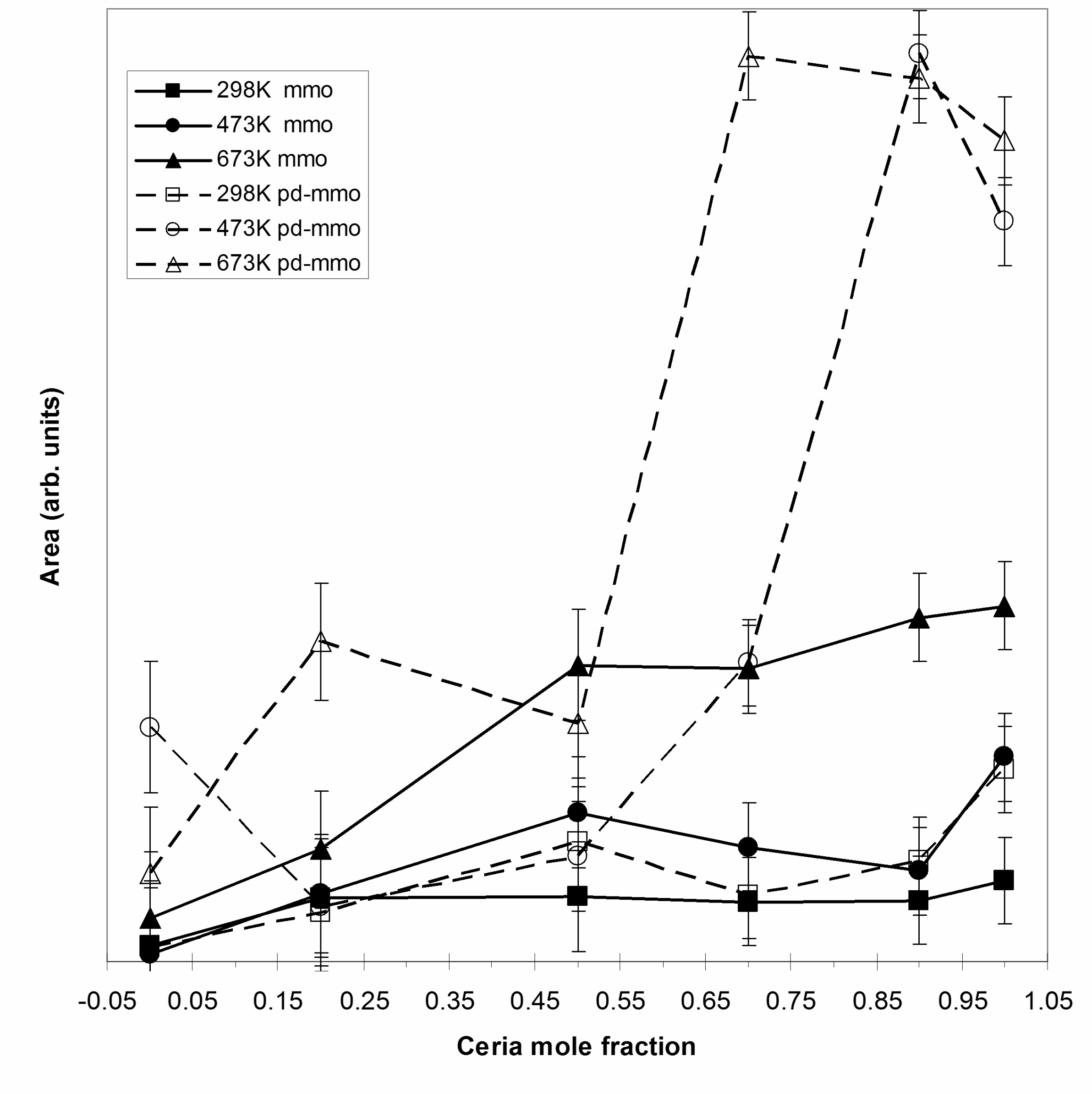

Figure 6.9 Compilation of S(2p) peak areas obtained using high resolution XPS after a 15 min SO_2 exposure at 1000 T for six MMO compositions (x-axis). Solid lines and filled symbols denote the results obtained for base MMO's while dashed lines and hollow symbols represent MMO's loaded with 10 mass% palladium

shown with solid lines and filled in symbols for direct comparison with the results using the palladium-loaded MMO's. The palladium loaded MMO results are shown with dashed lines and hollow symbols. The data in Figure 6.9 shows in a more comparative manner the size of the increase in S(2p) peak area as the composition becomes rich in ceria. In particular, for exposure at 473 K, the 10:0 (ceria) and 9:1 compositions show very significant gains in S(2p) peak area as compared to the results obtained for the corresponding base MMO wafers. Similarly, at 673 K, the same compositions show very similar gains over the base MMO results, along with the palladium loaded 7:3 Ce/Zr MMO, which is the next cerium-rich composition to be investigated. The significant rise in S(2p) peak area in these cases is two or three times the values obtained for the base MMO materials exposed to SO_2 at equivalent conditions. Figure 6.9 also shows that the S(2p) signatures are not absent in the data presented in Figure 6.7 for the 2:8 and 5:5 Ce/Zr materials, but are actually on the order of the S(2p) signals obtained when investigating the base MMO materials of equal composition. The vertical scale in Figures 6.7 and 6.8 is dictated by the strong S(2p) photoemission counts observed for the 10:0 and 9:1 MMO compositions at 473 K and additionally, the 7:3 MMO composition at 673 K. Since these photoemissions are two to three times as intense as the most intense

S(2p) signal obtained for the base MMO's, the weaker S(2p) signals are not distinguishable on this vertical scale. However, individual spectrum analysis has revealed that the S(2p) signal is present, just at a much lower intensity level.

Examination of the Pd(3d) high resolution spectra have shown that there is no change in palladium oxidation state and the palladium is essentially zero valent.

6.6 DISCUSSION

The results shown in the previous section demonstrate that the incorporation of palladium in these mixed-metal oxides does impart certain effects to the adsorption of SO_2 on these particular materials. The compositional and exposure temperature trends visible in study of SO_2 adsorption on the base MMO materials is not seen in the same way with the palladium-loaded MMO's. However, the binding energy and width of the observed S(2p) features is fully consistent with those previously reported for the formation of sulfite (SO_3) and sulfate (SO_4) species on base MMO materials. Nevertheless, several interesting features are present in the data acquired for the palladium-loaded MMO materials.

Firstly, the signal intensity at certain conditions is of significantly higher value than previously observed. In particular, at 473 K exposure conditions, the palladium-loaded materials with Ce/Zr molar ratios of 10:0 and 9:1 show between two and three times the signal intensity of the most intense S(2p) signal observed for the base MMO materials. At an even higher temperature of 673 K, similar S(2p) signal intensity changes are observed for the 7:3 Ce/Zr material, which is incrementally, the material with the next lower molar ratio of cerium. Very steep drops in the S(2p) signal occur as the cerium molar ratio is decreased further.

Another interesting observation is the apparent decrease in S(2p) signal intensity as the composition becomes pure ceria at elevated temperature. This drop in S(2p) signal from the 9:1 to 10:0 Ce/Zr composition can be attributed to enhanced availability of oxygen in the wafers due to a small amount of zirconia. The ability of zirconia to conduct oxygen anions is a well known phenomena [2]. Here, the presence of a small amount of zirconia could render increased oxygen mobility in the crystalline lattice while maintaining or increasing the number of SO_2 adsorption sites on ceria.

Undoubtedly, a substantial increase in adsorption sites along with enhanced oxygen mobility in the crystalline lattice is required for such increases in signal intensity to be realized. For SO_2 to adsorb onto and form sulfite/sulfate compounds on a zero valent metal, such as palladium, oxygen would have to be present and mobile to allow the formation of such compounds. In these cases, a small amount of zirconia in a ceria-zirconia solid solution could make possible the conduction of easily removed oxygen atoms from the ceria lattice to an oxygen deficient area, such as a nearby ground state palladium surface. Reduction of ceria to the (III) oxidation state would then occur at deeper levels, eventually resulting in hindered oxygen availability.

At lower temperatures, such as 298 K, the palladium-loaded materials displayed slight increases in S(2p) adsorption intensities obtained for the base MMO materials at 298 K. These increases can be attributed to the formation of sulfite and sulfate compounds on additional adsorption sites on the metal oxide provided by the addition of palladium metal particles.

However, for the zirconia-rich materials, the S(2p) signal intensities never surpass the most intense S(2p) signal obtained for the base oxides (ceria at 673 K). The addition of palladium to the zirconia-rich MMO's does give an increase in S(2p) signal. This is due to the addition of palladium, which provides more adsorption sites compared to the base metal oxide.

For most compositions, the addition of palladium to the MMO materials results in increased SO_2 adsorption to some extent. Since the palladium is not experiencing oxidation state change, the adsorption of sulfur dioxide must be occurring at MMO surface sites. However, at elevated temperatures, the palladium may be contributing to the S(2p) signals for some compositions by itself becoming oxidized at deeper levels and mechanistically releasing the additional oxygen atoms for the formation of sulfite and sulfate surface species at nearby oxide surface sites. These sites can then become active adsorption sites due to the availability of additional oxygen. In effect, the palladium may be serving to reoxidize cerium (III) oxide sites and allow further formation of sulfite and sulfate species.

These results show that for certain combinations of compositions and exposure conditions, the tendency for adsorption of SO_2 can be significant on ceria and zirconia-based catalysts. The beneficial catalytic properties of catalysts must be applied carefully with consideration given to potential catalyst poisons.

CHAPTER VII

CONCLUSIONS

- Sulfate and sulfite surface species form upon exposing ceria-zirconia mixed-metal oxides to a sulfur dioxide and nitrogen gas mixture.
- The adsorption of sulfur dioxide is temperature dependent at any oxide composition, with a larger propensity for adsorption at higher temperatures.
- Compositional dependence is displayed, with samples having higher ceria mole fractions showing a larger propensity for adsorption of sulfur dioxide than those samples composed primarily of zirconia.
- Adsorption sites must consist of residual surface hydroxyl groups and lattice oxygen atoms.
- Zirconia is resistant to sulfur dioxide adsorption under the conditions of this study and does not undergo changes in oxidation state.

- In ceria, surface residing cerium atoms undergo partial reduction from Ce(IV) to Ce(III) upon exposure to sulfur dioxide, especially at elevated temperatures.
- The reduction of fully oxidized ceria to reduced cerium (III) oxide is attributed to the net loss of oxide oxygen for the subsequent formation of sulfite and sulfate sulfur species.
- Palladium loading affects sulfur dioxide adsorption on zirconia-rich MMO's.
- Palladium loaded MMO's that are rich in ceria show a sharp increase in sulfur dioxide adsorption of two or three times greater intensity than comparably treated base MMO's.
- The addition of palladium does not alter the sulfur speciation witnessed in base MMO studies.
- Lack of changes in the Pd 3d XPS spectra show that palladium does not undergo changes in oxidation state from exposure to sulfur dioxide.
- Ceria-palladium interfacial regions are particularly susceptible to adsorption of sulfur dioxide under the conditions of this study.

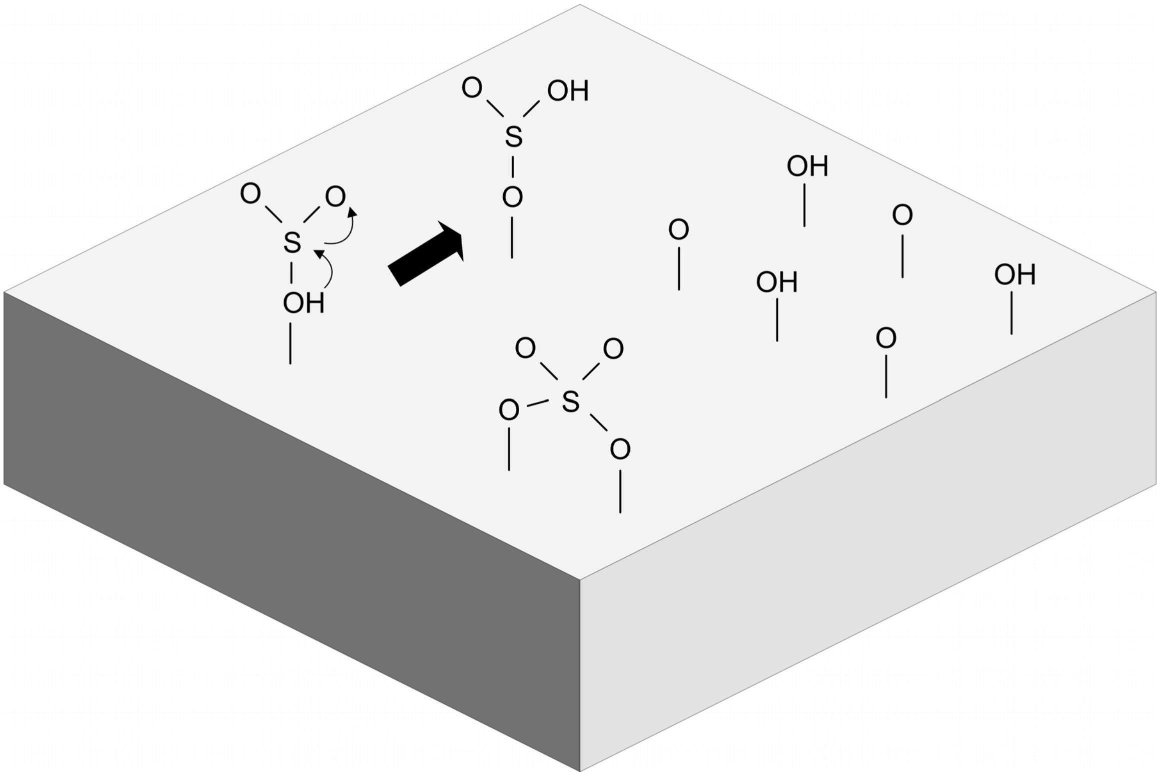

Figure 7.1 Graphic showing the formation of singly-coordinated hydrogen sulfite species and doubly-bridged sulfate species on the partially hydroxylated surface of ceria/zirconia

CHAPTER VIII

RECOMMENDATIONS FOR FUTURE RESEARCH

There are many opportunities for enhancing the knowledge-base of catalytic system deactivation. Exploration using new materials can possibly produce new research objectives. In addition to exploring new materials, it is imperative to try alternative experimental protocols and techniques to gain a more complete understanding of known phenomena.

The exposure of a catalyst to sulfur dioxide after the catalyst is first exposed to other carbon or nitrogen gas species can show interesting deactivation phenomena. As an automotive catalyst, the material will be primarily subjected to carbon monoxide and carbon dioxide environments under most conditions. The combined effect of controlled sulfur dioxide exposure on a catalyst surface that already has some form of adsorbed carbonaceous species present is unknown, but a very practical phenomena to investigate.

Likewise, oxidizing treatments at realistic temperatures under an oxygen or nitrogen oxide environment, after SO_2 adsorption may show whether the nature of sulfur dioxide adsorption on these materials is irreversible. This would further solidify the understanding of the known deactivation process in commercial catalysts.

In addition, spectroscopic studies focusing on the effect of water vapor on metal oxide catalysts in high temperature exhaust streams would shed light on the regeneration of Brönsted acid sites that have been observed and/or consumed on these metal oxides. Performing multiple heated treatments of sulfur dioxide followed by water vapor, in a cyclic fashion, could provide additional insight into this phenomena. Since water vapor is also a major IC engine exhaust component, a study focusing on cyclic exposures to water and sulfur dioxide would benefit the knowledgebase.

The exposure conditions employed could be further expanded to include very high temperature regimes. The temperatures employed in this study reached 673 K, but the actual temperature a commercial catalyst may experience can reach 1273 K under some driving conditions. Unfortunately, performing exposures at these temperatures can prove to be a challenge for any analytical in-situ heating system in which an unshielded stainless steel platen is used to support a polycrystalline catalyst wafer. Simple equipment upgrades to the heating system and sample manipulation methods could make such studies a real possibility.

Another recommendation for future studies is to employ additional techniques. One promising route is to try a vibrational spectroscopy such as Raman or FTIR spectroscopy. This tool is extremely powerful in the elucidation of chemical structures, and could only serve to reinforce the findings obtained using other techniques. Secondary ion mass spectroscopy (SIMS) is another technique that would provide a unique viewpoint of the species created by sulfur dioxide adsorption. However, it is necessary to emphasize the importance for in-situ studies regardless of the analytical technique employed.

Futher material development can lead to major advancements in emissions control catalyst development. Finding a new material, or combination of materials, that possesses unique oxygen storage capabilities while demonstrating strong resistance to deactivation by various poisons would be a significant achievement in catalytic science. In order to do this, studies would have to be undertaken to measure the oxygen storage and catalytic properties of a material while simultaneously investigating the adsorption of known poisons such as SO_2. Possible materials to explore can include some lesser-known metal oxides or other synthetically derived high surface area silica or metal oxides. In particular, synthetically derived metal oxides that are made using micellar templating routes can yield metal oxides that are more highly porous than equivalently composed materials derived using other, more common methods. These methods have yielded materials that are extremely high in surface area and are currently the subject of intense research in the catalysis community. Utilizing commercial catalysts and teaming with a commercial catalyst manufacturer that is involved in materials research may be a promising route to finding new catalyst material prospects. If a synergistic relationship could be fostered between commercial and academic research units, the results from such collaboration could be significant. Due to the highly proprietary nature of these materials, proposing joint research ventures to catalyst manufacturers would be a challenge. However, the opportunity for collaboration with industry does exist. The proposed work would have to be sold by the principal investigator in a convincing manner while showing significant practical knowledge and understanding of the problems currently facing industrial catalysts.

REFERENCES

[1]. U.S. Environmental Protection Agency, The Plain English Guide to the Clean Air Act, EPA-400-K-93-001 (1993).

[2]. R.M. Heck, R.J. Farrauto, S.T. Gulati, *Catalytic Air Pollution Control: Commercial Technology,* John Wiley and Sons, Inc., New York (2002).

[3]. U.S. Environmental Protection Agency, EPA Staff Paper on Gasoline Sulfur Issues, EPA-420-R-98-005 (1998).

[4]. U.S. Environmental Protection Agency, Latest Findings on National Air Quality: 2002 Status and Trends, EPA-454-K-03-001 (2003).

[5]. U.S. Environmental Protection Agency, EPA's Program for Cleaner Vehicles and Cleaner Gasoline, EPA-420-F-99-051 (1999).

[6]. Chevron Products Company, Motor Gasolines Technical Review, FTR-1 (1996).

[7]. J.G. Calvert, J.B. Heywood, R.F. Sawyer, J.H. Seinfeld, Science, 261 (1993) 37.

[8]. K.R. Laud, E.M. Logothetis, K. Park, U.S. Patent No. 3,933,028, (1976).

[9]. H. Furuhashi, S. Tanida, T. Saito, U.S. Patent No. 5,518,603, (1996).

[10]. Chevron Products Company, Aviation Fuels Technical Review, FTR-3 (2000).

[11]. Chevron Products Company, Diesel Fuels Technical Review, FTR-2 (1998).

[12]. J.T. Kummer, Prog. Energy Combust. Sci., 6 (1980) 177.

[13]. British Petroleum Company, BP Statistical Review of World Energy, (2003).

[14]. K.C. Taylor, Catal. Rev. – Sci. Eng., 35 (1993) 457.

[15]. A. Trovarelli, *Catalysis by Ceria and Related Materials,* Imperial College Press, London (2002).

[16]. H.W. Jen, G.W. Graham, W. Chun, R.W. McCabe, J.P. Cuif, S.E. Deutsch, O. Touret, Catal. Today, 50 (1999) 309.

[17]. B. Fultz, J.M. Howe, *Transmission Electron Microscopy and Diffractometry of Materials,* Springer-Verlag, New York (2002).

[18]. Alfa-Aesar, 2004 General Catalog.

[19]. Y. Zel'dovich, Acta Physicochimica U.R.S.S., 21 (1946) 577.

[20]. K.C. Taylor, Ind. Eng. Chem., Prod. Res. Dev., 15 (1976) 264.

[21]. D.D. Beck, M.H. Krueger, D.R. Monroe, SAE Technical Paper Series, Preprint 910844 (1991).

[22]. A.E. Nelson, K.H. Schulz, Appl. Surf. Sci., 210 (2003) 206.

[23]. C.E. Hori, H. Permana, K.Y. Simon Ng, A. Brenner, K. More, K.M. Rahmoeller, D. Belton, Appl. Cat. B: Env., 16 (1998) 105.

[24]. C.E. Hori, A. Brenner, K.Y. Simon Ng, K.M. Rahmoeller, D. Belton, Catal. Today, 50 (1999) 299.

[25]. J.F. Moulder, W.F. Stickle, P.E. Sobol, K.D. Bomben, *Handbook of X-ray Photoelectron Spectroscopy*, Perkin-Elmer Corporation, Eden Prairie, 1992.

[26]. J.F. O'Hanlon, *A User's Guide to Vacuum Technology,* John Wiley and Sons, Inc., New York (1980).

[27]. S. Tanuma, D.R. Penn, Surf. Interface Anal., 17 (1991) 911.

[28]. P. Atkins, *Physical Chemistry,* W.H. Freeman and Company, New York (1994).

[29]. P.E.J. Flewitt, R.K. Wild, *Physical Methods for Materials Characterisation,* Institute of Physics Publishing, Philadelphia (1994).

[30]. B.C. Gates, *Catalytic Chemistry,* John Wiley and Sons, Inc., New York (1992).

[31]. V.E. Henrich and P.A. Cox, *The Surface Science of Metal Oxides,* Cambridge University Press, New York (1994).

[32]. R. A. Campbell and D. W. Goodman, Rev. Sci. Instrum., 63 (1992) 172.

[33]. E. T. Krastev and R. G. Tobin, J. Vac. Sci. Technol. A, 16 (1998) 743.

[34]. A. Ludviksson, J. Yoshihara, and C. T. Campbell, Rev. Sci. Instrum., 66 (1995) 4370.

[35]. S. Thevuthasan, D. R. Baer, M. H. Engelhard, Y. Liang, J. N. Worthington, T. R. Howard, J. R. Munn, and K. S. Rounds, J. Vac. Sci. Technol. B, 13 (1995) 1900.

[36]. Y. N. Wang, R. McAllister, R. G. Herman, G. W. Simmons, and K. Klier, Rev. Sci. Instrum., 63 (1992) 5767.

[37]. J. Szanyi and D. W. Goodman, Rev. Sci. Instrum., 64 (1993) 2350.

[38]. T. A. Jachimowski and J. Lauterbach, Rev. Sci. Instrum., 69 (1998) 2757.

[39]. K. E. Keck, B. Kasemo, and A. Höglund, Rev. Sci. Instrum., 54 (1983) 574.

[40]. A. E. Nelson and K. H. Schulz, Rev. Sci. Instrum., 71 (2000) 2471.

[41]. C.D. Wagner, Applied Surface Analysis, ASTM STP 699 (1980) 137.

[42]. A.E. Nelson, K.H. Schulz, Stud. Surf. Sci. Catal., 139 (2001) 247.

[43]. S.H. Overbury, D.R. Mullins, D.R. Huntley, L. Kundakovic, J. Phys. Chem. B, 103 (1999) 11308.

[44]. D.D. Beck, M.H. Krueger, D.R. Monroe, SAE Paper No. 910844, 1991.

[45]. J.A. Rodriguez, T. Jirsak, A. Freitag, J.C. Hanson, J.Z. Larese, S. Chaturvedi, Catal. Lett., 62 (1999) 113.

[46]. R.M. Ferrizz, R.J. Gorte, J.M. Vohs, Catal. Lett., 82 (2002) 123.

[47]. M. Waqif, A.M. Saad, M. Bensitel, J. Bacheller, O. Saur, J.C. Lavalley, J. Chem. Soc., Faraday Trans., 88 (1992) 2931.

[48]. M. Waqif, P. Bazin, O. Saur, J.C. Lavalley, G. Blanchard, O. Touret, Appl. Cat. B Env., 11 (1997) 193.

[49]. A. Badri, C. Binet, J.C. Lavalley, J. Chem. Soc., Faraday Trans., 92 (1996) 4669.

[50]. J.L. d'Itri, V.V. Pushkarev, V.I. Kovalchuk, AIChE Annual Meeting, paper 506d, San Francisco, CA (2003).

[51]. A. Trovarelli, Catal. Rev.- Sci. Eng., 38 (1996) 439.

[52]. H. Luth, *Solid Surfaces, Interfaces and Thin Films,* Springer-Verlag, New York (2001).

[53]. S. Shah, *Surface and Interface Characterization in Corrosion,* NACE International, Houston (1994).

[54]. A. Corma, H. Garcia, Catal. Today, 38 (1997) 257.

[55]. M. Hunger, S. Ernst, S. Steuernagel, J. Weitkamp, Microporous Materials, 6 (1996) 349.

[56]. A. Corma, Chem. Rev., 95 (1995) 559.

[57]. D.M. Lyons, J.P. McGrath, M.A. Morris, J. Phys. Chem. B, 107 (2003) 4607.

[58]. D.R. Mullins, S.H. Overbury, D.R. Huntley, Surf. Sci., 409 (1998) 307.

[59]. D.N. Belton, S.J. Schmieg, J. Vac. Sci. Technol. A, 11 (1993) 2330.

[60]. A. Galtayries, R. Sporken, J. Riga, G. Blanchard, R. Caudano, J. Electron Spectrosc. Relat. Phenom., 88-91 (1998) 951.

[61]. C. Hardacre, G.M. Roe, R.M. Lambert, Surf. Sci., 326 (1995) 1.

[62]. B.E. Koel, G. Praline, H.I. Lee, J.M. White, R.L. Hance, J. Electron Spectrosc. Relat. Phenom., 21 (1980) 31.

[63]. G. Praline, B.E. Koel, R.L. Hance, H.I. Lee, J.M. White, J. Electron Spectrosc. Relat. Phenom., 21 (1980) 17.

[64]. D.D. Beck, J.W. Sommers, C.L. DiMaggio, Appl. Catal. B: Env., 11 (1997) 273.

[65]. K. Tatsumi, M. Tsutsui, J. Electron Spectrosc. Relat. Phenom., 16 (1979) 113.

[66]. J.Z. Shyu, W.H. Weber, H.S. Gandhi, J. Phys. Chem., 92 (1988) 4964.

[67]. A. Pfau, K.D. Schierbaum, W. Göpel, Surf. Sci., 331-333 (1995) 1479.

[68]. A. Pfau, K.D. Schierbaum, Surf. Sci., 321 (1994) 71.

[69]. P. Burroughs, A. Hamnett, A.F. Orchard, G. Thornton, J. Chem. Soc., Dalton Trans., 17 (1976) 1686.

[70]. G.W. Graham, C.L. Roe, L.P. Haack, A.M. Straccia, J. Vac. Sci. Technol. A, 18 (2000) 1093.

[71]. Y. Baer, C. Zürcher, Phys. Rev. Lett., 39 (1977) 956.

[72]. A.J. Signorelli, R.G. Hayes, Phys. Rev. B, 8 (1973) 81.

[73]. E. Paparazzo, G.M. Ingo, N. Zacchetti, J. Vac. Sci. Technol. A, 9 (1991) 1416.

[74]. J. Stubenrauch, J.M. Vohs, J. Catal., 159 (1996) 50.

[75]. E.S. Putna, R.J. Gorte, J.M. Vohs, G.W. Graham, J. Catal., 178 (1998) 598.

[76]. A. Tschöpe, W. Liu, M. Flytzani-Stephanopoulos, J.Y. Ying, J. Catal., 157 (1995) 42.

[77]. M. Romeo, K. Bak, J. El Fallah, F. Le Normand, L. Hilaire, Surf. Interface Anal., 20 (1993) 508.

[78]. E. Wuilloud, B. Delley, W.D. Schneider, Y. Baer, Phys. Rev. Lett., 53 (1984) 202.

[79]. O. Gunnarsson, K. Schönhammer, Phys. Rev. B, 28 (1983) 4315.

[80]. A. Kotani, T. Jo, J.C. Parlebas, Adv. Phys., 37 (1988) 37.

[81]. M.R. Albert, J.T. Yates, Jr., *The Surface Scientist's Guide to Organometallic Chemistry,* American Chemical Society, Washington, DC (1987).

[82]. B.J. Cooper, Plat. Met. Rev., 38 (1994) 2.

[83]. J.R. Anderson, M. Boudart, *Catalysis: Science and Technology,* Springer-Verlag, New York (1984).

[84]. D.D. Beck, J.W. Sommers, Appl. Catal. B: Env., 6 (1995) 185.

[85]. J.A. Rodriguez, T. Jirsak, S. Chaturvedi, J. Chem. Phys., 110 (1999) 3138.

[86]. G. Liu, J.A. Rodriguez, Z. Chang, J. Hrbek, J. Phys. Chem. B, 108 (2004) 2931.

[87]. P. Albers, J. Pietsch, S.F. Parker, J. Molec. Catal. A: Chem., 173 (2001) 275.

[88]. T. Luo, J.M. Vohs, R.J. Gorte, J. Catal., 210 (2002) 397.

[89]. S. Hilaire, S. Sharma, R.J. Gorte, J.M. Vohs, H.W. Jen, Catal. Lett., 70 (2000) 132.

[90]. J.L. d'Itri, Evaluation of New Mixed Oxides for Use as Sulfur Tolerant Exhaust Gas Catalysts: Final Report, Coordinating Research Council, CRC E7a-3 (2002).

[91]. S.H. Overbury, D.R. Huntley, D.R. Mullins, K.S. Ailey, P.V. Radulovic, J. Vac. Sci. Technol. A, 15 (1997) 1647.

[92]. J.C. Summers, J.F. Skowron, W.B. Williamson, K.I. Mitchell, SAE Technical Paper Series, Preprint 920558 (1991).

[93]. H.C. Yao, Y.F.Y. Yao, J. Catal., 86 (1984) 254.